UNIVERSITY of CALIFORNIA
Santa Barbara

Numerical Investigations of Many-Body Localization and non-Fermi Liquids

A dissertation submitted in partial satisfaction of the
requirements for the degree of

Doctor of Philosophy

in

Physics

by

Katharine Sarah Hyatt

Committee in charge:

Professor Matthew P. A. Fisher, Co-Chair

Dr. Bela Bauer, Co-Chair

Professor David Weld

June 2018

The dissertation of Katharine Sarah Hyatt is approved:

Professor David Weld

Professor Matthew P. A. Fisher, Co-Chair

Dr. Bela Bauer, Co-Chair

May 2018

To my friends and family.

Acknowledgements

Before all others I wish to thank my two co-advisors, Prof. Matthew P. A. Fisher and Dr. Bela Bauer. Matthew is one of the kindest, most knowledgeable, and most creative physicists I have ever known. Although our research interests eventually diverged, Matthew never stopped taking an interest in my career and never stopped helping me work towards my goals. Matthew and Bela share such an expansive understanding of condensed matter physics that it would be very intimidating, were it not for their equally expansive openhandedness with this understanding. Some people use their position of superior knowledge and experience to put others down, but in my time here both my advisors have only ever helped to pull others up. It is rare to be able to have discussions about both physics and computing with a single person – I am so grateful that Bela was such a mentor to me in both these domains. Bela has an inspiring ability to find the interesting questions to work on in many, many areas. I benefitted greatly from being able to work with him on our projects together and I am deeply grateful for his advice and support. Both my advisors have been more generous with their knowledge, time, and support than I can express or repay.

I want to especially thank Bela for reviewing many, many drafts of my thesis as a whole and the publications which went on to form parts of it. Editing on its own is difficult and time-consuming enough, but Bela faced the additional constraint of meetings which numbered closer to the size of the reals rather than the integers. I could not have asked for someone more forbearing with my snowstorm of drafts.

During the early years of my studies, Bryan Clark was another invaluable mentor, teaching me the Monte Carlo methods I would use on our early projects together and encouraging me to stick with computational condensed matter theory.

I absolutely must thank Jim Garrison. Generous and supportive, Jim was also willing to have a joint vent session about malfunctioning cluster software or programming esoterica or grad school in general. He invited me to conferences, helped me connect with other scientists and programmers, and constantly forwarded information about others I did not yet know I wanted to attend. Jim introduced me to Julia, and I never would have got so far with it absent his evangelism. He provided me with so much useful, helpful, and actionable advice. Jim is one of the most thoughtful and insightful physicists I have had the pleasure to work with. I am very grateful for the time we spent as co-located colleagues, and I wish him every success in his future career.

Although we did not overlap at UCSB for long, Ryan Mishmash gave me a great deal of useful advice which I have reflected upon often in the years since. He also passed along to me a treasure trove of annotated papers and a desktop with which I completed much of this work.

Without the steadfast encouragement and mentorship of my undergraduate advisor, Professor Roger Melko, I would never have begun graduate studies or likely continued through the many ups and downs of graduate school. My time in Roger's group at Waterloo kindled and fanned my desire to pursue a PhD in numerical condensed matter theory, and he and the other group members – Ann Kallin, Steven Inglis, Jason Iaconis –

who I spent time with were always encouraging and gave me the gift of telling me when I was wrong. Throughout the years I have been extremely lucky to benefit from Roger's advice and support, and I would not have reached this point without it.

To acknowledge those who helped kindle and sustain my interest in physics while leaving out the other condensed matter theorists in my cohort would be a serious omission. The nights Alex Rasmussen, Jason Iaconis, Dominic Else, Zhen Bi, and I worked together on our many-body field theory homework were some of the most productive I ever spent. In a thousand moments since they have provided inspiration, helpful feedback, and extremely niche jokes.

I want to thank the Julia programming language community. Both the developers of "base" itself and the wider package ecosystem made my programming experience inestimably less painful than it otherwise would have been. Additionally, having Julia to turn to when I felt frustrated with research but still wanted to make progress on something and be helpful to others was more helpful than I can say. Attending JuliaCons was something I looked forward to year after year, and being able to meet so many brilliant scientists, artists, and programmers was a privilege. I particularly wish to thank Stefan Karpinski, Jeff Bezanson, Viral Shah, Tim Holy, Seth Bromberger, Valentin Churavy, Tony Kelman, Jiahao Chen, Mike Innes, Sashi Gowda, Simon Danisch, Alex Arslan, and Alan Edelman.

Especially in the last few years, I spent a great deal of time at Station Q. The postdocs and researchers there were always welcoming and friendly and I learned a great deal about physics from them. The hive of research activity at Q helped broaden my horizons and sustain my enthusiasm for seeking out and developing new knowledge. Sean Fraer has also always been amazingly kind and helpful to me, no matter how minor my problem.

During my Station Q work hours, Christina Knapp has been a constant friend. I deeply appreciate all our conversations about work, climbing, and life in general. She is an inspirationally hard worker, in physics and outside, and I wish to thank her for all her support and the levity we shared in rough times.

I want to thank Gregory Peairs. Greg has been there for me during all the setbacks and frustrations, small or large, always encouraging me to keep going no matter how many emotional and intellectual brambles I got caught in and scraped by. No matter what, he was happy for me when something good happened, doing his best to convince me it wasn't just a fluke or a mistake, despite my sometimes impressive committment to playing Devil's advocate against myself. Even after moving to Chicago, he has been a better friend and partner than I could have ever expected or asked for. I am so glad for the time we have been able to spend together, and for the refuge I could find here in Santa Barbara or later in Chicago.

A good conference appears to run seamlessly and noiselessly, although a great deal of work goes into ensuring that this happens and into responding to the inevitable crises that arise. I would like to thank all the organizers of the many conferences and schools I attended during my graduate studies – these events reminded me what I love about physics and helped me keep the faith that continuing was worthwhile.

I also wish to thank the National Science Foundation Graduate Research Fellowship Program, which awarded me a fellowship which enabled me to focus full-time on research.

Curriculum Vitæ

Katharine Sarah Hyatt

Education

2018	Ph.D., Physics, University of California, Santa Barbara
2016	M. A., Physics, University of California, Santa Barbara
2012	Honours Bachelor of Science, Mathematical Physics, University of Waterloo, Waterloo, Ontario, Canada

Publications

"Entanglement at a Two-Dimensional Quantum Critical Point: a Numerical Linked Cluster Expansion Study", Ann B. Kallin, Katharine Hyatt, et al. *Physical Review Letters* 110, 135702 (2013)

"Many-body localization in the presence of a small bath", Katharine Hyatt, James R. Garrison, et. al. *Physical Review B* 95, 035132 (2017)

"'Extracting entanglement geometry from quantum states', Katharine Hyatt, James R. Garrison, Bela Bauer *Physical Review Letters* 119, 140502 (2017)

Abstract

Numerical Investigations of Many-Body Localization and non-Fermi Liquids

by

Katharine Sarah Hyatt

We begin with an introduction to some of the important numerical tools in the field of condensed matter theory: exact diagonalization, quantum Monte Carlo, and tensor network algorithms. We also introduce interesting problems to which they can be applied, including holographic duals (for tensor networks), many-body localization, and thermalization.

We explore, using the previously discussed quantum Monte Carlo methods, a model of itinerant interacting fermions with relevance to the mysterious pseudogap phase of the cuprate high temperature superconductors. We provide tentative evidence for a non-Fermi liquid phase believed to support a violation of area law entanglement scaling. We hope to settle numerical questions about this work in furtherance of the goal of incorporating it into a future publication.

We then explore the stability of a system predisposed towards localization coupled to a system of similar size which would, on its own, thermalize. The stability of localized systems interacting with environmental baths is both experimentally relevant and theoretically interesting, and we explore a large parameter space using exact diagonalization

techniques. We find that for a small set of parameters, localization may survive the presence of a similarly sized bath, but the tendency of the bath to delocalize the entire system is difficult to overcome. We also investigate the dynamics of these coupled systems, making connections with previous theoretical studies. This work is adapted from previously published material.

We take steps towards developing a new tensor network technique with which to study non-equilibrium quantum systems. We develop a disentangling circuit generation algorithm, drawing on previous algorithms for representing a variety of interesting wavefunctions, which can disentangle generic states without reference to a Hamiltonian. This is a novel departure from many previous disentangling approaches or tensor network optimization algorithms. We apply this technique to well-understood physics in the form of disordered models of free fermions, detecting an emergent entanglement geometry which reproduces interesting features of holographic duality. This work is also adapted from a previous publication.

We then extend these results to the realm of dynamics, investigating the effects of quantum quenches on the circuits generated by the disentangling algorithm and the role disorder may play. We find an intriguing connection between disorder strength and the effective energy density (or effective "temperature"). We also observe two regimes, one as the system approaches its volume law limit, and another of slowly decaying oscillations after it has reached the long-time regime of volume law entanglement scaling. We hope to develop this last set of results into a future publication.

Contents

Chapter 1

Introduction

1.1 Entanglement

One of the most striking features of quantum mechanics that goes beyond classical physics is the notion of entanglement. In a classical system of more than one body, a constituent of the whole (for instance, a small subregion) is separable from the rest. One can obtain full information about its configuration without reference to the excluded parts. In quantum mechanics this is no longer the case - quantum systems have a notion of "entanglement". Quantum objects can come together to form a whole that is substantially more than the sum of its parts. In an entangled pair of objects, tracing out one half necessarily discards information, and only by making measurements on both sub-parts together can we understand the entire object. A famous example of an entangled pair is

a Bell state [20]:

$$|\Psi_B\rangle = \frac{1}{\sqrt{2}}\left(|\uparrow\uparrow\rangle + |\downarrow\downarrow\rangle\right) \tag{1.1}$$

This is a wavefunction for two spin $\frac{1}{2}$ particles on two sites. The wavefunction $|\Psi_B\rangle$ on *both* sites is a pure state. We can construct its density matrix:

$$\begin{aligned}\hat{\rho}_{12} =& |\Psi_B\rangle\langle\Psi_B| \\ =& \frac{1}{2}\begin{bmatrix} 1 & 0 & 0 & 1 \\ 0 & 0 & 0 & 0 \\ 0 & 0 & 0 & 0 \\ 1 & 0 & 0 & 1 \end{bmatrix}\end{aligned}$$

The trace of a density matrix is always 1 [147]. If we compute $\mathrm{Tr}\,\hat{\rho}^2$ we find it is also 1, because $|\Psi_B\rangle$ is a pure state and we have complete information about it. This is the diagnostic for whether a density matrix represents a pure ($\mathrm{Tr}\,\hat{\rho}^2 = 1$) or mixed ($\mathrm{Tr}\,\hat{\rho}^2 < 1$) state.

However, if we trace out one of the sites (say site 2), the resulting description must

be in terms of a mixed state, which can only be written as a reduced density matrix.

$$\begin{aligned}\hat{\rho}_1 &= \sum_{\{|\psi_2\rangle\}} \langle\psi_2 \,|\, \hat{\rho} \,|\, \psi_2\rangle \\ &= \frac{1}{2}\begin{bmatrix} 1 & 0 \\ 0 & 1 \end{bmatrix}\end{aligned}$$

Here again the trace is 1, but $\operatorname{Tr}\hat{\rho}_1^2 = 1/2$ and so $|\Psi_B\rangle$ is entangled - only the joint representation over the whole system can be written as a pure state wavefunction. To quantify the degree of entanglement we can use the entanglement entropy

$$S(\hat{\rho}) = -\operatorname{Tr}\hat{\rho}\log\hat{\rho} \tag{1.2}$$

If the matrix $\hat{\rho}$ has eigenvalues $\{\lambda\}$, $S(\hat{\rho}) = -\sum_{\{\lambda\}}\lambda_i \ln\lambda_i$. The pure state $|\Psi_B\rangle$ has entanglement entropy $S(|\Psi_B\rangle\langle\Psi_B|) = 0$. Pure states always have zero entanglement entropy. However, the mixed state $\hat{\rho}_1$ has entanglement entropy $S(\hat{\rho}_1) = \ln 2$. Thus $|\Psi_B\rangle$ is an entangled pair, where each spin of the pair is entangled with the other.

This is a simple example on a 2-site system, but it is possible to compute entanglement between larger regions as well: for instance, a small 4-site cluster of a large lattice. Groundstates with a gap – a non-zero energy difference between the groundstate and first excited state – are conjectured have an "area law" [225]. In one dimension this has been proven [74]. The entanglement entropy $S(\hat{\rho}_A)$ of a subregion A scales with the size of the *boundary* of this region (so that it is constant in one dimension, linear in two dimensions, etc.). In higher dimension there are examples of area law scaling [8]. This

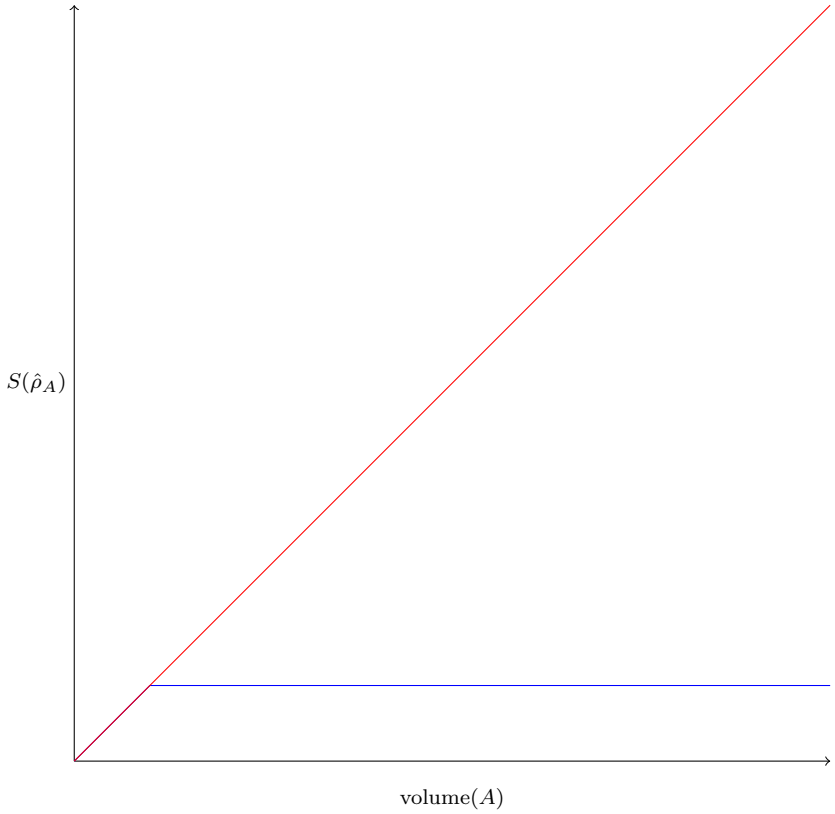

Figure 1.1: Schematic depiction of an area law scaling (in blue) and a volume law scaling (in red) of entanglement entropy in a one-dimensional subregion A.

is in contrast to the behavior of (most) highly excited states (see Sec. 1.5 for a notable exception), which are "volume law" - $S(\hat{\rho}_A)$ scales with the size of the subregion (so that it is linear in one dimension, for example). A qualitative example of both is shown in Fig. 1.1.

Groundstates may also have *violations* to the area law, and such states are an active area of research since they so often host interesting physics. For example, groundstates of one dimensional critical systems, which are scale invariant, have a logarithmic violation of the area law [31]. Fermi liquids in two or more dimensions are known to have logarthmic violations as well [224], and non-Fermi liquids have logarithmic violations different from

those of Fermi liquids, which is one way to distinguish the two. This violation allows us to access very important information which characterizes the theory describing the system – the central charge [31, 30]. In two or fewer dimensions, we have a complete classification of conformal field theories, and measuring the central charge allows us to fingerprint the governing CFT. In higher dimensions the situation is more complex [53].

States with non-trivial topological order also have area law violations. A constant "topological term" is present in addition to the area law scaling in these states, and computing this term again functions as a fingerprint for topological order [53].

1.2 Exact Diagonalization

Exact diagonalization (ED) is in some sense the simplest of all numerical approaches to study quantum systems. For a finite size Hilbert space (or one which has been truncated, for instance by constraining the maximum occupation number of any site for soft-core bosons) the Hamiltonian can be represented by a Hermitian matrix. A variety of specialized algorithms have been developed to study the spectra of such matrices, owing to their presence in many areas of research. Some forms of exact diagonalization simply compute the entire spectrum of a Hermitian matrix, eigenstates and their eigenvalues (energies), and these results can then be used to study properties of the system (for example, determining if a finite temperature phase transition exists). Others, such as the Krylov methods discussed below, are useful when only a small portion of all the eigenstates are of interest or computationally accessible, as is true for large system size.

As the name implies, exact diagonalization can provide us with the exact eigenstates of a Hamiltonian. The results are subject to numerical error, but if the method has converged they should be unbiased and reproduce all the features of the true states we might calculate analytically. But this comes at the cost of very bad performance at large system size/for large Hilbert spaces. The largest exact diagonalization studies to date made extensive use of symmetries (which allow the Hilbert space to be "folded down" and represented in a smaller format) and were able to reach 42 sites total [34] or, recently, 50 spins [222]. Even in one dimensional systems, this may not be large enough to robustly generalize to the thermodynamic limit. The situation is even worse in higher dimension.

For models where other algorithms are practical, ED can be a suggestive first step against which the other methods can be tested (they should agree for the smaller systems ED can access). It can also illustrate what regions of the explorable parameter space are likely to be "interesting" in the sense that a phase transition may be present or some other sort of interesting physics is present (topological states, localized states, etc.).

For some models, algorithms have not yet been developed to efficiently approximate the interesting states and/or physics. Examples of such models are frequent outside an equilibrium context, as we will see later in the context of many-body localization. Developing new techniques beyond ED to simulate these models remains an outstanding problem in the field of numerical condensed matter physics.

1.2.1 Krylov Methods

Often, the most interesting eigenstates are those lowest down in the spectrum, the ground-states and low energy excited states. When the system is at low/zero temperature, these states are dominant, and interesting many-body quantum effects (superfluidity and long range magnetic order, to give two examples) are observable. Rather than diagonalizing the entire spectrum, it is desirable to focus on acquiring these interesting states. Krylov methods [114] were developed for such problems. The Lanczos method [115] is the most commonly used of these in physics, although others (such as Jacobi-Davidson [187]) exist as well.

The Lanczos method works by constructing a restricted subspace of the full Hilbert space (the *Krylov space*) by repeated applications of the Hamiltonian to a moving "guess" vector, eventually driving it to the eigenvector with smallest eigenvalue (lowest energy, i.e. the groundstate).

For a chosen number of iterations M:

1: Let $|\phi_0\rangle \in \mathbb{C}^n$ be a *normalized* initial guess for the eigenvector with smallest eigenvalue.

2: $|\varphi_0'\rangle \leftarrow \hat{H}\,|\phi_0\rangle$

3: $a_0 \leftarrow \langle\varphi_0'|\phi_0\rangle$

4: $|\varphi_0\rangle \leftarrow |\varphi_0'\rangle - a_0\,|\phi_0\rangle$

5: **for** $i \leftarrow 1, M-1$ **do**

6: $\quad b_i \leftarrow \sqrt{\langle\varphi_{i-1}|\varphi_{i-1}\rangle}$

7: $|\phi_i\rangle \leftarrow \frac{|\varphi_{i-1}\rangle}{b_i}$

8: $|\varphi_i'\rangle \leftarrow \hat{H}\,|\phi_i\rangle$

9: $a_i \leftarrow \langle\varphi_i'|\phi_i\rangle$

10: $|\varphi_i\rangle \leftarrow |\varphi_i'\rangle - a_i\,|\phi_i\rangle - b_i\,|\phi_{i-1}\rangle$

11: **end for**

12: Let $\hat{V}$ be an N by M matrix such that its i-th column is the vector $|\phi_i\rangle$.

13: Let $\hat{T}$ be a tridiagonal M by M matrix such that $T_i^i \leftarrow a_i$, $T_i^{i+1} \leftarrow b_{i+1}$, $T_{i+1}^i \leftarrow b_{i+1}$.

All eigenvalues of $\hat{T}$ are eigenvalues of $\hat{H}$, and if $|\psi'\rangle$ is an eigenvector of $\hat{T}$ then $|\psi\rangle = \hat{V}\,|\psi'\rangle$ is an eigenvector of $\hat{H}$. The eigenvectors have the same ordering, so that the lowest energy eigenvector of $\hat{T}$ will be transformed into the lowest energy eigenvector of $\hat{H}$.

The advantage of this method is that matrix-vector products are much quicker and less memory intensive to compute than the matrix-matrix operations required for a full diagonalization. Computing the eigensolution of a symmetric tridiagonal matrix like $\hat{T}$ is much less expensive than doing so for a generic Hermitian matrix like $\hat{H}$. When the eigenvectors are converged (which can be checked by comparing their eigenvalues from iteration to iteration and their overlap between iterations) the procedure is done and measurements (e.g. correlators) can be made on the eigenvectors.

1.2.2 Shift-and-Invert Approaches

Traditional Krylov methods are very effective when we are interested in the behavior of a system's groundstate or low energy excitations. To probe states deep in the band using

these methods requires first computing all eigenstates with energies below the energy level of interest, which is both time- and memory-expensive. A technique which can selectively search for states close in energy to the "target" (e.g. halfway between the groundstate energy and highest possible energy in a system with bounded Hilbert space) is desirable.

Consider a target energy σ for a Hamiltonian $\hat{H}$. A natural approach might be to compute the operator $\hat{A}_2 = (\hat{H} - \sigma\hat{\mathbb{I}})^2$, where $\hat{\mathbb{I}}$ is the identity, and then apply standard Krylov methods to this new operator. $\hat{A}_2$ has the same *eigenvectors* as $\hat{H}$, but the *eigenvalues* are different. However, this approach is often not numerically tractable: deep in the band, the level spacing is exponentially small in the system size. This means that $\hat{A}_2 = (\hat{H} - \sigma\hat{\mathbb{I}})^2$ will have level spacing $\propto \exp\{-2N\}$, and as discussed above, Krylov methods perform better (in terms of time to converge) when the gap between adjacent energy levels is larger. The choice of operator $\hat{A}_2$ works against the strengths of these methods. Additionally, for large systems, the level spacing may be so suppressed that even double precision floating point numbers may not have enough precision to reliably separate two adjacent levels of $\hat{A}_2$. In such a situation, we would either need a new algorithmic approach or need to go to higher floating point precision, which can have dramatic negative impacts on performance (in addition to the convergence issue mentioned previously).

Another choice of operator is available: $\hat{A}_{-1} = \left(\hat{H} - \sigma\hat{\mathbb{I}}\right)^{-1}$. This forms the basis of the "shift-and-invert" method for performing exact diagonalization studies where highly

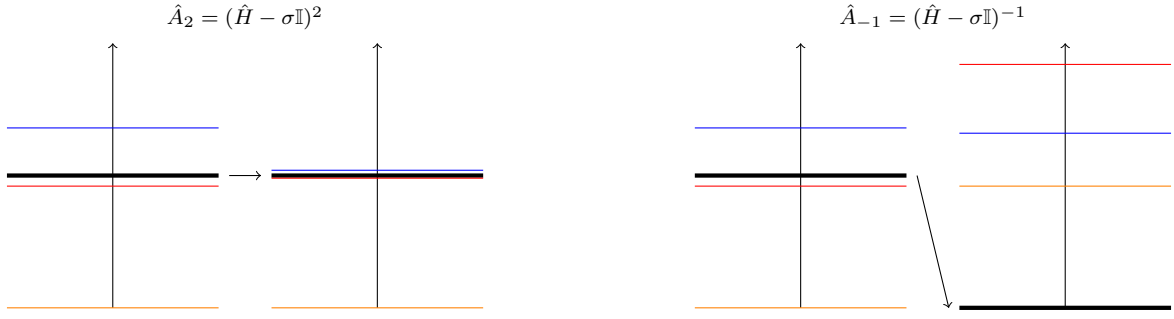

Figure 1.2: Schematic illustration of the differences in the two operators' level spacing. The eigenstate with energy closest to σ before the transformation is shown in black.

excited states are of interest. Unlike $\hat{A}_2$, the inversion step in $\hat{A}_{-1}$ transforms very closely spaced levels into very widely separated levels. This plays to the strength of Krylov methods, so after $\hat{A}_{-1}$ has been computed, its groundstate (which is the eigenstate of $\hat{H}$ with energy closest to σ) can be relatively easily computed.

This method also has drawbacks. In large scale numerical simulations, $\hat{H}$ is usually represented as a (very) sparse Hermitian matrix or as a function to compute matrix-vector products on given vectors in the Hilbert space which could be used to construct such a matrix. But there is no guarantee that $\hat{A}_{-1}$ will be sparse, and indeed sparse matrices often have dense inverses. Matrix inversion is also a very time-intensive operation.

A commonly applied solution is to use preconditioning [22]. Several preconditioning algorithms exist, and many used for this purpose attempt to find a matrix $\hat{N}$ which, for a sparse matrix $\hat{M}$, has a spectrum as close as possible to that of the exact $\hat{M}^{-1}$ while having the same sparsity pattern as $\hat{M}$. This approach reduces the risk of running out of memory while still being accurate and precise enough to reliably allow us to target states deep in the band of a Hamiltonian and also saves time.

This approach of preconditioner-based inversion and subsequent Krylov method based extraction of eigenstates can be implemented in parallel (e.g. using MPI) and on distributed memory systems. As discussed in Chapter 3, pre-written software packages exist which provide such implementations and can be used to investigate the properties of highly excited states in physical systems where they are important, such as in many-body localized phases.

1.3 Monte Carlo Methods

We may want to simulate a zero temperature system using a Monte Carlo technique in the case that other methods are not suitable. There are many such techniques – stochastic series expansion [172], diagrammatic Monte Carlo [162], determinantal Monte Carlo [196, 110, 24], and various worldline methods [218, 161, 80], to give a few examples. Many of these methods are "Markov chain Monte Carlo" (MCMC), in that they can be modelled as Markovian processes [72, 133]. Such MCMC methods must have two features:

1. Detailed balance – the weighted transition rate *into* and *out of* a configuration must be the same:

$$W(c)P(c \to c') = W(c')P(c' \to c)$$

, where P represents the probability of transition. The simplest way to satisfy this is to require that the transition rate from configuration $c_1 \to c_2$ is the same as the transition rate from $c_2 \to c_1$.

2. Ergodicity – all configurations are accessible during the simulation. This may be more difficult to satisfy than it first seems. If the simulation must climb a very tall, very "steep" energy barrier to move from a metastable configuration into the groundstate, it may never do so, and therefore not be ergodic, even though the groundstate is (in theory) accessible [116]. If we are willing to wait "long enough", the simulation will eventually reach the true groundstate, but this may be a very long time.

The stable state of the Markov process should reproduce the equilibrium state of the physical system being simulated - for example, it should efficiently sample the partition function $\mathcal{Z}$, with the correct Boltzmann distribution at inverse temperature β. In general, the detailed balance condition ensures an invariant target distribution like the Boltzmann distribution exists, while the ergodicity condition ensures this distribution is reachable in the simulation [204, 135].

MCMC methods have achieved great success simulating many physical systems [173, 134, 75, 52, 112, 71] but in some cases they struggle to achieve ergodicity. Another family of methods, projector Monte Carlo(s), dispense with restriction (1) in order to get around the ergodicity problem. First developed several decades ago [97, 100, 25], such methods have achieved success for interesting physical models [81, 82, 202, 175, 174]. In the following sections, we summarize how this is possible and some of the drawbacks doing so introduces.

1.3.1 Diffusion Monte Carlo

In projector Monte Carlo methods we start with a trial wavefunction, $|\Psi_T\rangle$, a technique first introduced in Ref. [99]. Then, we apply a projection operator $\hat{P}$ many times to this trial state, hopefully driving the system into its groundstate. There are many different projectors we might apply, and each resulting method has a name:

- $\hat{P}^N = \exp\{-\beta\hat{H}\}$ - Diffusion Monte Carlo
- $\hat{P}^N = \left[1 + \tau\hat{H}\right]^{-1}$ - Green's Function Monte Carlo
- $\hat{P}^N = 1 - \tau\hat{H}$ - Power Monte Carlo

We can simulate in continuous or discrete time. The discrete case is simpler. We can do a Trotter discretization on the projector, and obtain the projection operator we want to use:

$$\hat{P} = \left(1 - d\tau\hat{H}\right)$$
$$\exp\{-\beta\hat{H}\} = \prod_{i=1}^{N} \hat{P} + \mathcal{O}(1/N^2)$$
$$\hat{P}^N |\Psi_T\rangle = |\Psi_0\rangle$$

This relation holds for large N and small $d\tau$. Repeated applications of $\hat{P} = \left(1 - d\tau\hat{H}\right)$ will drive the system into its groundstate if we choose to do diffusion Monte Carlo (this will efficiently sample the partition function).

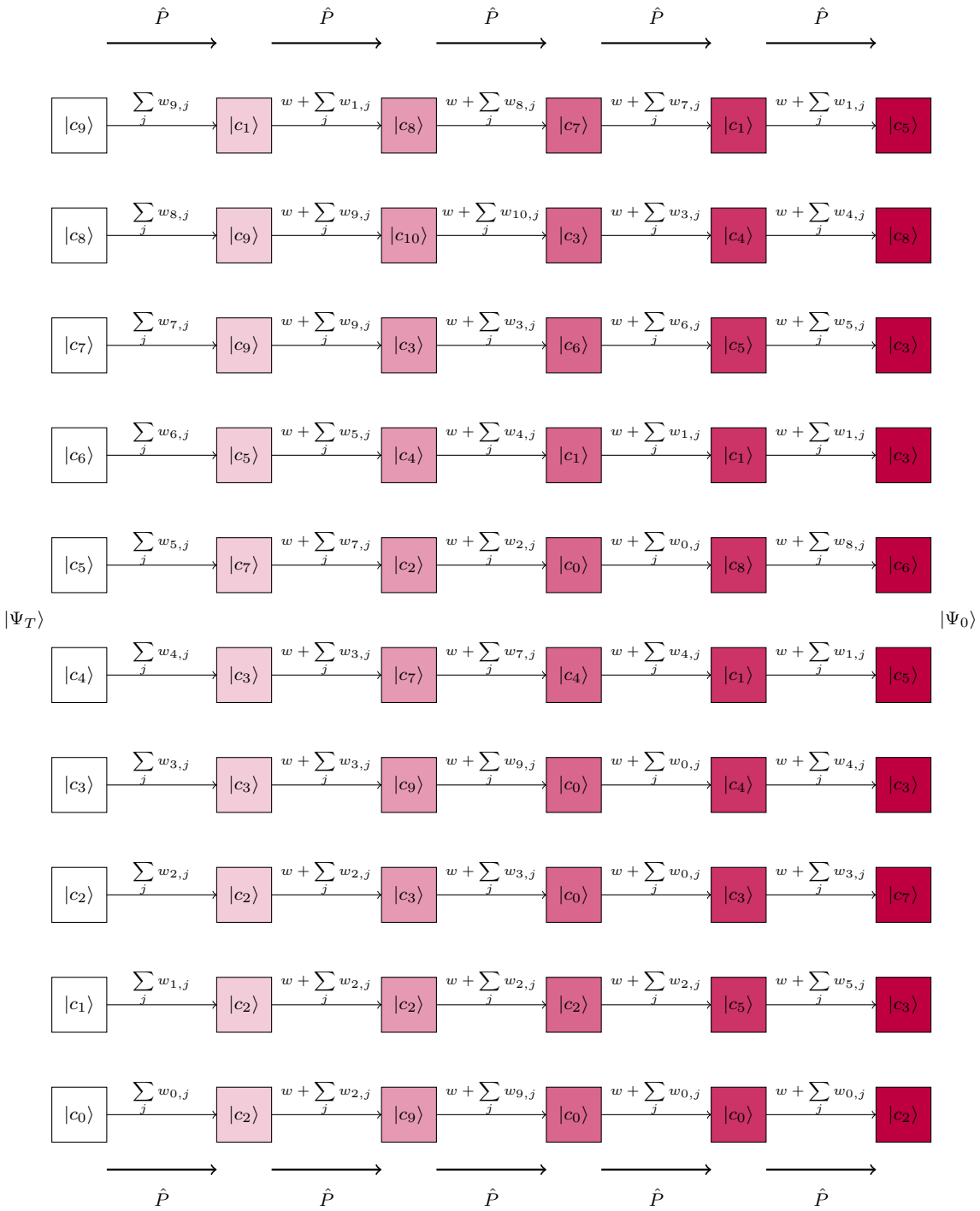

Figure 1.3: A schematic diagram of five update steps on 10 walkers performed using a projector $\hat{P}$, with weights accumulating until the posterior distribution describing $|\Psi_0\rangle$ is reached. w at each step represents the accumulated walker weight since the last rebalance/initialization of the simulation.

Note that for large N, $\hat{P}^N = \exp\{-\beta\hat{H}\}$ and therefore $d\tau \cdot N = \beta$. If we wish to access the groundstate then the "effective β" in the simulation must be large. Generally many projections are applied (see more below for details), with the energy being checked at each step, until the system has converged into the groundstate. Measurements can then be performed, while continuing to apply the projection operator so that many samples can be taken and the error of these measurements is minimized.

How are projector methods different from MCMC methods discussed above? For some models, especially those with many-particle interactions, achieving ergodicity becomes very difficult. MCMC lives or dies by its updating scheme and finding one which does not have a sign problem, is ergodic, and will obey detailed balance is often not possible. A projector method removes the condition of detailed balance to restore ergodicity, at the cost of introducing statistical biases discussed in more detail below.

Implementing Projection Operators

When initializing the simulation, one selects a population size N_p (which may be fixed, or may grow or shrink - the fixed case is simpler) and prepares the population of "walkers" according to the trial wavefunction $|\Psi_T\rangle$. This trial wavefunction can be obtained a number of ways - variational Monte Carlo, analytical intuition, DMRG studies in ladders. It can also be set to be a uniform distribution across the Hilbert space, which avoids biasing the simulation at the cost of worse performance (statistics will take longer to converge). Biased or no, each walker is accompanied by a "weight" drawn from the trial distribution. In the unbiased case, all the weights are 1. The "walker" is a configuration

(basis element) in the Hilbert space which will be updated, tracing a "walk" through phase space which can be sampled to compute correlators, Green's functions, etc.

It is important to note that even in the unbiased case, the initial wavefunction does not need a representative of *every* basis element! The principle of Monte Carlo simulations is that by picking a good updating scheme, we will focus on the configurations which contribute most to the partition function. So we can draw randomly from configuration space.

Each walker is updated independently. The projector operation is used to create a list of possible moves. In the case that $\hat{P}$ is small enough to represented as a sparse matrix, this list of moves would simply be the row of $\hat{P}$ corresponding to the current configuration. Usually $\hat{P}$ is too large to be stored in matrix format, so it is instead kept as a row-generating function which returns a list of possible configurations to move to (and their matrix elements). To choose a new configuration, a weighted sample is taken from this new distribution. After the move is chosen, the current configuration is stored in a "history" of the walk, and the current weight is *multiplied* by the *sum* of all the matrix elements of the possible moves.

If the initial guess is poor and most of the initial walkers are in an unimportant region of configuration space, some of the walkers will very quickly accumulate far more weight than others. Even if we choose well, the fact that the weights are multiplied at each step means they will quickly grow so large that they threaten to overflow their floating point number representation. To solve this problem we can perform a "population

rebalance" [11]. If the population size is fixed, we again do a weighted sample among the accumulated weights so far, *keeping a record of the sum of the weights.* This record will be important to correct for statistical issues arising from having a population size smaller than the Hilbert space size. After the population rebalance, all weights are set to 1 again and the updates proceed. A rebalance should be done every N_r update steps for consistency.

1.3.2 Mixed Estimator Error and Forward Walking

To make a measurement of an observable $\hat{O}$ on a groundstate wavefunction $|\Psi_0\rangle$, basic quantum mechanics gives us the formula:

$$\begin{aligned}\left\langle \hat{O} \right\rangle =& \frac{\left\langle \Psi_0 \left| \hat{O} \right| \Psi_0 \right\rangle}{\langle \Psi_0 \mid \Psi_0 \rangle} \\ =& \frac{\sum_{|c\rangle} \sum_{|c'\rangle} \langle \Psi_0 \mid c \rangle \left\langle c \left| \hat{O} \right| c' \right\rangle \langle c' \mid \Psi_0 \rangle}{\sum_{|c\rangle} |\langle \Psi_0 \mid c \rangle|^2} \\ =& \frac{\sum_{|c\rangle} \sum_{|c'\rangle} \left\langle \Psi_T \left| \exp\{-\beta \hat{H}\} \right| c \right\rangle \left\langle c \left| \hat{O} \right| c' \right\rangle \left\langle c' \left| \exp\{-\beta \hat{H}\} \right| \Psi_T \right\rangle}{\sum_{|c\rangle} \left| \left\langle \Psi_T \left| \exp\{-\beta \hat{H}\} \right| c \right\rangle \right|^2}\end{aligned} \tag{1.3}$$

Consider the state of the simulation walkers at step i of the simulation, corresponding to effective time $\tau = i \cdot d\tau$, at which point it has run for inverse temperature $\beta(\tau)$ "time" - each carries a configuration $|c\rangle$ and a corresponding weight $w_c(\tau)$ so that $|\Psi(\tau)\rangle = \sum_{|c\rangle} w_{|c\rangle}(\tau) |c\rangle$. An intuitive guess for how to compute the expectation value of $\hat{O}$ using

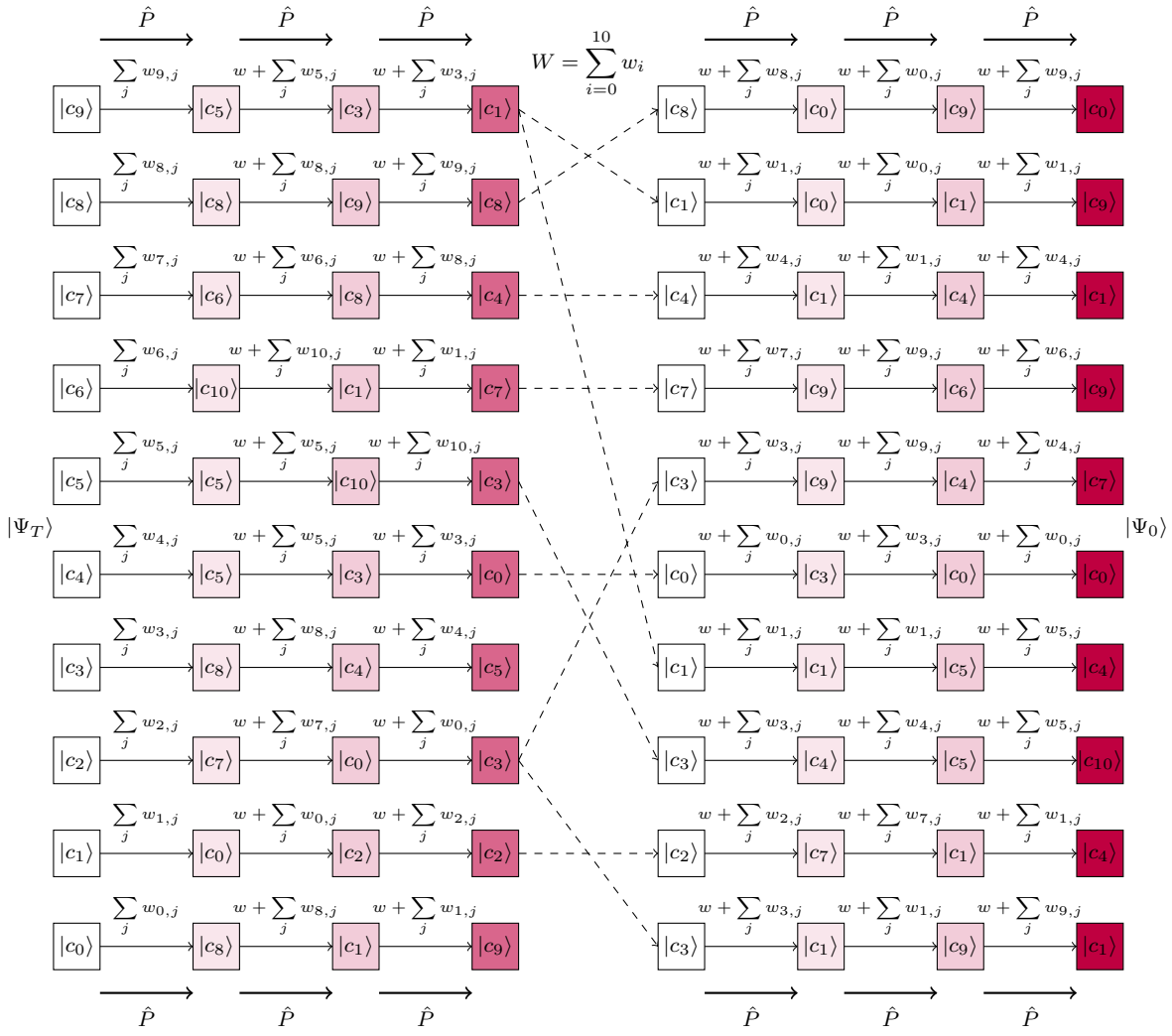

Figure 1.4: A schematic diagram of four update steps on 10 walkers performed using a projector $\hat{P}$, with weights accumulating. Each w at an update step represents the weight accumulated so far by the walker since the last rebalance/since the simulation began. A rebalance is performed, resetting the weights to 1 on the surviving configurations. Note that some configurations "die out" - for this reason, the total weight W is tracked so that population bias control can be perfomed. After the rebalance, updates resume until the posterior distribution describing $|\Psi_0\rangle$ is reached.

these w would be to compute a simple weighted average:

$$\begin{aligned}\left\langle \hat{O} \right\rangle_T =& \frac{\sum_{|c\rangle} w_{|c\rangle}(\tau) \left\langle c \left| \hat{O} \right| c \right\rangle}{\sum_{|c\rangle} w_{|c\rangle}(\tau)} \\ =& \frac{\sum_{|c\rangle} \sum_{|c'\rangle} \langle \Psi_0 \,|\, c\rangle \left\langle c \left| \hat{O} \right| c' \right\rangle \langle c' \,|\, \Psi_T\rangle}{\sum_{|c\rangle} \langle \Psi_0 \,|\, c\rangle} \\ =& \frac{\sum_{|c\rangle} \sum_{|c'\rangle} \left\langle \Psi_T \left| \exp\{-\beta(\tau)\hat{H}\} \right| c \right\rangle \left\langle c \left| \hat{O} \right| c' \right\rangle \langle c' \,|\, \Psi_T\rangle}{\sum_{|c\rangle} \left\langle \Psi_T \left| \exp(-\beta(\tau)\hat{H}) \right| c \right\rangle}\end{aligned} \tag{1.4}$$

If $\hat{O}$ does not commute with $\hat{H}$ (and therefore $\exp\{-\beta\hat{H}\}$), Eq. (1.4) is not the same as Eq. (1.3). Effectively, one would be sampling $O(c)$ weighted by $|\Psi_0(c)|$ and *not* $|\Psi_0(c)|^2$. In most cases, correlators of interest do not commute with $\hat{H}$, and the natural guess of simply doing a weighted average over the walkers will give the "mixed estimator error" [36]. Note that the *energy* does not suffer from this error, since $\hat{H}$ commutes with itself. A modification to the averaging scheme in the simulation must be made to correct for this error. Forward walking is one solution.

In Sec. 1.3.1, the process of updating the walkers at each time step was described. The history kept of which configurations have been visited along the worldline will be used to correct the mixed estimator error. Essentially, there is a "missing" $\exp\{-\beta'\hat{H}\}$ in the $\langle \ldots \rangle$ expressions in Eq. (1.4). The principle of forward walking is to "walk" in reverse along the worldline a β' "far enough" into its history that transforming $|c(\tau)\rangle \rightarrow$

$|c'(\tau - \beta')\rangle$ recovers a good representation of the groundstate. In general, once the walkers have converged to a good sample of $|\Psi_0\rangle$ (which can be checked using their overall energy), β' need not be particularly large compared to the overall simulation time.

In the forward walking sampling, each walker marches n_f steps backwards into its configuration history, and uses that historical configuration in the weighted average, but the *weight* used should be the current weight (*not* the weight the walker had "historically"). It is therefore convenient to make measurements after a rebalance, since all the walkers will have weight 1. An appropriate number of forward walking steps can be determined by measuring correlators at each step and walking back through history until the correlators have converged.

1.3.3 Population Bias Control

During the rebalance, some walkers and their histories may die out and be discarded. This loss of information can bias the simulation. Population bias control (PBC) is another corrective which can be used to attempt to remove the bias in the correlator statistics [113]. At each rebalance, the sum of all walker weights is stored before each walker's weight is reset to 1.

To perform N_{PBC} steps of population bias control, at each rebalance, the total weight

at rebalance r W_r is multiplied by the weight at the N_{PBC} previous rebalances.

$$W'_r = \prod_{i=r-N_{PBC}}^{r} W_i$$
$$W_i = \sum_{j=1}^{N_p} w_{|c_j\rangle}(\tau_i)$$

Then a simple weighted average can be performed across all rebalance measurements. Again, measuring only at rebalance steps makes the procedure of combining forward walking and population bias control simpler. A forward walk which "crosses" a population bias control step (for instance, if the walk is longer than the number of steps between rebalances and $N_{PBC} > 0$) does not affect this process: the final weight from population bias control is used with the configuration from the forward walk. No extra correction in the bias control is necessary no matter the length of the forward walk. The weighted average across rebalances is a way of importance sampling the configuration space - rebalances after a large total weight has accumulated are more relevant to the partition function and observables than rebalances where a proportionally smaller amount accumulates.

In Chapter 2 we apply these Monte Carlo methods to a two dimensional model of itinerant electrons with a 4-fermion ring exchange term. This model, which is sign problem free, may support an intriguing non-Fermi liquid phase.

1.4 Tensor Networks

Despite the many and various successes of quantum Monte Carlo, exact diagonalization, and other methods, many other interesting questions in condensed matter physics which could benefit from a numerical approach cannot be tackled by these means. The family of sign problems – interacting fermions [125], geometrically frustrated spin systems [117] – drastically handicap a Monte Carlo approach to attack systems such as high-Tc superconductors [118].

Although it is possible to find ingenious reweighting schemes [124, 40] to remove the sign problem, solving it for a general Hamiltonian is known to be NP-HARD [207].

Exact diagonalization cannot access large system sizes in dimensions greater than 1, and Monte Carlo techniques which are not vulnerable to sign problems (like variational Monte Carlo) are biased and/or have uncontrolled error [205].

Tensor network states are a class of wavefunction ansätze which are unbiased, can represent states on large (even infinite) systems, and can be exploited by variational approaches to efficiently search for low lying states [150]. A rank-n tensor is an n dimensional array of numbers. A 2-tensor is a matrix, a 1-tensor is a vector, and a 0-tensor is a scalar. By computing inner (outer) products over indices in a tensor we can contract (expand) it to different ranks. A tensor network is a graph, with nodes and edges connecting these nodes. A tensor lives at each node, and is connected to other nodes (tensors) through edges, which represent indices to be contracted over. Not every edge has to connect two nodes - "dangling" edges represent contractable indices and can ad-

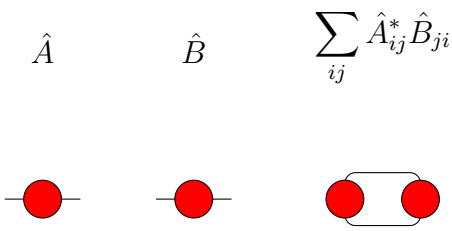

Figure 1.5: Two matrices, $\hat{A}$ and $\hat{B}$, presented as 2-tensors and then multiplied. Each has two dangling edges (since matrices have two indices) which, when joined up, represent a matrix multiplication and summation, generating a rank 0 tensor (a scalar). If only one set of legs were joined, another rank 2 tensor would be the result - this would be a matrix multiplication.

dress physical qubits. We can think of the nodes in a tensor network as representing qubits which can be used in a quantum algorithm – a deep connection exists between tensor network states and quantum circuits [130, 68].

In Fig. 1.5 a cartoon of matrix multiplication in this format is presented.

Tensor networks can be used to encode wavefunctions. A linear combination of vectors in a Hilbert space is a "tensor network" with rank of the number of sites. It is possible to write down an infinite number of combinations of tensors and connections between them, but many of these will be too large to represent on a computer and/or tell us nothing interesting about the physical states they are supposed to represent.

We should use patterns of TN which can capture most of the information about a wavefunction in a compact way, so that investigations of large systems which cannot be accessed using other numerical techniques are possible; which can be efficiently manipulated, so that the TN can easily be optimized to represent certain states or to simulate dynamics; and which can illuminate important features of certain kinds of states. To elab-

orate on this last criterion, it is often interesting to know whether a state has correlations which decay as a power law, or exponentially, and how the wavefunction's entanglement between different subregions of the system scales with the size of those subregions or the size of their boundaries. Useful TN constructions will help us answer these questions. If a wavefunction can be efficiently simulated by a TN designed for states with exponentially decaying correlations, that tells us something about the structure of its correlations and, if it is the eigenstate of a Hamiltonian, that model as well (e.g. it has a gap). Conversely, if we need a TN which can capture power-law decaying correlations, or model a wavefunction that is scale invariant, that tells us something too (maybe the system is critical).

Some of the most commonly used tensor network states are the matrix product states, used to great success in 1D and quasi-1D density matrix renormalization group studies [180]; and MERA, applicable to a variety of wavefunctions, including groundstates for critical systems, in any dimension [213, 214]. Other structures (like the tree tensor networks [62, 186]) have also been developed, and this is an active area of research. Recently, tensor networks have been both designed by machine learning approaches [230] and used with such algorithms to improve their accuracy or enable new applications [194].

1.4.1 Matrix Product States

Over the past two decades, exact diagonalization and quantum Monte Carlo have largely been supplanted in studies of one dimensional many body quantum systems by the density

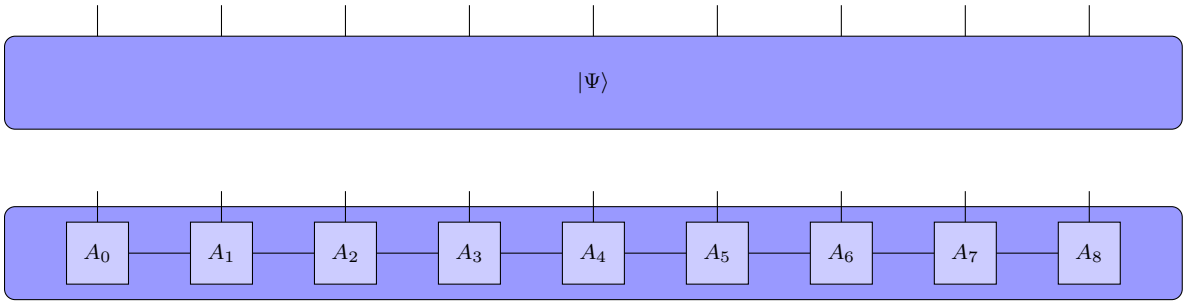

$$|\Psi\rangle = \sum_{p_0,p_1,\ldots,p_8} c_{p_0,p_1,\ldots,p_8} \, |p_0\rangle \otimes |p_1\rangle \otimes \ldots \otimes |p_8\rangle \, ; \quad c_{p_0,p_1,\ldots,p_8} = \sum_{v_0,v_1,\ldots,v_8} A^{p_0}_{v_0} A^{p_1}_{v_0,v_1} \ldots A^{p_7}_{v_7,v_8} A^{p_8}_{v_8}$$

Figure 1.6: MPS composed of tensors A_i representing wavefunction $|\Psi\rangle$. The vertical lines represent physical degrees of freedom (p_i in the above formula), the horizontal lines within the MPS virtual degrees of freedom (v_i). If $|\Psi\rangle$ has low (high) entanglement, the bond dimension along these horizontal connections will be small (large) and the MPS representation will (not) be efficient.

matrix renormalization group (DMRG) [180]. First developed by White et al. [221], DMRG is a very effective technique to simulate systems with gapped groundstates [179]. DMRG has also been successfully used to study critical systems and states with non-zero central charge [94, 63, 226]. Unlike quantum Monte Carlo, DMRG never suffers from sign problems, and unlike exact diagonalization, it can reach very large (even infinite) system sizes [180].

Although DMRG as originally formulated [221] did not use the language of tensor network states, these representations turn out to be a very natural way to describe how the algorithm works and why it succeeds or fails[180]. In DMRG, the wavefunction to be variationally optimized can be written as a matrix product state (MPS)[180, 132, 151, 168, 51, 131]. The tensor network descriptions and operations can be represented in a graphical format, as discussed above in Section 1.4. An example is shown in Fig. 1.6.

The virtual legs on each tensor in the MPS encode correlations between neighboring sites. To accurately represent these correlations requires a larger matrix on each site if the wavefunction has high entanglement. The matrix size in this direction is named the "bond dimension" and if the bond dimension grows too large (the wavefunction is too highly entangled), the DMRG approach will fail both because storing the wavefunction representation becomes impossible and time required for the necessary linear algebra for the optimization procedure grows beyond what is practical [180]. But if the entanglement is small, the MPS representation is highly efficient, because far fewer parameters are needed to capture the behavior of $|\Psi\rangle$ than if the full Hilbert space representation were used. MPS can represent any wavefunction given a large enough bond dimension [212], but is not used for highly entangled (super-area law) states because the representation is very inefficient. The performance of DMRG scales as χ^3, where χ is the MPS bond dimension, so that accurately simulating highly entangled states becomes infeasible on current computing hardware [101].

The algorithm works by sweeping left and right across a system (or, in the multi-leg ladder case, snaking across the vertical legs) [221]. At each step, the ansatz for the state of interest is optimized with respect to a local operator, called a "matrix product operator" (MPO) in the tensor network language. This procedure is represented graphically in Fig. 1.9. Much like a matrix product *state*, a matrix product *operator* is formed of tensors for each degree of freedom on a site with virtual links between sites, shown in graphic form in Fig. 1.7.

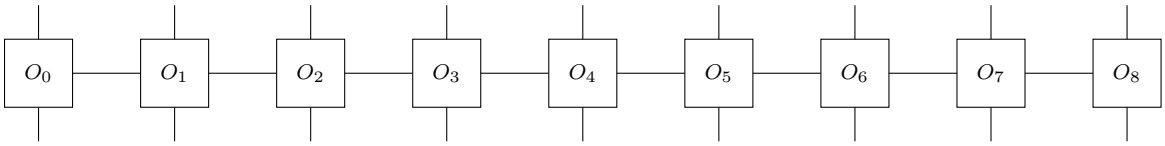

Figure 1.7: An MPO for a system with 9 sites with open boundary conditions. Each inner tensor O_i has four "legs", two physical (vertical) and two virtual (horizontal). The boundary two have only three since their physical sites only have one bond. The tensor on each site represents the local Hamiltonian there, describing both interactions on the site itself (e.g. spin flip operators) and interactions between degrees of freedom on the site and neighbors.

A Hamiltonian can be written as an MPO, and in this form DMRG optimizes the ansatz towards the groundstate. In most systems, excited states have volume law entanglement and so DMRG cannot be used to extract the entire spectrum [53]. As originally formulated, only one site would be optimized at each step [221], but it is now common to optimize two tensors connected by a bond, since this provides some protection from getting trapped in local energy minima [180].

Other choices of MPO besides the Hamiltonian are possible - recent work [232] has proposed using a shift-and-invert approach (discussed in Sec. 1.2.2) to construct an MPO which can be used to target states deep in the many body band in the case those states are area law/low entanglement (as they can be in systems which are "many body localized" [19], an exception to the general situation for highly excited states discussed in Sec. 1.1). Another approach to finding such highly excited eigenstates which are area law begins with random MPS with structure similar to a state with conserved local integrals of motion, and optimizes for their overlap with the eigenstate of the Hamiltonian MPO in a local region, finding states with exponentially decaying "logical qubits" which the many body localized phase is expected to support [104, 90] (see Sec. 1.5 for a more

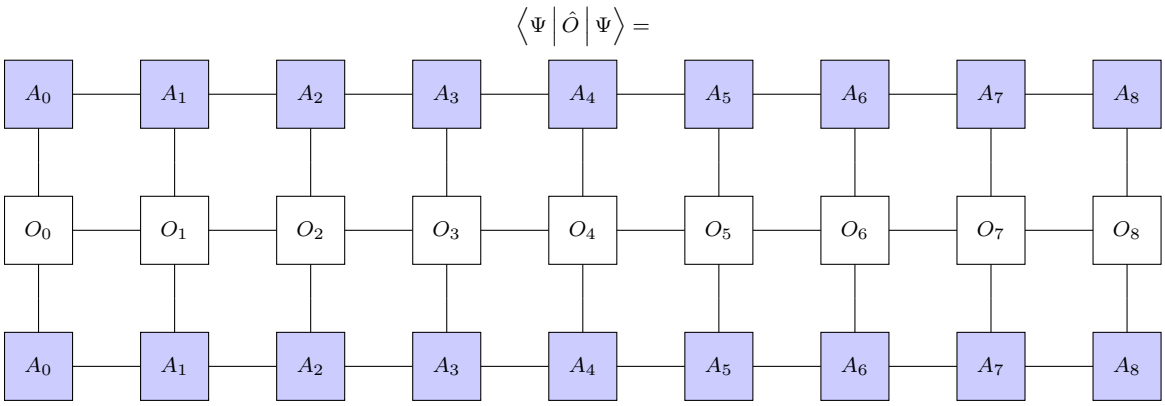

Figure 1.8: A graphical representation of computing an expectation value for an operator.

complete explanation of these l-bits).

To measure observables (correlation functions, etc.) with an MPS one writes the operator as an MPO "sandwiched" between two copies of the MPS (see Fig. 1.8) and traces over all connected lines, effectively performing $\langle \Psi | \hat{O} | \Psi \rangle$ [180].

From this perspective it is easier to understand why DMRG works so well on some states and so poorly on others. Systems in one dimension with gapped groundstates have area law entanglement [74], and in a purely 1D system this means the entanglement does not grow at all with the size of the subregion being considered. Even in a quasi-1D system, the perimeter of a subregion grows slowly enough that for states with low entanglement, an MPS representation will have bond dimension small enough to be feasible to use on current computing hardware.

Note that although MPS works best in (quasi)-1D systems, because of the particular area-law structure 1D states can possess, generalizations to higher dimensions exist which can accurately represent area law states [210].

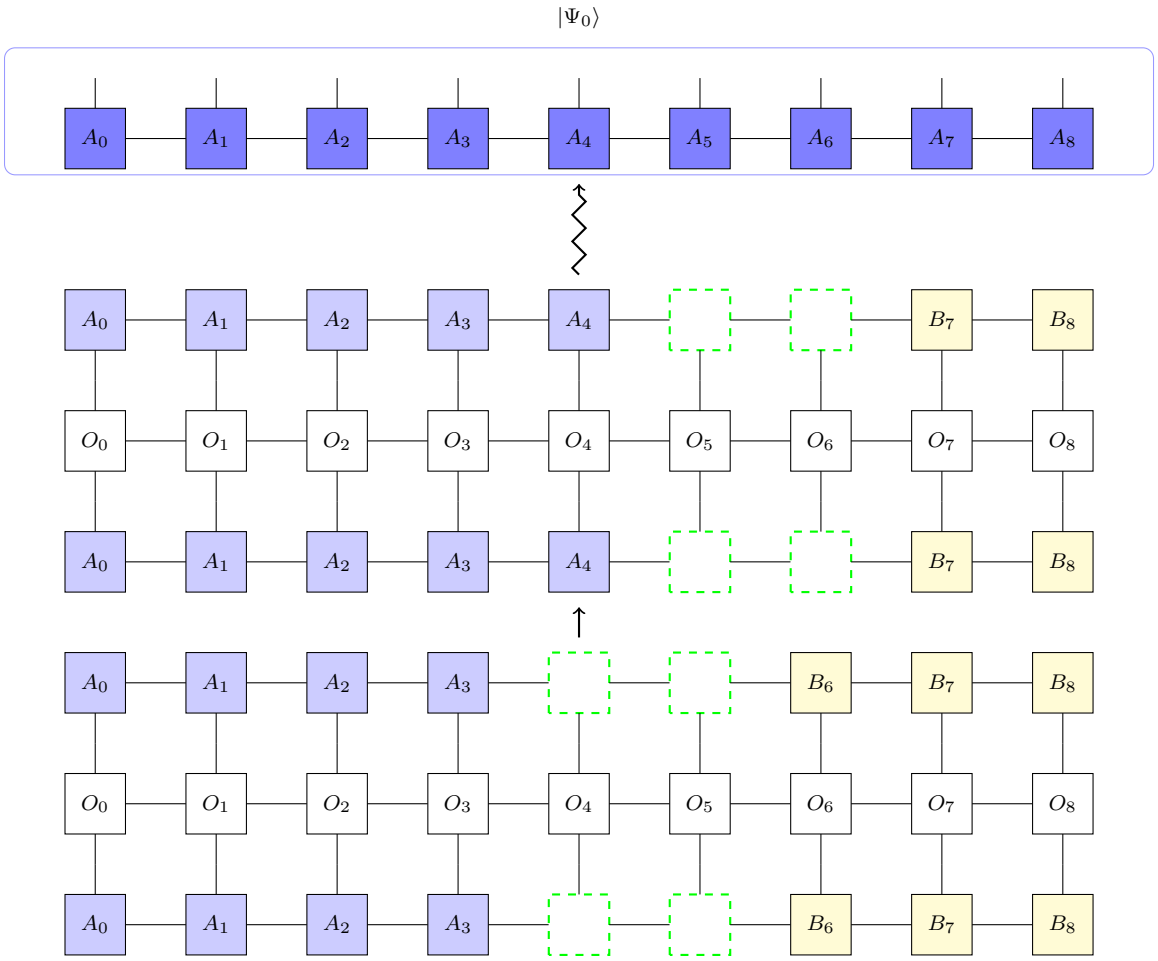

Figure 1.9: Sweeping procedure in DMRG. The tensors in the MPS shown with dashed boundaries are the ones optimized at each iteration step. After many steps (represented by the zigzag line) the MPS is optimized to the groundstate.

1.4.2 MERA

The multi-scale entanglement renormalization ansatz (MERA), first proposed by Vidal [213, 214], is another special tensor network ansatz which can efficiently represent certain wavefunctions in any dimension. Unlike MPS, which is essentially "flat", a MERA has a layered structure which is visualized in Fig. 1.10.

As Refs [213, 214] explain, MERA takes advantage of the fact that most interesting models have local interactions, which constrains their groundstates to have degrees of freedom which can be decoupled from each other through disentangling. The MERA combines these disentangling steps with coarse-graining after the degrees of freedom are decoupled, which imposes a particular structure on the tensor network. This structure allows changes in "higher" levels to propagate through effective time in an efficient way because the light-cone of any tensor high in the circuit has bounded growth [56].

The disentanglers in a MERA are unitary quantum gates. They address neighboring sites, which is not a restriction of tensor networks in general - one can devise other structures in which connections of any length are possible. Each site in a layer is only affected by one disentangling unitary at circuit gate depth τ, so that the *parallel gate depth* of the layer of disentanglers is 1. The layer after a disentangling layer is composed of *isometries*, which take the outputs of the disentanglers and coarse-grain them to 1 site, similarly to the procedure in block-spin renormalization. Isometries can have a varying number of inputs - if they take 2 input qubits, the overall MERA is called "binary", and if they take 3 input qubits, the MERA is called "ternary". "MERA" describes a family

of variational ansätze with very similar structure but which can vary slightly in details. At the end of the disentangle – coarse-grain – disentangle procedure the lattice will have been coarse-grained to one remaining tensor. By tracing the bonds backwards through "time" (the layers of the MERA) the wavefunction on any site can be reconstructed. The rules for how to construct each layer in the MERA ensure the total number of layers scales as $T \propto \log N$ where N is the number of sites in the lattice. The proportionality constant depends on the precise structure of the network [214].

A slight modification allows MERA to represent scale invariant states on systems of infinite size - critical systems. All isometries are identical tensors w and all disentanglers are identical tensors u. The MERA has an infinite number of layers with no "cutoff" tensor t at the top as in the previous figures. The pair (u, w) can be iteratively optimized to represent the groundstate and from these the central charge of the conformal field theory corresponding to the lattice theory whose groundstate the MERA represents can be found [158].

Analogously to MPS, variational optimization algorithms to perform groundstate search using MERA exist [55]. Because of the greater complexity of MERA, which gives it is expressive power, numerical work has been limited, although studies of lattice gauge theories [201] and critical states on boundaries [54] have been performed. The description has proved useful in analytic studies [2, 109, 41, 199, 211], and widespread numerical implementations may be forthcoming soon [195].

In the previous section the name "matrix product state" follows naturally from the

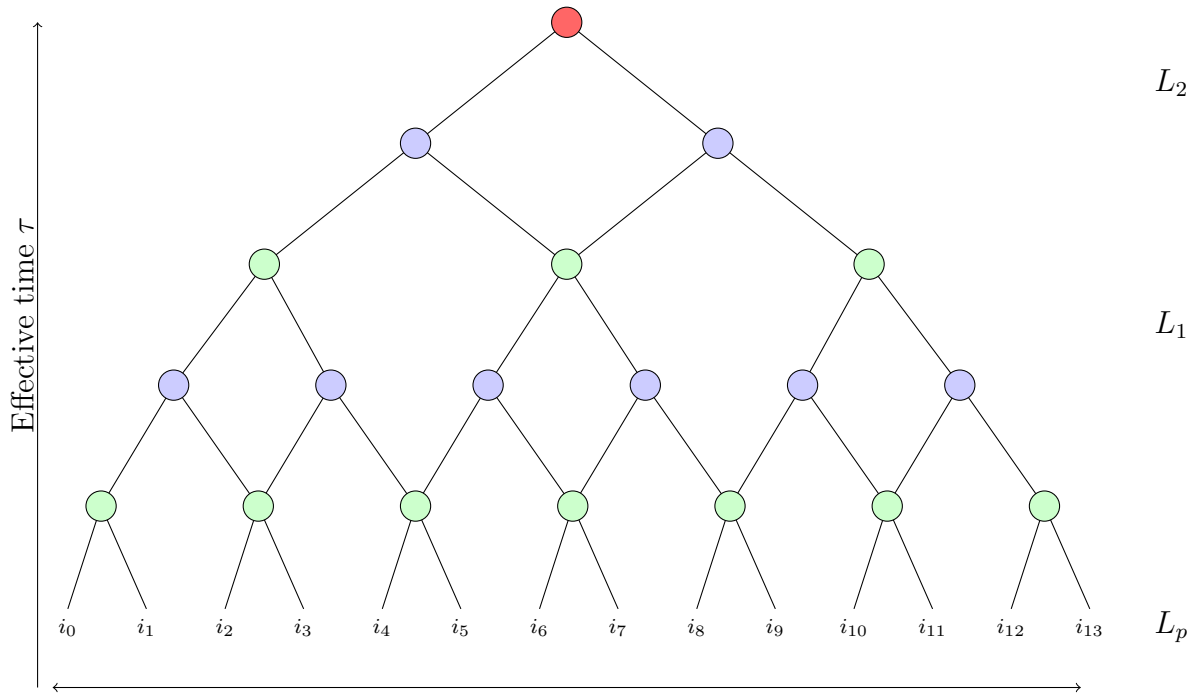

Figure 1.10: Example of a binary finite-depth MERA for a 1D system of 14 sites. At each higher level, sites are coarse-grained away. This allows the MERA to represent states of higher entanglement than an MPS can (efficiently) represent. The blue nodes represent disentangling unitaries, and the green nodes represent isometries, coarse-graining 2 sites into 1. Note the differing number of output qubits between the two types of node. The red node at the top of the circuit controls the dimension of the subspace of the Hilbert space on the physical lattice which this MERA will represent. Each L_i represents a coarse-grained lattice produced as the output of the combined disentanglers/isometries. Since this MERA is finite depth, it can represent states of finite correlation length.

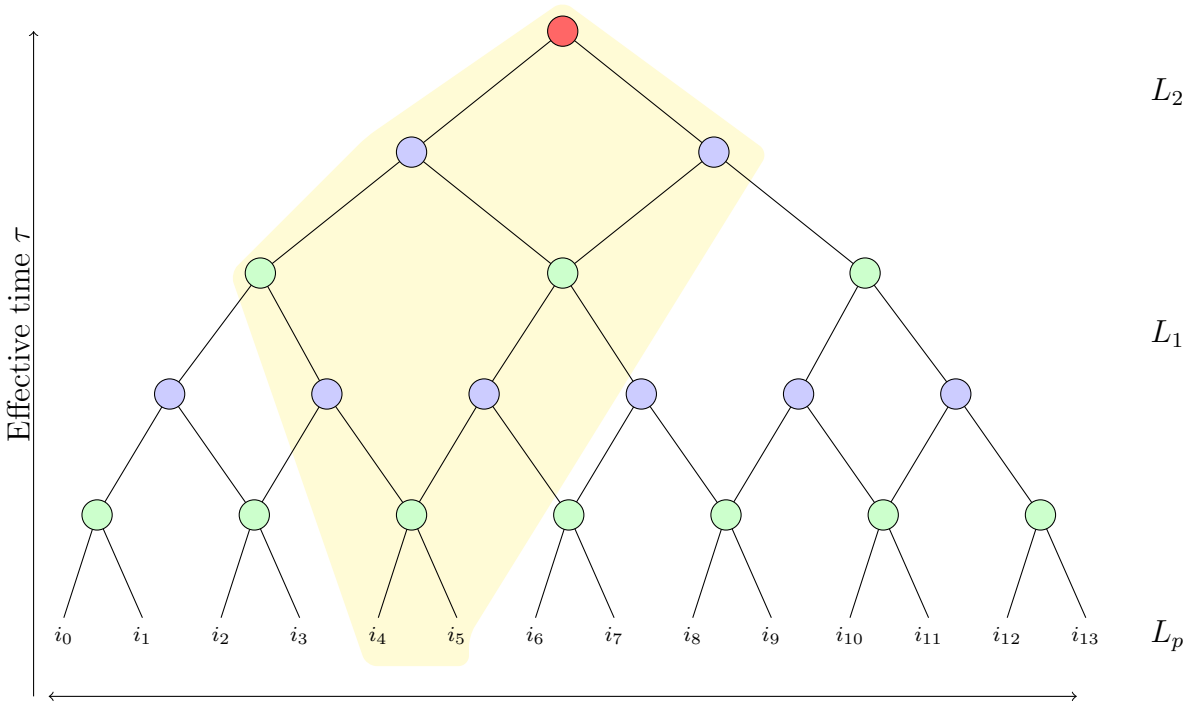

Figure 1.11: Causal lightcone for sites 4 and 5 in the MERA example from Fig. 1.10. This "lightcone" encompasses all tensors higher in the network which can affect the pair. At each effective time τ, the lightcone only touches 2 tensors at most.

fact that the MPS is an ansatz for a state involving taking products of 2-tensors (matrices). Similarly, "multi-scale entanglement renormalization ansatz" flows from the fact that a MERA's structure suggests a state with different ranges of entanglement: some short range entangled regions, which are quickly renormalized away in lower layers, and longer range entangled bonds, which are addressed as the layers are applied. The fact that MERA can represent states with such entanglement structure and that these representations are efficient to generate and manipulate (because of the lightcone structure seen in Fig. 1.11) enables MERA to handle a greater variety of states than MPS [56]. This entanglement – tensor network structure relationship has important connections to geometry and holographic duality.

1.4.3 Entanglement and Geometry

In some sense it seems obvious that there is a connection between tensor network states and geometry, since the previous two sections focus on networks with a pre-imposed structure and implicitly connect this structure with the kinds of wavefunctions each network family can efficiently describe. Can this relationship be made explicit and connected with other results about the connection between information and geometrical structure?

The entanglement structure of a state $|\Psi\rangle$ generates an "emergent holographic geometry". By entanglement structure, we mean whether long range entanglement exists, what lengths are dominant, etc. In particular we are interested in whether the state has "area law" entanglement, "volume law" entanglement, or intermediate scaling (as in a

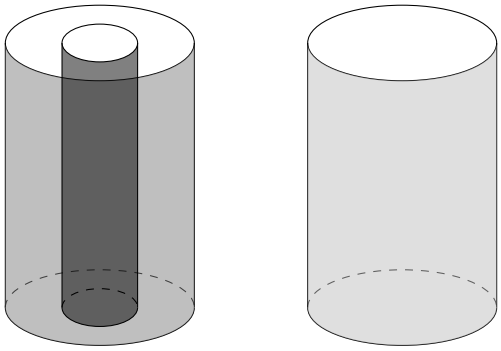

Figure 1.12: Diagrams of two AdS/CFT correspondences. On the left, a black hole corresponds to a thermal state of the CFT living on the surface, whose temperature is controlled by the black hole radius. On the right, a purely AdS bulk corresponds to the vacuum state of the CFT.

critical system) [35, 216, 95, 31]. States with non-trivial topological order also exhibit a constant contribution called the topological term [53].

The length scale in the entanglement structure of $|\Psi\rangle$ on a d-dimensional lattice is what generates the $d+1$-dimensional "holographic geometry" [56] Holographic duality forms a dictionary between a quantum field theory in a $d+1$-dimensional bulk and its d dimensional boundary, one aspect of which is this geometrical connection. The celebrated anti-de Sitter/conformal field theory (AdS/CFT) correspondence conjecture is an example of such a gauge/gravity duality [86].

In AdS/CFT there is a direct map between the gravity bulk theory (which is time-dependent) and the surface gauge theory which gives the CFT [86]. The dynamics of one of the two theories are accessible from the other through the mapping [129]. Some simple examples are shown in Fig. 1.12. The first principle of the correspondence is that $\mathcal{Z}_{CFT} = \mathcal{Z}_{AdS}$. This statement about the partition functions of the two theories generates all the specific relationships between transport coefficients and entanglement entropies,

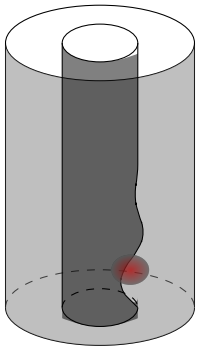

Figure 1.13: A perturbation to the black hole dies out over time according to its quasi-normal modes. This is detectable in the surface theory through various transport measurements (represented by the red hot-spot).

since in the non-holographic context we can calculate these quantities directly from $\mathcal{Z}$ [86]. Generally one "side" of the duality has a $\mathcal{Z}$ which is much easier to calculate and then this can be run through the map to find quantities much more difficult to calculate without the use of the duality.

Depending on the limit of strong or weak coupling the map has been used in different ways. Using a classical gravity theory in the bulk which is well understood allows us to probe theories on the surface which are difficult to understand using other methods (for examples see Refs. [93, 153, 73, 85]), forming the sub-field often called AdS/CMT. Conversely, simpler surface theories may have interesting quantum gravity duals in the bulk and again the mapping allows us to take statements about the correlations on the surface theory and rephrase them for the bulk. AdS/CFT duality has also uncovered new solutions in the bulk which are interesting to high energy theorists [60, 58, 50].

To give an example of the dynamical relationship, we can consider a bulk composed of a black hole . This maps to a thermal state of the surface CFT, with the surface

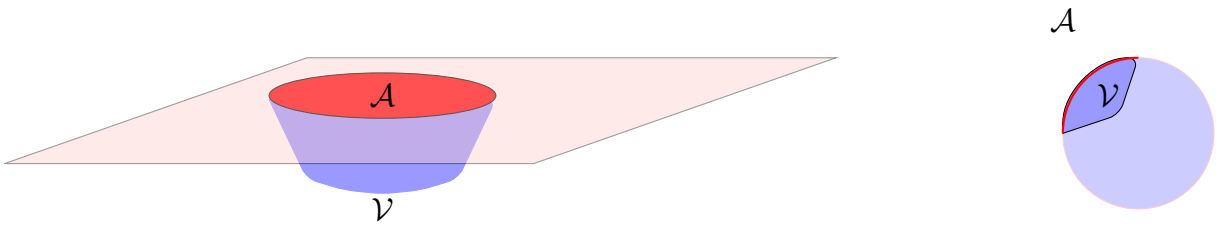

Figure 1.14: Minimal bulk volume $\mathcal{V}$ (in blue) for surface region (in red) $\mathcal{A}$. This minimal bulk volume contains the data needed to reconstruct the state of the CFT in $\mathcal{A}$ and vice-versa. The lighter shaded regions are the complement of $\mathcal{A}$ and the regions of the AdS dual outside the minimal surface $\mathcal{V}$.

temperature controlled by the black hole radius [129]. If the black hole is perturbed, it "rings" like a bell: it supports quasinormal modes [217, 160]. These damped oscillations eventually die away (like a bell's music) as the black hole returns to its steady state, and the damping process is controlled by the black hole and not the features of the perturbation [84]. In the AdS/CFT duality this damping can be viewed as a process of thermalization of the surface theory [84]. Additionally, the CFT's transport properties (such as ac or dc conductivity, thermal conductivity, etc.) are related by the map to the response of the black hole's horizon to perturbations [111], shown schematically in Fig. 1.13.

Entanglement plays an important role in this mapping. If a correspondence exists between a surface theory and a bulk theory, and we are interested in a compact region of the surface (we could equally well consider the bulk here of course), it is natural to ask how much of the bulk contains the information needed to reproduce the surface configuration? What shape should the bulk region have?

Ryu & Takanayagi [171] developed a formula to quantify this relationship in the

time-independent AdS/CFT context. It was later extended to the time-dependent case by Hubeny et al. [87]. In the time-independent case, shown in Fig. 1.14, a compact region $\mathcal{A}$ on the surface has a minimal bulk surface counterpart which contains all the information needed to reproduce the state on $\mathcal{A}$.

The volume $\mathcal{V}$ is the *minimal* volume with the same boundary on the surface as $\mathcal{A}$. Its shape is controlled by the bulk geometry (for instance, bulks with different curvatures will generate different shapes of $\mathcal{V}$). Black holes have a well-known area law for their entanglement entropy [76]:

$$S_{BH} = \frac{\text{Area (horizon)}}{4G_N} \tag{1.5}$$

And somewhat analogously, the entanglement entropy of the *surface* region $\mathcal{A}$ is expressible through this minimal surface $\mathcal{V}$:

$$S(\mathcal{A}) = \frac{\text{Area}(\mathcal{V})}{4G_N^{d+1}} \tag{1.6}$$

where G_N is Newton's constant. This demonstrates the important relationship between entanglement entropy of the surface CFT and the geometrical structure of the AdS bulk. In Chapter 4 we investigate a similar relationship. Our construction is somewhat different because we are working with lattice models and these statements are all for smooth classical manifolds. Additionally, our results are for an integrable free fermion CFT which may not be generic to 1+1D CFTs because of the integrability.

As shown by Swingle [198], the scale invariant MERA is an expression of aspects of the AdS/CFT correspondence. The CFT is the physical state, which lives on the surface of an emergent bulk AdS geometry. The holographic bulk here is the tensor network. The

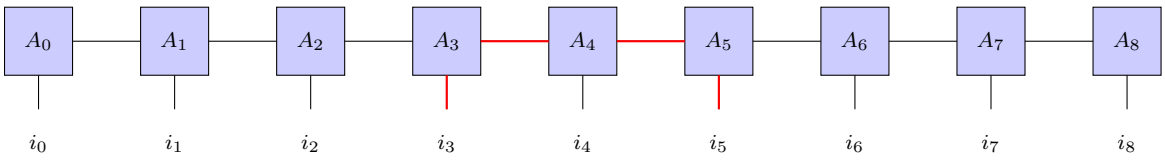

Figure 1.15: Geodesic (shown in red) in an MPS between sites 3 and 5. The geodesic distance has linear scaling with the physical distance.

relationship between correlations in the physical state on the boundary and the geometry in the bulk is accessible through geodesics. A geodesic is the shortest path between two locations in a metrizable space (one in which we have some notion of distance). In flat (Euclidean) space, the shortest path between two points is always a straight line. In spaces with non-zero curvature, this may no longer be the case. For example, in the positively curved space of the surface of the Earth, geodesics often take the form of arcs. Examining the relationship between the surface and bulk shortest distances allows us to determine the curvature of the bulk in holographic duality. These statements are about a restricted feature-set of the AdS/CFT map: they do not make any claims (yet) about dynamics or transport.

In an MPS (or its two-dimensional generalization PEPS), the geodesic length in the circuit scales linearly with the physical distance between lattice sites [56], and so MPS has a flat geometry, with zero curvature, as shown in Fig. 1.15. But a MERA, which can represent states with higher entanglement, may have a geodesic length which scales *logarithmically* with the physical distance [56] (in part due to the logarithmic layer structure of the MERA [198]). This is shown in Fig. 1.16.

MERA can represent area law states just as MPS can, and a finite-depth MERA can

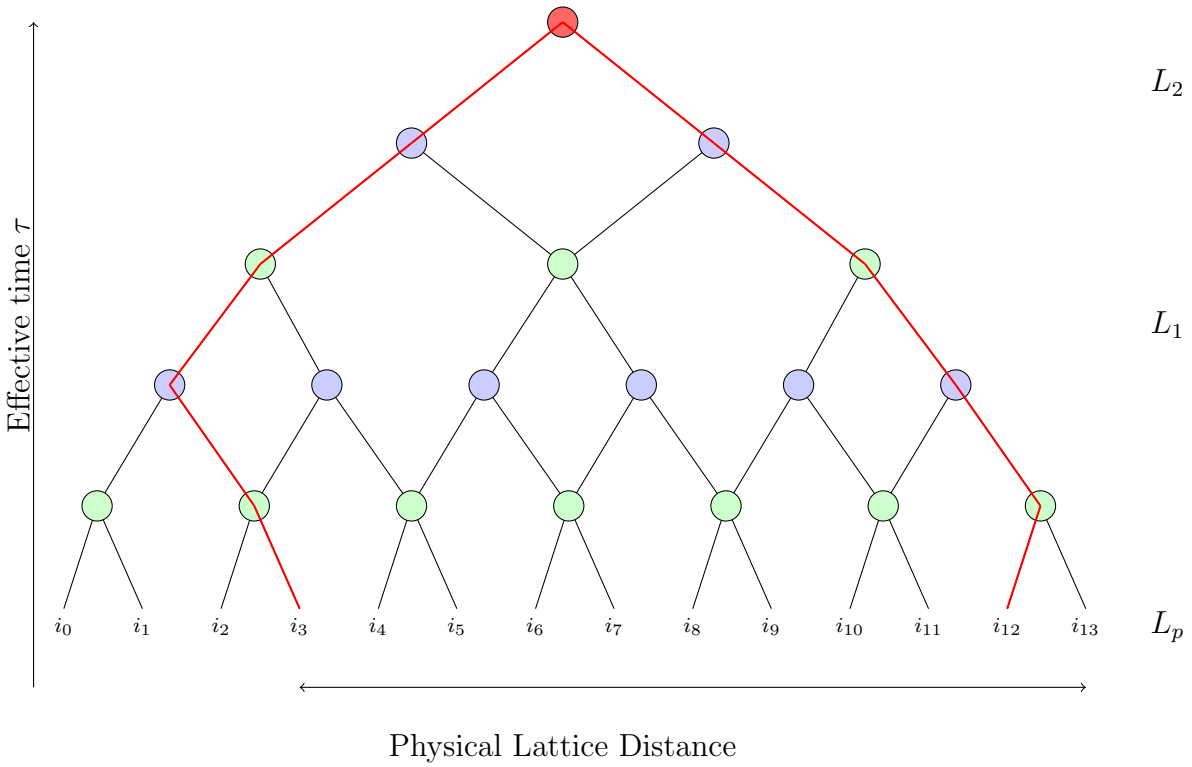

Figure 1.16: Geodesic (shown in red) in a MERA between sites 3 and 12. The geodesic distance has logarithmic scaling with the physical distance.

always be converted into an MPS (which might have large bond dimension) [214, 56]. The scale-invariant MERA, representing critical states, replicates the holographic duality of highly entangled states – hyperbolic geometry. The finite depth MERA, representing area law states, has the flat geometry of an MPS at long enough distances.

1.5 Many Body Localization and Thermalization

Most quantum many-body systems coupled to a large, continuous bath "thermalize" with the bath. By this we mean that such a system has no long-term local memory - a pure state prepared on the system will have its initial local information "washed out" into non-local observables which cannot be measured [146]. The system equilibrates with the bath and both settle to the same temperature, described by quantum statistical mechanics and the canonical ensemble.

What happens in the absence of a bath? An isolated quantum system prepared in a pure state undergoes unitary time evolution? The system is initially described by the microcanonical ensemble, but if it is allowed to evolve undisturbed for a long period of time, will it still "thermalize" so that its local observables match those of the equilibrium configuration described by the canonical example?

The eigenstate thermalization hypothesis (ETH) was developed to answer these questions. Consider preparing the isolated quantum system in a pure state $|\varphi(t=0)\rangle = \sum_{i=1}^{N} c_i |\psi_i\rangle$, where $\{|\psi_i\rangle\}$ are the eigenstates of the system's $N \times N$ Hamiltonian and $\sum_{i=1}^{N} c_i^2 = 1$, $c_i \in \mathbb{C}$. If one wanted to measure some local (meaning that it involves a

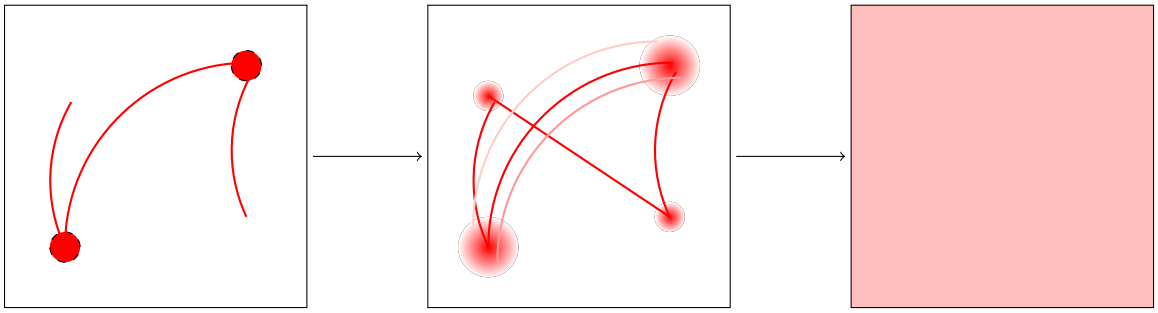

Figure 1.17: Interacting regions of an isolated quantum system act as baths for each other to drive the process of thermalization from an initial pure state with local information. The red lines represent long range resonances forming between regions.

number of sites that does not scale with the system size, e.g. a 2-local operator involves 2 sites) observable $\hat{O}$ at time t, the expectation value would be:

$$\left\langle \hat{O} \right\rangle (t) = \sum_{j=1}^{N} \sum_{k=1}^{N} c_k c_j^* \exp\{i(E_j - E_k)t\} \left\langle \psi_j \middle| \hat{O} \middle| \psi_k \right\rangle \tag{1.7}$$

The eigenstate thermalization hypothesis is that this expectation value approaches a single value at large t, that its variance as it approaches this value goes to zero, and that the single final value is the same as would be predicted if the system were coupled to the bath, and that all of this is true *even though the system is isolated* [49, 191]. At late times, the microcanonical and canonical ensembles will give the same answer. The interpretation is that the system is self-thermalizing, that is, different subregions act as baths for each other [106], inducing resonances across the system that enable thermalization, as shown in Fig. 1.17. In this way local information present initially is lost to non-local observables and a local region of the system has no long-term memory. Detailed numerical studies of candidate models for ETH suggest that the self-thermalization picture is the right one [166, 106]. Perfectly isolating a quantum system in an experiment is difficult but in

cold atom experiments with very weak coupling between the system under investigation and its surroundings, probing the dynamics of thermalization has been attempted [181, 28, 42, 188]. Recently, superconducting qubits have also emerged as a possible platform for experiments with isolated many-body quantum systems with disorder, which may host MBL physics [227]. Experiments similar to work discussed in Chapter 3 have also been performed, addressing the question of the stability (or lack thereof) of localized phases interacting with small quantum baths [169].

In the fully thermalized state, the system will have volume law entanglement. If a system supports thermalization, after a quantum quench occurs which introduces excitations correlations spread ballistically through the system [88, 208, 91], and eventually the entanglement entropy reaches the value predicted by the thermal density matrix $\hat{\rho}_{th,A} = \left[1/\operatorname{Tr}\{-\hat{H}_A/T_A\}\right] \times \exp\{-\hat{H}_A/T_A\}$, where T_A is the effective temperature on subregion A and $\hat{H}_A$ is the Hamiltonian on this subregion.

Systems which thermalize (obey ETH) have three features:

- Eigenstates close in energy have vanishing difference between each eigenstate in local observables. Stated another way, in a small window of finite energy density, local observables of eigenstates should be very close between eigenstates in the window if the system thermalizes.

- The reduced density matrix on a subregion of the system, acquired by tracing out the components of an energy eigenstate over the complement of that subregion, is equal to the thermal density matrix on that subregion, predicted by the canonical

ensemble.

- The value of a local observable of an eigenstate over time is essentially static, with small (if any) fluctuations, after a certain "pre-thermalization" time.

Most many-body quantum systems undergoing unitary time evolution thermalize in this manner. Most, but not all: a few interesting exceptions are known. Integrable systems, which have conserved integrals of motion, do not thermalize [177, 176, 167]. In 2006, another group of exceptions were proposed - the many body localized states [17]. Originally described as a generalization of the famous Anderson model for localization [9], a many-body localized phase can be found in a model with quenched disorder and interactions (which the Anderson model does not have). Allowing interactions may induce long-range resonances between particles and enable thermalization – the self-thermalization where sub-regions act as thermal baths for each other following and washing away local information into the global observables. However, if interactions are weak enough, a non-thermal phase may survive [17]. As Basko, Aleiner, and Altshuler (BAA) show in their seminal work, coupling to a continuous thermal bath (for instance, a crystalline system with phonons) or interactions strong enough to overpower the effects of disorder can thermalize the localized phase.In the dynamical picture of the quench discussed above, correlations (and entanglement) spread *sub*-diffusively [121, 88]. Another perspective [90] considers an Ising spin chain subjected to both random transverse and parallel magnetic fields on each site. The eigenstates of the Hamiltonian in this model form "logical bits" (l-bits), which are localized [104, 183, 88, 39]. The i-th eigenstate corresponds to set of

l-bits, each a localized packet of spin in a small, spatially local region of the chain. These logical bits emerge in the MBL phase and exist there only, and are not present in the thermalized phase. For a 1D disordered Ising or XXZ chain (see Eq. (1.5)) of length L in the localized phase, there are L logical bits, each one $\mathbb{Z}_2$ valued.

$$\hat{H}_{XXZ} = J_{XX} \sum_i \left(\hat{\sigma}_i^x \hat{\sigma}_{i+1}^x + \hat{\sigma}_i^y \hat{\sigma}_{i+1}^y \right) + J_Z \sum_i \hat{\sigma}_i^z \hat{\sigma}_{i+1}^z + \sum_i h_i \hat{\sigma}_i^z, \quad h_i \in [-W, W] \tag{1.8}$$

Eigenstates which are very close in energy differ in $O(L)$ of their l-bits, so that transitions between eigenstates are suppressed, since a large fraction of the l-bits would have to flip to make the transition from one eigenstate to another. This is one way to think about the concept of Fock space localization – just as hopping of particles is suppressed, so that the dc transport is zero, so is hopping between eigenstates, even if they are very close in energy. It also explains one of the ways in which MBL systems violate ETH: since states close in energy have very different l-bits, their local observables differ substantially. The values of these l-bits are also stable through time, so that the system cannot have its subregions act as thermal baths for each other. The l-bits can be constructed by "dressing" the physical spins with short-range local unitaries, generating a new set of pseudospin operators:

$$\hat{\tau}_i^{x,y,z} = \hat{U} \hat{\sigma}_i^{x,y,z} \hat{U}^\dagger \tag{1.9}$$

The $\hat{\tau}_i^z$ are l-bits and are eigenstates of $\hat{H}$. Rewriting the XXZ Hamiltonian in terms of these pseudospin operators leads to [39]:

$$\hat{H}_{LIOM} = \sum_i g_i \hat{\tau}_i + \sum_{i,j} J_{ij} \hat{\tau}_i^z \hat{\tau}_j^z + \sum_{i,j,k} J_{ijk} \hat{\tau}_i^z \hat{\tau}_j^z \hat{\tau}_k^z + \ldots \tag{1.10}$$

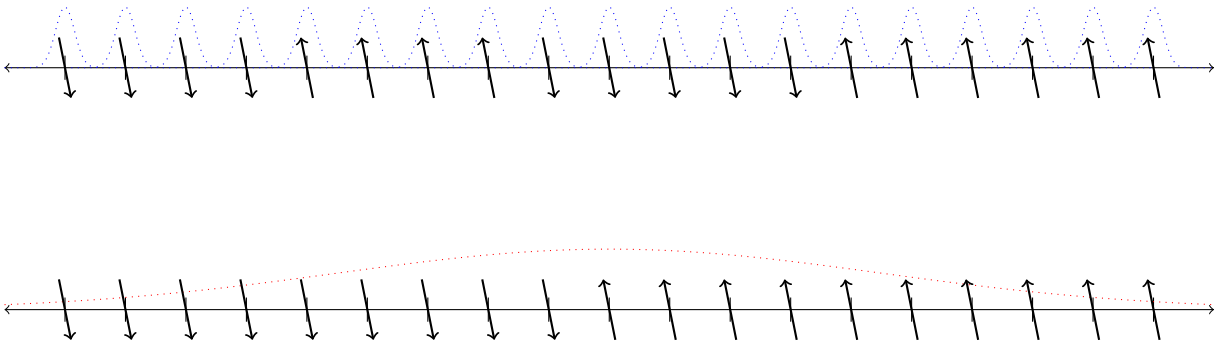

Figure 1.18: Top: a localized spin chain with l-bit envelopes. Bottom: a delocalized thermal version of the spin chain with extended band shown.

Where the J_n corresponding to n τ^z operators and sites decays exponentially in the maximum distance between any pair of sites. There is exponentially small overlap between these $\{\tau_z\}$ l-bits and the eigenvalues $\{\tau_z\}$ specify a unique eigenstate of $\hat{H}_{XXZ}$. This would be true of any Hamiltonian which supports the MBL phase, including the generalized André-Aubry models of spinless fermions in a quasiperiodic potential [146].

A schematic of the differences between the localized phase (with l-bits) and the delocalized one (with extended bands) is shown in Fig. 1.18. In this region of parameter space the eigenstates exhibit features of localization, in that they are area law and violate ETH, and this behavior survives to the thermodynamic limit. This construction does not rely on BAA-style arguments.

Many body localized phases violate the eigenstate similarity condition of ETH. Eigenstates very close in energy density may have very different local observables over long time frames. Localized states are area law, even deep in the many-body band [19] where they have high energy density, which violates the condition of replicating the thermal density matrix. As an MBL system undergoes unitary time evolution, it "heats up"

logarithmically in time to a volume law [184] but the final prefactor on this volume law is subthermal. In contrast to the ballistic spreading of entanglement in the ETH phase, in an MBL phase entanglement spreads sub-diffusively [184].

Many-body localization can also be produced in systems with a quasi-periodic potential, as in the generalized André-Aubry model [92]. MBL in these models is expected to have a variety of different features from the case of quenched disorder [92].

The stability of MBL is an important area of study with several outstanding questions. In the original 2006 proposal, the system needed to be perfectly isolated from a *continuous* thermal bath (this is the reason phonons cannot be present) [17]. Later work addressed the situation of a system which would on its own realize the MBL phase coupled to baths of varying size: a single thermal grain [48, 126], and a bath composed of free fermions similar in size to the system which would localize [145, 144, 96]. In Chapter 3 we investigate the ability of a system with quenched disorder which would localize were it isolated to overcome the resonance-inducing effects of a bath and how such a system evolves in time.

Since ETH is a statement about isolated quantum systems, experimental probes of thermalization have been difficult. As shown in Chapter 3, a system which would otherwise tend towards localization is quite easily destabilized towards thermalization even in the presence of relatively small baths. It is also an open question whether MBL physics can survive in two or three dimensional systems, which would be easier to access experimentally [48, 159]. Nevertheless, experiments in cold atoms [182, 28, 27, 42] have

provided some evidence for the existence of these phases. Devising signatures of localization which are accessible experimentally remains a challenge: experiments cannot easily measure entanglement entropies or level statistics or the variance of operator expectation values between eigenstates close in energy. Because most solid state systems have a "reservoir" of phonons, which can function as a continuous thermal bath, it is unlikely it will be possible to realize MBL physics in the standard solid-based experimental platforms of condensed matter physics.

1.5.1 The Localization Transition

Unlike other quantum phase transitions, the MBL-ETH transition may involve the entire spectrum crossing from area-law to volume-law at once. Many body mobility edges, which would occur if there are parameter regions where all eigenstates below some cutoff energy are localized and all eigenstates above are delocalized, have been proposed [127, 18], but there are also arguments against their existence [46]. These "eigenstate transitions" are a dramatic departure from other cases, where the transition involves the groundstate and low-lying excitations and high energy excited states are mostly insensitive to the change.

The MBL physics in quasiperiodic models (such as the André-Aubry family) is distinct from the MBL physics in the quenched disorder context [185, 92, 119]. In the quasiperiodic case the rare region/Griffiths effects are not present [92] and the transition between these MBL phases and the ETH regime is governed by a different universality class than the similar transition between MBL in quenched disorder models and ETH [105, 119]. A

variety of questions remain open about the transition(s) between an ETH phase and an MBL phase. In the quenched disorder case, what role do rare metallic regions play? How do they grow? Conversely, coming from the thermal side, how do extended, delocalized bands "freeze" into the localized phase [66]? The structure of entanglement through the transition, while important, remains poorly understood [69]. Also unresolved is the possible presence of an intermediate phase which is not fully localized but which also does not satisfy ETH [146].

1.5.2 Numerical Methods for MBL

The best current numerical approach to the MBL-ETH transition is exact diagonalization [4]. Many disorder realizations must be computed to acquire accurate statistics, and studies have so far been limited to 30 sites or fewer [193]. The shift and invert method discussed previously is the state of the art exact diagonalization approach to understanding MBL systems.

Devising quantum Monte Carlo schemes to extract high energy density eigenstates is very difficult. Generically these states will have nontrivial sign structure, unlike ground-states, even if the particles in the system are bosons [37]. Using $(\hat{H} - \sigma\hat{\mathbb{I}})^2$ to try to target states in the middle of the band will not help, since one of $\hat{H}$ or $\hat{H}^2$ will have a sign problem.

As mentioned in Sec. 1.4.1, the discussion of matrix product states and DMRG, algorithms exist to target many-body eigenstates deep in the band when the system is

localized. However, since these methods are MPS-based, the closer to the transition to a thermal phase they are used the worse their performance. On the thermal side of the transition, the entire band may be volume law, exactly the situation where these tensor network approaches struggle most. Thus, to determine how a thermalizing system undergoes localization will require new numerical methods, which can find and describe states on both sides of the MBL-ETH transition. In Chapter 4, we discuss preliminary work in this vein, developing a new algorithm to generate tensor networks for a wide variety of wavefunctions, making connections to holography (similar to the connections discussed in Sec. 1.4.3), with an eye towards extending this work to the interacting (many-body localized) realm.

Chapter 2

Projector Monte Carlo Study of a Four Fermion Ring Exachange Model

Materials, such as cuprates, which exhibit high T_c superconductivity have phase diagrams with many common features. Among these features is the presence of a bad metal phase bordering a region showing pseudogap behavior. The bad metal phase has linear T resistivity suggesting that it is a non-Fermi liquid (n-FL). To better understand superconducting materials, it then behooves us to search for evidence on strange metal phases in itinerant two-dimensional electronic systems.

A minimal model for cuprates is the one-band Hubbard model. A perturbative expansion of this model results in a number of terms including a hopping term (t), a Heisenberg

exchange term (J) and ring exchange term (K) suggesting a $t-J-K$ model,

$$\begin{aligned}\hat{H}_{tJK} =& t\sum_{\langle i,j\rangle}\hat{c}_i^\dagger\hat{c}_j + \text{h.c.} + J\sum_{\langle i,j\rangle}\hat{\mathbf{S}}_i\cdot\hat{\mathbf{S}}_j + K\hat{H}_\square \\ \hat{H}_\square =& \sum_i \hat{c}^\dagger_{i+\hat{x},\uparrow}\hat{c}_{i+\hat{x}+\hat{y},\uparrow}\hat{c}^\dagger_{i+\hat{y},\downarrow}\hat{c}_{i,\downarrow} + \\ & \hat{c}^\dagger_{i+\hat{y},\uparrow}\hat{c}_{i+\hat{x}+\hat{y},\uparrow}\hat{c}^\dagger_{i+\hat{x},\downarrow}\hat{c}_{i,\downarrow} + \text{h.c.} + \uparrow\leftrightarrow\downarrow \end{aligned} \tag{2.1}$$

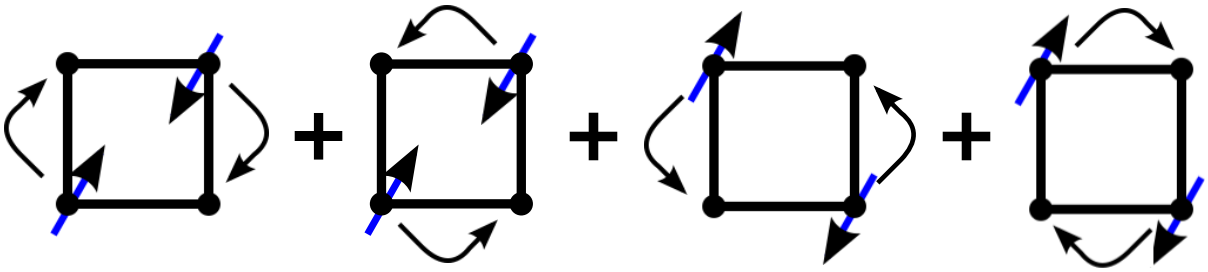

Figure 2.1: Schematic illustration of $\hat{H}_\square$.

as a reasonable approximation of the Hubbard model in certain regimes. A similar Hamiltonian can also be derived from an RPA approximation of the screened Coulomb interaction in the 2D planes Unfortunately, this Hamiltonian has a fermion sign problem and although DMRG studies [136] find numerical evidence of a d-wave Bose metal on two-leg ladders, establishing anything definitive about the two-dimensional limit has proved difficult. The sign problem arises when t or J is non-zero when $K<0$. The K-only Hamiltonian commutes with the total number of electrons on each row/column as well as the S_z of the two sub-lattices A and B; therefore, these quantities are conserved

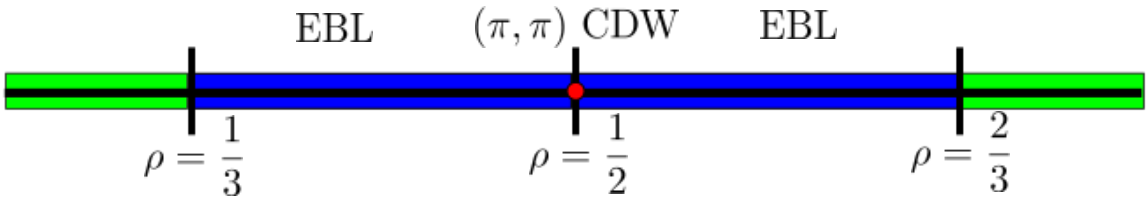

Figure 2.2: Phase diagram for the fermionic ring-exchange model.

throughout the simulation. All data presented is where the number of electrons are the same for each row/column and the $S^z = 0$ on both sub-lattices.

In this work, we report strong numerical evidence for a non-Fermi liquid phase as the ground state of an itinerant two-dimensional electronic model. In particular, we consider the K-only model ($t = 0,\ J = 0$) showing that it is sign-free (see appendix XXX) allowing for statistically exact quantum Monte Carlo simulations to be performed in the two-dimesional limit. We perform Green's Function Monte Carlo [206] to examine the phase diagram of the ring-exchange model for spinful fermions. Studying this model as a function of electron density, we find a strange metal phase which has the properties of the extremal d-wave local Bose liquid (e-DLBL), originally suggested as a potential ground state for this model by ref. [142]. Numerically, we find a charge sector which is an e-DLBL and a spin sector which appears to be weakly antiferromagnetic. The e-DLBL has been seen as the ground state of a bosonic ring-exchange model [154],[202]. In addition to finding the e-DLBL, we identify densities where the ground state of the Hamiltonian is a charge density wave (CDW) or phase separates. Fig. 2.2 presents a summary of our phase diagram.

2.1 Numerical Methods

We use diffusion Monte Carlo (DMC) (see 1.3.1)), a type of projector quantum Monte Carlo, to investigate the groundstates of $\hat{H}_{\square}$ (2.1) and its phase diagram for the fermions, carrying both spin and charge. DMC, like all projector Monte Carlo algorithms, works by stochastically applying a propogator (in our case $\hat{G} = \hat{1} - \tau\hat{H}_{\square}$) to a trial wavefunction, driving the system to its groundstate at zero temperature. We choose a wavefunction whose amplitude is constant but whose signs are chosen to correspond to their known ground state values as our trial state. Projector methods avoid the need to update sections of a path and so are not affected by the presence of hard-core constraints in the way that other Monte Carlo methods, such as worldline or stochastic series expansion, are. The trade-off in this method is that it most naturally samples $|\Psi|$ instead of $|\Psi|^2$; to resolve this, a forward walking correction [98],[29] is used. We use a parallel implementation of the fixed population GFMC algorithm, with forward walking 1.3.2 and population bias control 1.3.3 to control systematic errors.

We performed the simulation with 10^4 walkers, up to a β of 80, using the `C++ STL MT19937` pseudo-random number generator. We peformed forward walking up to β of 5, with 600 steps of population bias control.

2.2 The Charge Sector

We look for various charge-ordered phases using the charge structure factor,

$$S_C(\mathbf{q}) = \frac{1}{L^2} \sum_{i,j} e^{\{i\mathbf{q}\cdot(\mathbf{r}_i - \mathbf{r}_j)\}} \left(\langle \hat{n}_i \hat{n}_j \rangle - \langle n \rangle^2 \right) \tag{2.2}$$

Where $\hat{n}_i$ is the density operator at site i.

At low and high filling ($\rho \leq 1/3, \rho \geq 2/3$) we see phase separation which we can diagnose in the charge structure factor based on the presence of Bragg peaks at small wavevector. The $S^z_A = S^z_B = 0$ sector is lowest in energy. These constraints prevent full phase separation and instead we find 'stripes' which maximally phase separate the system under these constraints. This is consistent with previous DMRG studies on two-leg ladders of the full $t - J - K$ model at $\rho = 1/3$ which also saw phase separation when $K \gg t, J$ [94].

At exactly half filling ($\rho = 1/2$) we find a (π, π) charge density wave identified by the Bragg peaks at $(\pm\pi, \pm\pi)$ in the structure factor, shown in Fig. 2.3. The peaks appear to persist as the system size grows (shown by the black line in fig. 2.4), suggesting that the CDW order is the underlying phase in the thermodynamic limit. Notice, though, that even at half filling there is an unusual cross structure in the rest of the structure factor.

At intermediate filling ($1/3 < \rho < 2/3, \rho \neq 1/2$), we observe clear signals of the extremal d-wave Bose liquid phase in the charge sector. These are a) the abscence of Bragg peaking (no charge ordering), which seems to persist under finite size scaling; and b) the presence of the singular lines in the charge structure factor which are theoretically identified with the presence of a Bose surface [154]. Near the Bose surface we expect to

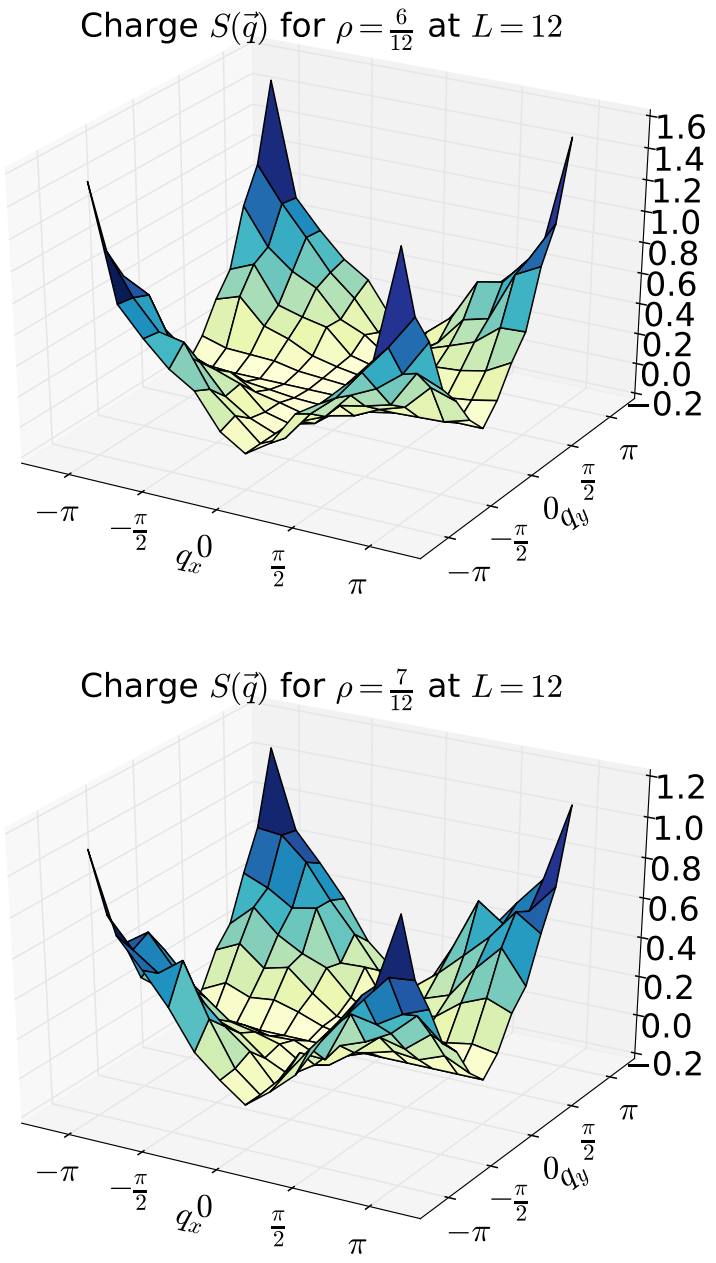

Figure 2.3: Charge structure factors for $L = 12$. Top figure shows $\rho = 1/2$ and lower figure shows $\rho = 7/12$.

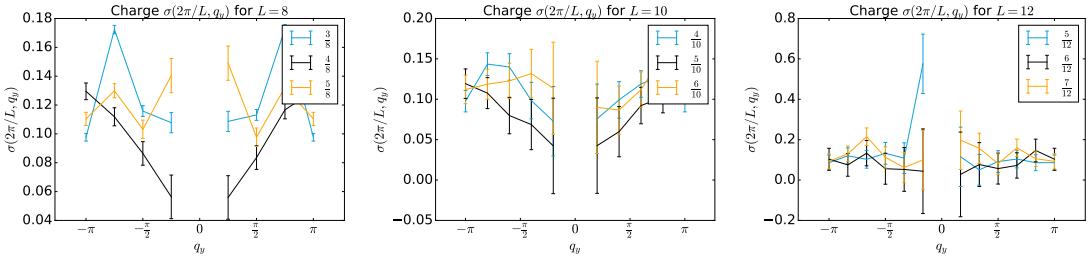

Figure 2.4: $\sigma(\mathbf{q})$ for various L

.

see linear dependence of $S_C(\mathbf{q})$ on $\mathbf{q}$. We test for this by examining the slope of $S_C(\mathbf{q})$ at small $|\mathbf{q}|$ - we divide $S_C(\mathbf{q})$ by the EBL theory result

$$S_{eDLBL}(\mathbf{q}) = 4 \left| \sin \frac{q_x}{2} \sin \frac{q_y}{2} \right| \tag{2.3}$$

If the ratio $\sigma(\mathbf{q}) = S_C(\mathbf{q})/S_{eDLBL}(\mathbf{q})$ does not go to zero as $|\mathbf{q}| \to 0$, then $S_C(\mathbf{q})$ has linear slope, suggesting the presence of a gapless bosonic phase - the e-DLBL. As the system size increases, $\sigma(\mathbf{q})$ does not appear to trend towards zero, as shown in fig. 2.4. The linearity of $S_C(\mathbf{q})$ persists to smaller and smaller wavelengths. The specific prefactor in $S_{eDLBL}(\mathbf{q})$, in this case 4, is not expected to be universal. This explains why different sized lattices may show peaks of different heights in $\sigma(\mathbf{q})$. The combination of the presence of the node-lines and linear behavior of $S_C(\mathbf{q})$ is strong evidence for the presence of the e-DLBL phase in the charge sector, away from half filling.

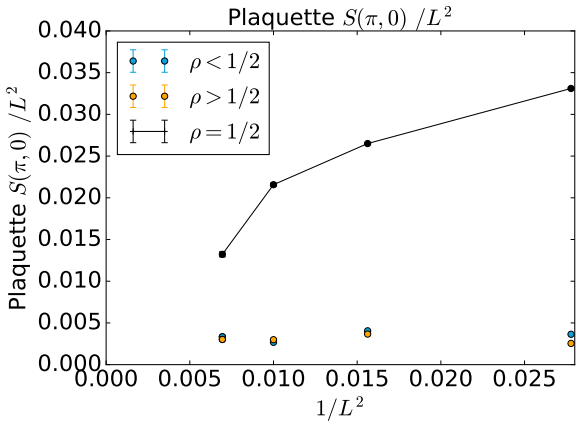

Figure 2.5: Finite size scaling for the plaquette structure factor.

2.3 Excluding Valence Bond Order

$$\hat{P}_i = \hat{c}^\dagger_{i+\hat{x},\uparrow}\hat{c}_{i+\hat{x}+\hat{y},\uparrow}\hat{c}^\dagger_{i+\hat{y},\downarrow}\hat{c}_{i,\downarrow} +$$

$$\hat{c}^\dagger_{i+\hat{y},\uparrow}\hat{c}_{i+\hat{x}+\hat{y},\uparrow}\hat{c}^\dagger_{i+\hat{x},\downarrow}\hat{c}_{i,\downarrow} + \text{h.c.} + \uparrow\leftrightarrow\downarrow$$

$$S_P(\mathbf{q}) = \frac{1}{L^2}\sum_{i,j} e^{\{i\mathbf{q}\cdot(\mathbf{r}_i-\mathbf{r}_j)\}}\left\langle \hat{P}^2_i \hat{P}^2_j \right\rangle$$

This operator measures whether a plaquette is "hoppable" and its structure factor show no signs of order, as discussed in appendix xxx and shown in Fig. 2.4. This rules out a valence bond solid phase. By measuring correlator $\hat{P}_i$ and examining its structure factor we can exclude the presence of a bond solid. Similar to the spins, if there is order present it will be at $\mathbf{q} = (\pm\pi, 0)$ or $\mathbf{q} = (0, \pm\pi)$ (since the hopping must occur in the $\hat{x}$ or $\hat{y}$ direction from site i). For half filling, the order parameter plotted in Fig. 2.5 does not

tend to zero because it is "carried along" by the CDW order, but in the more interesting regime where the e-DLBL is expected we see that the plaquette structure factor trends to zero - there is no bond order. Similarly, for *two* site operators

$$\begin{aligned}
\hat{B}_{x,i} =& \hat{c}^{\dagger}_{i+\hat{x},\uparrow}\hat{c}_{i,\uparrow} + \text{hc} + \uparrow\leftrightarrow\downarrow \\
\hat{B}_{y,i} =& \hat{c}^{\dagger}_{i+\hat{y},\uparrow}\hat{c}_{i,\uparrow} + \text{hc} + \uparrow\leftrightarrow\downarrow \\
S_{B,x}(\mathbf{q}) =& \frac{1}{L^2}\sum_{i,j} e^{\{i\mathbf{q}\cdot(\mathbf{r}_i-\mathbf{r}_j)\}} \left\langle \hat{B}^2_{x,i}\hat{B}^2_{x,j} \right\rangle \\
S_{B,y}(\mathbf{q}) =& \frac{1}{L^2}\sum_{i,j} e^{\{i\mathbf{q}\cdot(\mathbf{r}_i-\mathbf{r}_j)\}} \left\langle \hat{B}^2_{y,i}\hat{B}^2_{y,j} \right\rangle
\end{aligned}$$

We can perform a similar analysis, where we see:

2.4 The Spin Sector

Having established the properties of the charge sector, we can then consider the spin sector. There is no evidence of any ordering in the spin structure factor. In particular, the peaks at $(\pm\pi, 0)$ and $(0, \pm\pi)$ at various system sizes stay constant (see fig. xxx). The values of $S_S(\pm\pi, \pm\pi)$ are directly related to the differences between S^z_A and S^z_B, the total S^z quantum numbers on sublattices A and B respectively, which are conserved in our simulation. Finite size scaling analysis, shown in Fig. 2.4, suggests that the system is not antiferromagnetically ordered away from half filling. We have also ruled out the

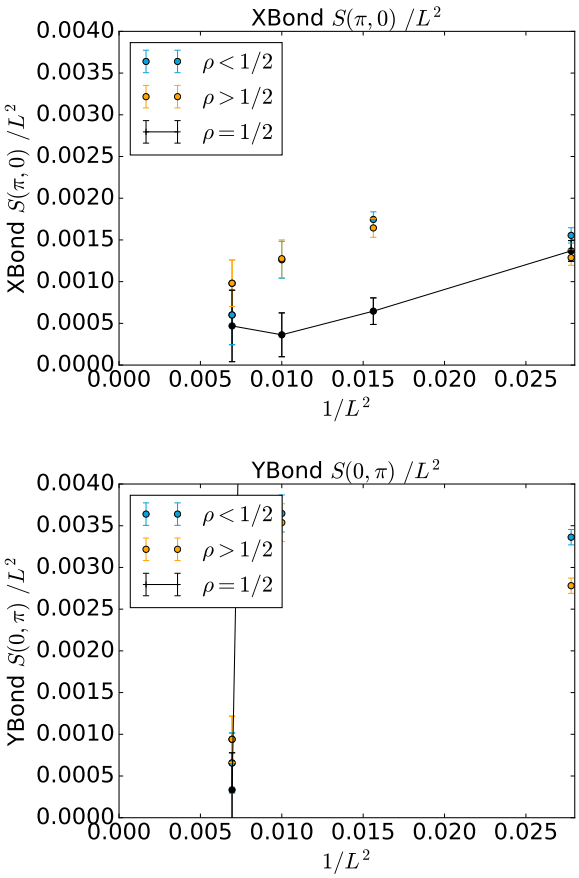

Figure 2.6: Finite size scaling for the bond structure factors.

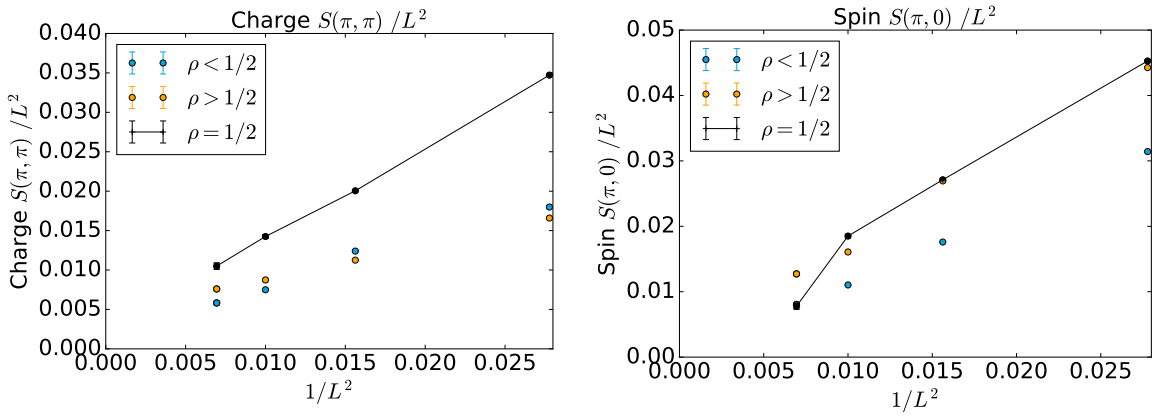

Figure 2.7: Finite size scaling for charge and spin order parameters. Note that although the densities less than half are rendered in the same colour, they are *not* exactly the same filling fraction (e.g. $\frac{5}{12} \neq \frac{4}{10}$ - they are similar, but not quite the same.

possibility of a valence bond solid by measuring relevant correlators.

It appears that the spin structure factor has weak Bragg peaks at $(\pm\pi, 0)$ and $(0, \pm\pi)$ - a signature of antiferromagnetism.

2.5 *d*-wave Bose Liquids

A wealth of experimental data suggests that the groundstate(s) of the high T_c cuprates in the pseudogap phase are described by non-Fermi liquids with gapless modes, no broken symmetries and no condensation. Near the transition to the superconducting state ARPES suggests that vortices bind together, but since the system is not superconducting these vortices cannot be condensed. *d*-wave correlated Bose liquids, also called "Bose metals", are a class of critical quantum fluids of *uncondensed* pairs of vortices/holons. First developed by [142], these states can be described using "doubly-slaved" electrons.

The electrons are broken down into a fermionic spinon f and bosonic chargon b, and further writing the chargon as a product of two spinless fermions d_1 and d_2.

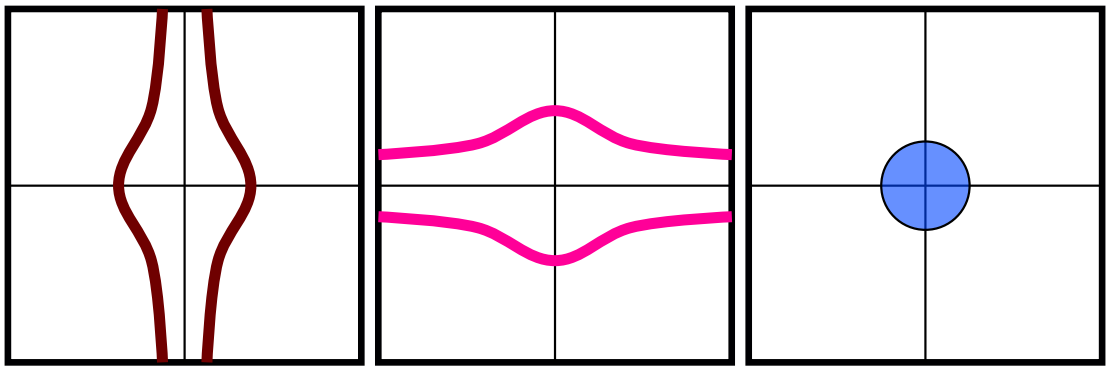

Figure 2.8: Schematic illustration of the parton wavefunctions. The full electron wavefunction $|\Psi\rangle$ is a product of these four Slater determinants.

d_1 (d_2) preferentially hops vertically (horizontally). The Fermi surfaces of each of d_1, d_2 are therefore ovoids, which may be closed (the d-wave Bose liquid - DBL) or open to the edge of the Brillouin zone (the d-wave local Bose liquid - DLBL), shown in Fig. 2.8. The width of the ovoids is controlled by the filling fraction if $t \neq 0$. The *exciton Bose liquid*, first proposed by Paramekanti et. al.[154], is analagous to an extremal limit of the DLBL. If $t, J \to 0$, the Fermi surfaces collapse onto the $q_x = 0$, $q_y = 0$ lines. There are two gapless node-lines for the boson b. The EBL and eDLBL phases are expected to be unstable to a (π, π) charge density wave at half filling if only nearest-neighbour ring exchange is present - Umklapp terms destroy the liquid[202]. At low density ($\rho < 1/3$), the system is expected to phase separate into "stripes" of CDW and vacuum. Since the Hamiltonian preserves the number of particles per row and column, the system cannot

fully phase separate. In this region the Hilbert space is highly sectorized because the stripes cannot move coherently. In the intermediate region, $1/3 < \rho < 1/2$, whether the EBL is stable at large system size was unclear[202]. For the spinful fermions the K_1 only model is the only one which is sign free. For the bosons it is possible to stabilize the EBL by including next-nearest-neighbour ring exchange terms, on a 2×1 or 1×2 plaquette. This also may allow the emergence of a VBS phase at half filling. The addition of even a tiny t hopping will introduce a sign problem and most likely destroy the EBL, but a state in the broader class of DLBL wavefunctions is still possible and likely for small enough t/K.

2.6 Extensions to Larger Systems

Beyond $L = 12$ it becomes difficult to overcome the statistical limitations of the DMC approach using currently available. There are several contributing causes:

- Correlators along the forward walk length must converge for a specific simulation τ. This requires comparing many forward walking steps, each of which is very expensive to compute correlations for.

- Population bias correction for the correlators should converge in both the number of walkers and in the number of population bias corrected steps. This requires checking multiple population bias correction step counts for very large population sizes, which is numerically difficult for large L.

These difficulties can be mitigated by choosing a smaller τ time slice, but this then requires running the simulation much longer so that the walkers can converge into the groundstate. As such, testing that measurements are reliable for a specific choice of τ, forward walking steps, population size, and population bias correction steps is extremely computationally intensive. Although we have performed simulations for $L = 14, 16$, which are suggestive of the presence of the e-DLBL phase, it was not possible to definitively state whether the above convergences were robust. This would be worthwhile to investigate in future work.

2.7 Conclusions

We have established the presence of the EBL phase in the charge sector up to lattice sizes 12×12. Finite size scaling analysis suggests the e-DLBL phase may be stable away from half filling to the thermodynamic limit. In the spin sector we detect signatures of weak anti-ferromagnetic ordering. It would be interesting to be able to measure the "box correlators" of [142],[202] to probe the length of the excitons in the EBL, but in our framework this is not possible.

2.8 Acknowledgements

We thank Ryan Mishmash, Olexei Motrunich, and Jim Garrison for useful discussions.

This material is based upon work supported by the National Science Foundation

Graduate Research Fellowship under Grant No. DGE 1144085. Any opinion, findings, and conclusions or recommendations expressed in this material are those of the authors(s) and do not necessarily reflect the views of the National Science Foundation.

We acknowledge support from the Center for Scientific Computing at the CNSI and MRL: an NSF MRSEC (DMR-1121053) and NSF CNS-0960316.

Chapter 3

Many-body localization in the presence of a small bath

3.1 Introduction

While it has become clear in recent years that the eigenstate thermalization hypothesis (ETH) [49, 191] provides the correct picture for the emergence of quantum statistical mechanics in broad classes of closed quantum systems [166], the phenomenon of many-body localization (MBL) [9, 18, 17, 67] has appeared as a scenario where quantum statistical mechanics is robustly violated. By now, overwhelming numerical [149, 208, 152, 16, 91, 19, 107, 127], analytical [90] and experimental [108, 181, 188, 26] evidence has been amassed that a many-body localized phase exists in strong disorder and for finite-strength interactions (for a recent review, see Ref. [146]). The violation of

ETH most prominently manifests itself in an area law for the entanglement entropy in highly excited eigenstates [19]: unique to an MBL system, the entanglement entropy of a region scales only with the size of the boundary of that region in almost all states of the many-body energy spectrum. Other key properties of MBL phases include a discrete local spectrum and vanishing conductivity [18, 17], a logarithmic growth of entanglement entropy [208, 16, 184], and a complete set of local integrals of motion that describe the entire many-body spectrum [89, 183].

The description of many-body localization generally assumes a system that, in the limit of vanishing electron-electron interactions, becomes an Anderson insulator in which all single-particle states are localized. The eigenstates of a many-body localized system are connected to the eigenstates of the Anderson insulator by a finite-depth local unitary transformation [19]. Recent work [123, 138, 220] has raised the question of whether MBL can also exist in a system where in the non-interacting limit, a critical single-particle energy, the mobility edge, separates localized and delocalized states. In one dimension, this can be achieved in certain types of quasi-disordered systems, and it is a generic scenario in higher dimensions. For a particular incommensurate potential, Ref. [123] found three regimes: a many-body localized phase; an ergodic phase; and an intermediate phase that exhibits volume-law entanglement scaling but violates eigenstate thermalization in a more subtle way by having a large eigenstate-to-eigenstate variance of the expectation value of local operators even in narrow energy windows. These regimes are separated by many-body mobility edges, i.e. critical energy densities separating localized from delocalized

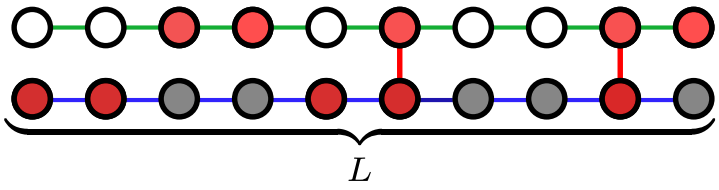

Figure 3.1: Schematic illustration of our setup. Here, the disorder potential only acts on the lower chain of the ladder ($\alpha = 0$), whereas the fermions in the upper chain are affected by the disorder only through the interactions. The fermions, indicated as red dots, hop along each chain, and interact only through a repulsive density-density interaction on each rung.

states in the many-body spectrum. The existence of such many-body mobility edges has been suggested based on both analytical [18, 17] and numerical [107, 127] observations; however, recent work has raised concerns about the stability of such a scenario [46].

A closely related question concerns the stability of many-body localization in open quantum systems, i.e. when coupled to bath degrees of freedom. Usually a bath is taken to be very large and the backaction of the system onto the bath is neglected. In this case (as well as in the presence of dissipation [122, 59]), one expects that the effects of many-body localization will be destroyed, although there is evidence for a crossover into a regime where some signatures of localization persist [145, 66, 96]. However, one can also consider the case where the number of degrees of freedom in the system and the bath is comparable and the backaction may be important. In this case, the interesting possibility arises that the backaction of the MBL system may be strong enough to induce localization in the bath [144]. The results of Ref. [123] may be interpreted as evidence for such a scenario.

In this chapter, we investigate these questions by numerically and analytically study-

ing a model for spinless fermions on a ladder, as sketched in Fig. 3.1. We introduce an uncorrelated disorder potential on one chain of the ladder, while keeping the other chain translationally invariant, and forbid hopping between the chains such that in the non-interacting limit, the chains are completely decoupled. We then introduce a local density-density interaction on each rung. With interactions, two sharply distinct scenarios appear: in one, the energy transport through the clean chain is sufficient to trigger delocalization of the entire system. In the other scenario, the localized fermions – through the density-density interaction – act as effective disorder potential for the fermions in the clean chain, inducing their localization. To distinguish these two scenarios, we will consider the entanglement entropy of highly excited eigenstates as well as the time evolution of the entanglement entropy. We find that in our model, both scenarios can be realized depending on the parameters of the system. We will comment on other possible intermediate scenarios at the end.

Our model is closely related to the model of Ref. [229], where the disorder potential is absent but the hopping strength in the two chains is vastly different and interactions between the chains are very strong. This model was studied in the context of dynamical effects akin to many-body localization in systems without explicit translational symmetry breaking in the Hamiltonian [178, 79, 47] (see also [70]), but where the initial conditions break translational symmetry. It was observed that the time evolution starting from random product state configurations exhibits slow dynamics at an intermediate time scale, yet relaxes at the longest time scales, consistent with with the formation of a

"quasi many-body localized" (qMBL) regime. Furthermore, the system shows a diverging susceptibility towards spin glass ordering upon introducing disorder. Our results are complementary in that we consider the case of strong disorder and weak interactions, and focus primarily on eigenstate rather than dynamical properties. We discuss the relationship between the models in more detail towards the end of Section 3.4.

It should also be noted that we focus purely on the one-dimensional case since in higher dimensions, localization of the entire system is very unlikely to occur. In particular, in three dimensions, there is no possibility of an interesting backaction of the localized states on the extended ones at weak interactions since perturbative disorder is irrelevant, i.e. the localization length is infinite up to finite value of V. In two dimensions, disorder is only marginally relevant, and actually tends to be driven irrelevant in the presence of interactions [120].

The remainder of this chapter is structured as follows: In Sec. 3.2, we describe the model, our diagnostics and the numerical approach in more detail. In Sec. 3.3, we discuss a perturbative analysis of the interchain coupling. In Sec. 3.4, we describe our numerical results, and conclude in Sec. 3.5.

3.2 Model and numerical approach

The Hamiltonian for the system is (see Fig. 3.1)

$$\hat{H} = -\sum_{\alpha} t_{\alpha} \sum_{i=1}^{L} \left(\hat{c}^{\dagger}_{\alpha,i} \hat{c}_{\alpha,i+1} + \text{h.c.} \right) + \sum_{i=1}^{L} w_i \hat{n}_{d,i} + V \sum_{i=1}^{L} \hat{n}_{d,i} \hat{n}_{c,i}. \tag{3.1}$$

Here, $c^{\dagger}_{\alpha,i}$ creates a fermion on the upper, clean ($\alpha = c$) or lower, disordered ($\alpha = d$) layer. The local potential w_i, acting only on the $\alpha = d$ fermions in the lower layer, is drawn uniformly from the range $[-W, W]$. V is a density-density interaction between the two chains. Each chain has length L such that the total number of sites in $2L$. Note that the particle number on each chain is separately conserved, reducing the size of the many-body Hilbert space. For even L, we choose each chain to be half-filled.

While the model is phrased here in terms of a ladder, it is equivalent to a system of two different flavors of fermions where only one flavor experiences the disorder potential. Such a description may be applicable to experiments on cold atoms which use different types of atom (non-convertible fermions), or different states of the same atom. We also note that since hopping between the chains is forbidden, the model can be mapped to a local model of hard-core bosons or spins by means of a Jordan-Wigner transformation. Since it is also possible to apply the Jordan-Wigner transformation to only one chain of the ladder, the model is related to spin and charge degrees of freedom in a Hubbard chain.

In Eq. (3.1), we have not included interactions between fermions on the same chain. We have confirmed numerically that adding a repulsive nearest-neighbor interaction between fermions on the order of the interlayer coupling or weaker on the same chain does not qualitatively affect the results. We have also verified that making the strength of the inter-chain interaction random does not affect the results.

We solve for highly excited eigenstates of Eq. (3.1) in the middle of the many-body

spectrum using the shift-and-invert method (discussed previously in the Introduction), which solves for low-lying states of

$$\hat{A}_{-1} = \left(\hat{H} - \lambda \mathbb{I}\right)^{-1} \tag{3.2}$$

where λ is a target energy. This approach was first used in the context of many-body localization in Ref. [127]. We use the implementation of SLEPc [78] & PETSc [13, 14, 6, 7], and rely on its direct LU solver and MUMPS. The LU factorization is used as a direct solver to perform the inversion after shifting. Once the inverse has been computed, the Lanczos method [115] can be used to target low-lying states of shift-and-inverted matrix. These states are the ones closest in energy to the target λ. We average over 250 eigenstates for 500 disorder realizations each for system sizes $L = 6$ and $L = 8$. For $L = 10$, we only compute eigenstates for 50 disorder realizations. Finally, for a few data points we simulated up to $L = 12$, where we obtained 150 states each for 100 disorder realizations. We choose the target energy $\lambda = VL/4$, which is close to the center of the many-body spectrum. For small systems, we have verified through a full diagonalization of $\hat{H}$ that the states thus obtained are representative of the "infinite-temperature" ensemble.

3.2.1 Eigenstate entanglement

The eigenstate thermalization hypothesis [49, 191, 166] suggests that in an eigenstate of a generic quantum system H at a finite energy density ϵ above the ground state, the reduced density matrix $\rho_{\mathcal{A}}$ for some region $\mathcal{A}$ will be close to a Gibbs state of the same Hamiltonian at some inverse temperature $\beta(\epsilon)$, $\rho_{\mathcal{A}} \approx \exp(-\beta H_{\mathcal{A}})$ [64]. Among many

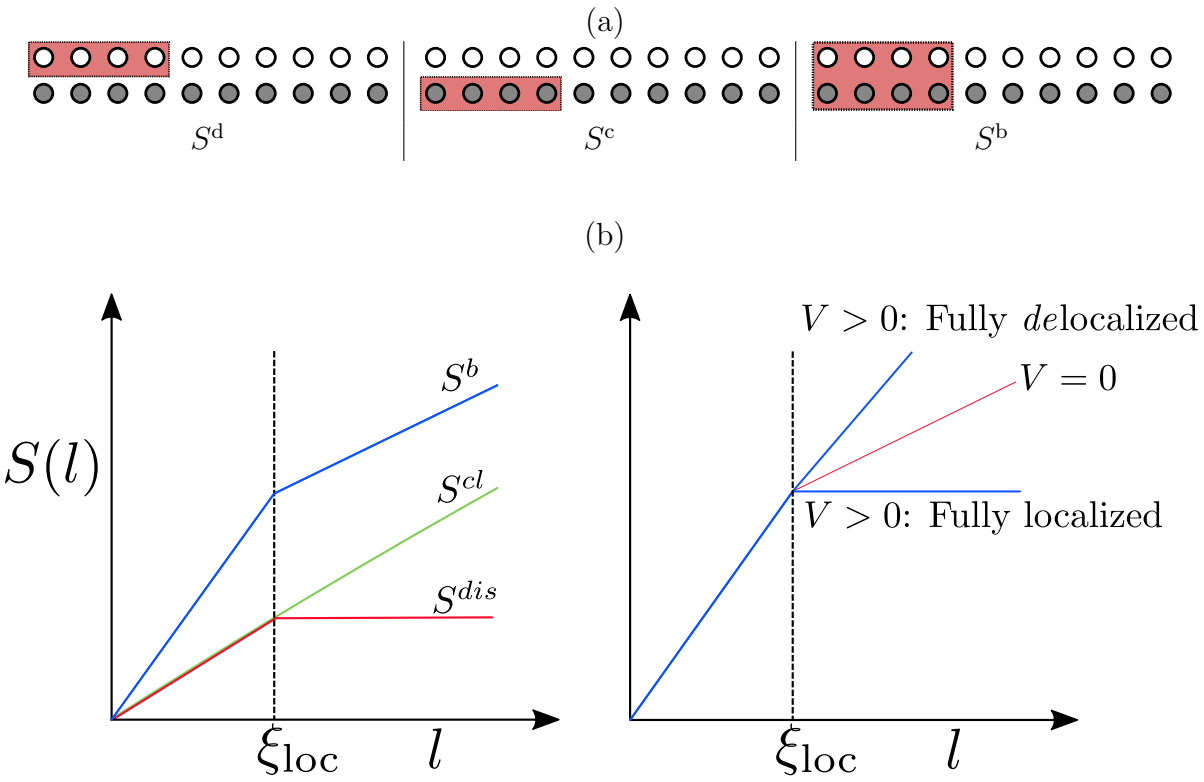

Figure 3.2: (a) Different entanglement cuts considered in this chapter. Here, the empty circles denote sites in the disordered chain, while filled circles denote sites in the clean chain. From left to right, we denote these entropy cuts as S^{d}, S^{c}, S^{b}. (b) Schematic behavior of the entanglement entropy. Left panel: decoupled case ($V = 0$), where $S^{\mathrm{b}} = S^{\mathrm{d}} + S^{\mathrm{c}}$. Right panel: Interacting case ($V \neq 0$).

other things, this implies that the entropy $S(\rho_{\mathcal{A}}) = -\operatorname{Tr} \rho_{\mathcal{A}} \log \rho_{\mathcal{A}}$ will exhibit a volume law, $S(\rho_{\mathcal{A}}) = s_{\mathrm{th}}(\epsilon)\mathrm{vol}(\mathcal{A})$. In the center of the many-body energy band, where $\beta \to 0$, one expects that the entropy density is close to its maximal value as given by the density of degrees of freedom.

One of the defining features of many-body localization is that this volume-law scaling is robustly violated [19]. Indeed, the excited eigenstates of an MBL system exhibit an area law [53]: the bipartite entanglement entropy between some region $\mathcal{A}$ and the rest of the system is found to scale only with the area of the boundary separating the regions. In

d dimensions, this leads to the scaling $S \sim L^{d-1}$, as opposed to the volume law $S \sim L^d$ that is expected for generic systems that obey eigenstate thermalization. Eigenstate entanglement has subsequently been used as powerful criterion to identify many-body localized phases [19, 107, 127].

We use eigenstate entanglement as diagnostic of whether the system described by Eq. (3.1) delocalizes or localizes. On a coarse level, distinguishing between a volume law and an area law allows us to determine whether the system is localized or not. Beyond this, if we find that the system exhibits a volume law, we can consider the entropy density to determine whether all microscopic degrees of freedom participate or whether some degrees of freedom remain localized.

Specifically, we consider the entanglement cuts illustrated in the top panels of Fig. 3.2. The cuts correspond to a contiguous block of sites in the clean (disordered) chain, which we label as S^{c} (S^{d}), as well as a cut that contains both chains, labeled as S^{b}. In the generic case where the two chains are coupled, an area law will only appear in S^{b}, since for the other cuts the area of the boundary scales with the volume of the block. However, in the non-interacting case $V = 0$ where the two chains are completely decoupled, the entropy of each of the chains separately can provide valuable insights.

The bottom panels of Fig. 3.2 schematically illustrate the behavior of the various entropy cuts. The lower left panel shows the case of decoupled, non-interacting chains ($V = 0$): the delocalized fermions in the clean layer contribute a volume law, $S^{\mathrm{c}} = s_{\mathrm{th}} L$ where $s_{\mathrm{th}} \approx \log 2$ is the thermal entropy density of a single layer at infinite temperature.

The localized layer, on the other hand, exhibits a volume law only for blocks smaller than the localization length $\xi_{\rm loc}$ [69] and saturates to a constant beyond that. The total entropy, $S^{\rm b} = S^{\rm d} + S^{\rm c}$, thus shows a volume law with prefactor $2s_{\rm th}$ for $l < \xi_{\rm loc}$, and crosses over to a volume law with a reduced prefactor $s_{\rm th}$ for $l > \xi_{\rm loc}$.

In the interacting case, the two scenarios discussed above are localization and delocalization of the entire system. These are illustrated in the lower right panel of Fig. 3.2: If the system becomes fully localized on some scale ξ', the entanglement entropy for the joint system $S^{\rm b}$ will exhibit an area law for $l > \xi'$ (note that while the figure shows the case $\xi' = \xi_{\rm loc}$, this need not necessarily be the case). If, on the other hand, the system fully delocalizes, the entropy will show a volume law with prefactor $2s_{\rm th}$ for all scales. Thus, in either scenario a strong signature appears in the eigenstate entanglement: the entropy either becomes constant, or the coefficient of the volume law doubles.

3.3 Perturbative analysis of interchain coupling

We expect that the eventual fate of the localization or thermalization of the ladder rests on the outcome of a competition between the tendency for the disordered chain to localize the states on the clean chain and the ability of the states in the clean chain to act as a thermalizing bath for the disordered chain. Before turning to direct numerical simulations, we consider the limit of weak interactions, $V \ll t_d, t_c$, where we can work perturbatively in V near the decoupled chain limit to estimate which of these effects is more important.

For $V = 0$, the clean chain has no randomness and exhibits extended single-particle eigenstates. With $V \neq 0$, however, if the disordered chain remains localized, the random distribution of charges $\langle \bar{n}_{d,i} \rangle$ in a given eigenstate produces an effective disorder potential $\mu_i \approx V \langle n_{d,i} \rangle$ in the clean chain. Due to the one-dimensional nature of the system, even an infinitesimally weak random potential will produce localization. In the case of weak interactions and thus weak disorder, localization occurs via quantum interference, and we can perturbatively estimate (using Fermi's golden rule) the localization length in the clean chain to be $\xi_V \approx t_c^2/(V^2\, \delta n_d^2)$, where $\delta n_d^2 \approx \rho_d(1-\rho_d)$ and ρ_d is the mean density of particles in the disordered chain.

As a technical aside, this treatment amounts to a Hartree-type approximation of the inter-chain interaction to obtain an effective disorder potential $\mu_i = V \langle n_{d,i} \rangle$ for the clean chain. Note that Fock-type exchange self-energies are zero in this model where particle number in each chain is separately conserved. Next, we will perturbatively incorporate interactions using the Hartree-dressed Green functions.

In the absence of this tendency towards localization, energy can propagate along the disordered chain mediated by resonant interactions with states in the clean chain. We can perturbatively estimate whether such resonant interactions can persist in spite of the tendency towards developing a finite localization length ξ_V in the clean chain. The typical level spacing for particle-hole excitations in the clean chain is:

$$\delta^{(2)} \approx \frac{1}{\Lambda_c \left(\nu_c \xi_V\right)^2} \approx \frac{V^4}{t_c^3} \tag{3.3}$$

where $\nu_c \approx 1/t_c$ and $\Lambda_c \approx t_c$ are the single-particle density of states and bandwidth, respectively. For strong disorder ($W \gg t_d$), the single-particle states of the disordered chain are well-localized with characteristic localization length $\xi_d \approx [\log(W/t_d)]^{-1}$. In this case, the simplest interchain interaction process is for a particle-hole excitation of two overlapping localized orbitals in the disordered chain to excite a particle-hole pair in two orbitals of the clean chain that reside within distance ξ_V of those in the clean chain.

For concreteness let us label a fixed pair of orbitals in the disordered chain by a, b, whose wave functions have the schematic form $\phi_{a,b} \approx \frac{1}{\sqrt{\xi_d}} e^{-|x-x_{a,b}|/2\xi_d}$, and similarly denote two orbitals in the other chain by α and β respectively with wave functions $\phi_{\alpha,\beta} \approx \frac{1}{\sqrt{\xi_V}} e^{-|x-x_{\alpha,\beta}|/2\xi_V}$. Then, for $|x_a - x_b| < \xi_d$, and $|x_{\alpha,\beta} - x_a| < \xi_V$ the matrix element for the interchain interaction among these orbitals is roughly:

$$\Gamma_{(a,b);\alpha,\beta} \approx V \int dx\ \phi^*_\alpha(x)\phi_\beta(x)\phi^*_a(x)\phi_b(x) \tag{3.4}$$

$$\approx \frac{V}{\xi_V} \approx \frac{V^3}{t_c^2} \tag{3.5}$$

Fixing our attention on a specific pair of orbitals in the disordered chain, the number of such transitions that are resonantly connected by matrix element Γ is of order $N_{\rm res} \approx \frac{\Gamma}{\delta} \approx \frac{t_c}{V}$, which is large for weak interactions, and in fact diverges in the limit of $V \to 0$. This divergence strongly suggests that, for weak interactions, the tendency for randomness in the disordered chain to localize states in the clean chain is insufficient to prevent it from acting as a bath for the disordered chain. The full system thus thermalizes in this limit on a timescale set by the magnitude of the matrix element Γ.

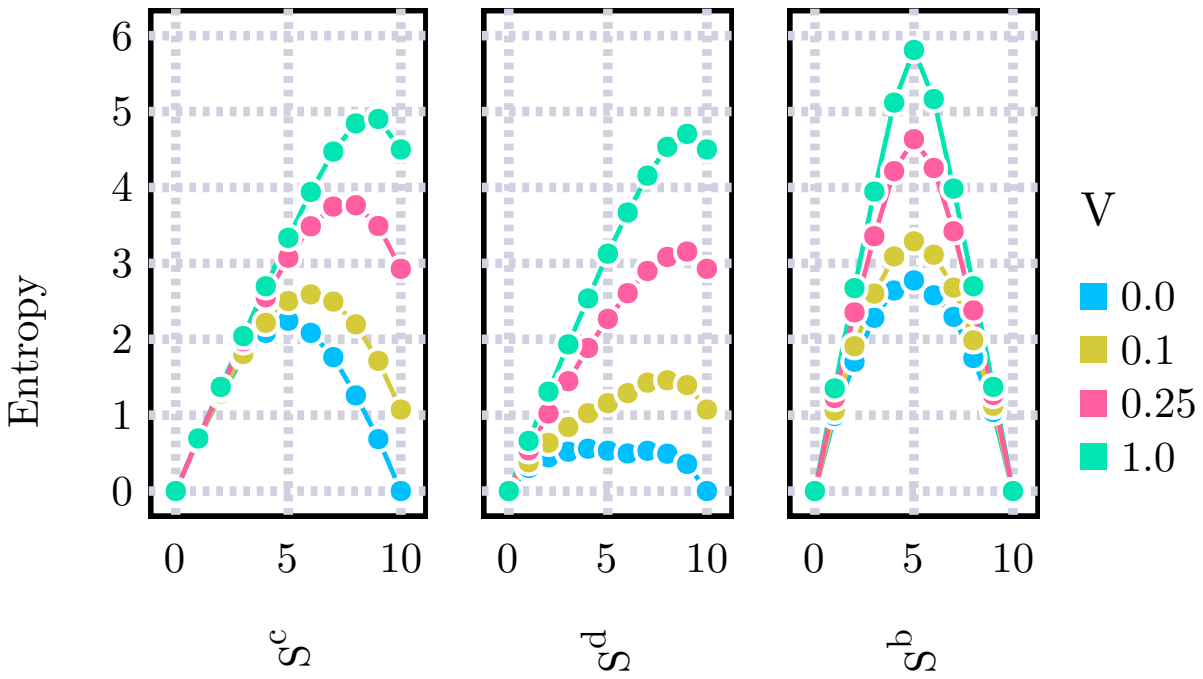

Figure 3.3: Entropy for three different cuts for a ladder of length $L = 10$ with $t_0 = t_c = 1$ and $W = 4$. The different cuts are illustrated in the top panels of Fig. 3.2. Error bars are comparable to the marker size.

To address the fate of thermalization in this ladder beyond these perturbative considerations, we now turn to microscopically exact numerical simulations.

3.4 Numerical results

3.4.1 Equipotent hopping

We first consider the case of equal hopping strength in the clean and disordered layer, $t_d = t_c = 1$. In Fig. 3.3, we show the behavior of different entropy cuts in this case for

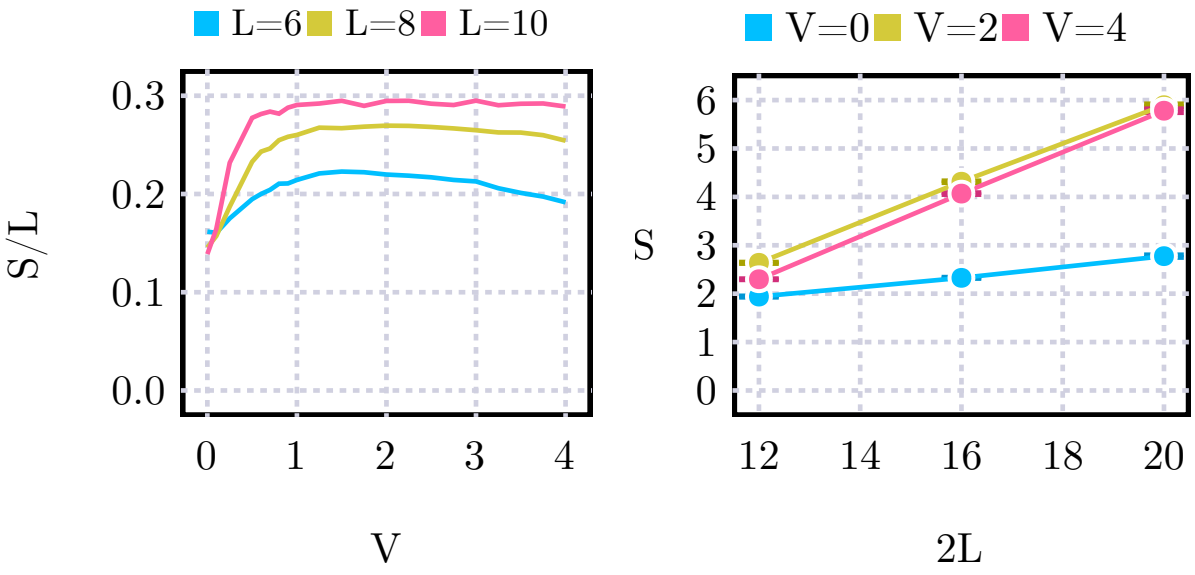

Figure 3.4: Left panel: Entropy S^{b} at the center of the system as a function of interlayer coupling V, for different system sizes and disorder strength $W = 4$. We observe that the increase of the entropy due to adding weak interactions sharpens as the system size increases. Right panel: Entropy $S^{\mathrm{b}}(L/2)$ for different V as a function of system size. The slope corresponds to the entropy density, which is observed to increase drastically as interactions are increased, compatible with all degrees of freedom contributing to the entropy.

a system with a total of $2L = 20$ sites and disorder strength $W = 4$. We first explore the results in the non-interacting case, $V = 0$. Here, we observe a volume law for S^{c} (left-most panel), while the disordered system exhibits a saturation of the entanglement entropy S^{d} for $l \gtrsim 3$ (center panel). Note that for $V = 0$, $S^{\mathrm{d}}(l) = S^{\mathrm{d}}(L - l)$ (and similarly for S^{c}), which is not true for $V \neq 0$. By identifying the saturation point of the entropy for S^{d}, we can read off that the localization length for $W = 4$ is $\xi_{\mathrm{loc}} \approx 3$. The right-most panel shows the joint entropy S^{b}, which for $V = 0$ is simply the sum of the two contributions and is therefore dominated by the volume law in the clean chain.

As we turn on interactions between the two layers ($V > 0$), we observe that the entanglement entropy for each cut increases dramatically. For the entropy cuts isolating each chain, this is expected as the boundary between the two chains begins to contribute to the entanglement entropy. However, we note that in the limit of strong enough interactions, the entropies S^{d} and S^{c} become approximately equal, indicating that there is no distinction between the two chains. Considering the joint entropy, we find that the entropy at the center of the system approximately doubles from $S^{\mathrm{b}}(L/2) \approx 2.8$ to $S^{\mathrm{b}}(L/2) \approx 5.8$. This is consistent with a volume law contribution from both chains. The maximum measured value at the center of the system is close to the upper bound $S^{\mathrm{b}}(L/2) \approx 6.9$; the discrepancy can be attributed to finite-size corrections. These results are strongly suggestive of delocalization of the entire system for $V > 0$.

To further investigate this, we consider the cut at the center of the system, $S^{\mathrm{b}}(L/2)$, for various system sizes and interaction strengths as shown in Fig. 3.4. In the left panel,

we have rescaled the entropy by the system size to convert to an entropy density. We observe that the entanglement increases rapidly as interactions are turned on for each system size. The increase sharpens as the system size is increased, indicating that at least in this parameter regime the entire system delocalizes for infinitesimal interaction strength V in the thermodynamic limit. For small system sizes, the entropy decreases for very large interactions, but this effect does not appear to persist to larger system sizes. In the right panel, we analyze the finite-size dependence of the entropy at the center of the system, which clearly exhibits a volume-law scaling. The coefficient of the volume law increases rapidly as interactions are turned on.

3.4.2 Narrow-bandwidth bath

While the results of the previous section confirm that the system tends to delocalize, as suggested by the considerations in Sec. 3.3, it may still be possible to change the parameters of the system in such a way as to enhance the tendency towards localization. We focus here on the effect of tuning the hopping strength in the clean layer, t_c. By reducing this hopping strength, we can reduce the bandwidth of the delocalized degrees of freedom, which reduces the amount of energy the bath can absorb. This regime was previously studied in Ref. [66]. Clearly, in a limit where $t_c \ll \delta E$, where δE is the mean level spacing of many-body energy levels, the system will not delocalize; however, this requires an exponentially small bandwidth $t_c \sim 2^{-L}$. In a more physical regime, where $\delta E \ll t_c \ll t_d$ and $t_c \ll W$, one may still expect that the bath is inefficient at delocalizing

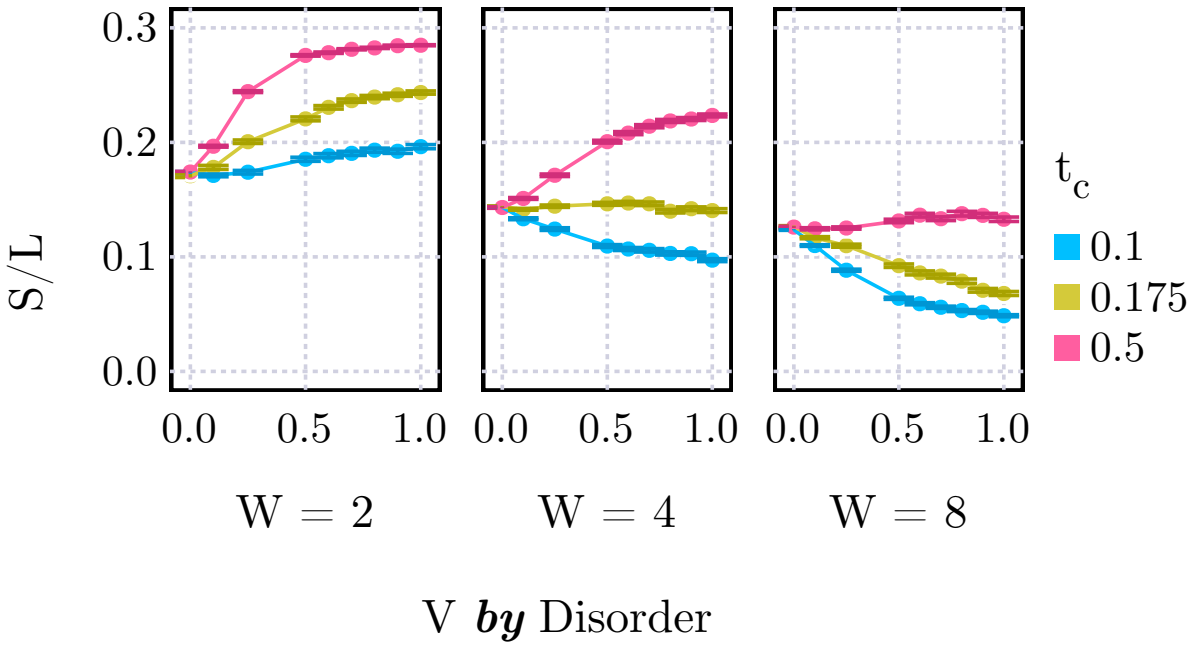

Figure 3.5: Entropy $S^{\mathrm{b}}(L/2)$ for a center cut of the system for various disorder strengths W and hopping in the clean chain, t_c. As disorder is increased and the hopping t_c reduced, we observe a crossover from a regime where interactions tend to increase entropy to a regime where interactions decrease entropy, i.e. drive the system towards localization.

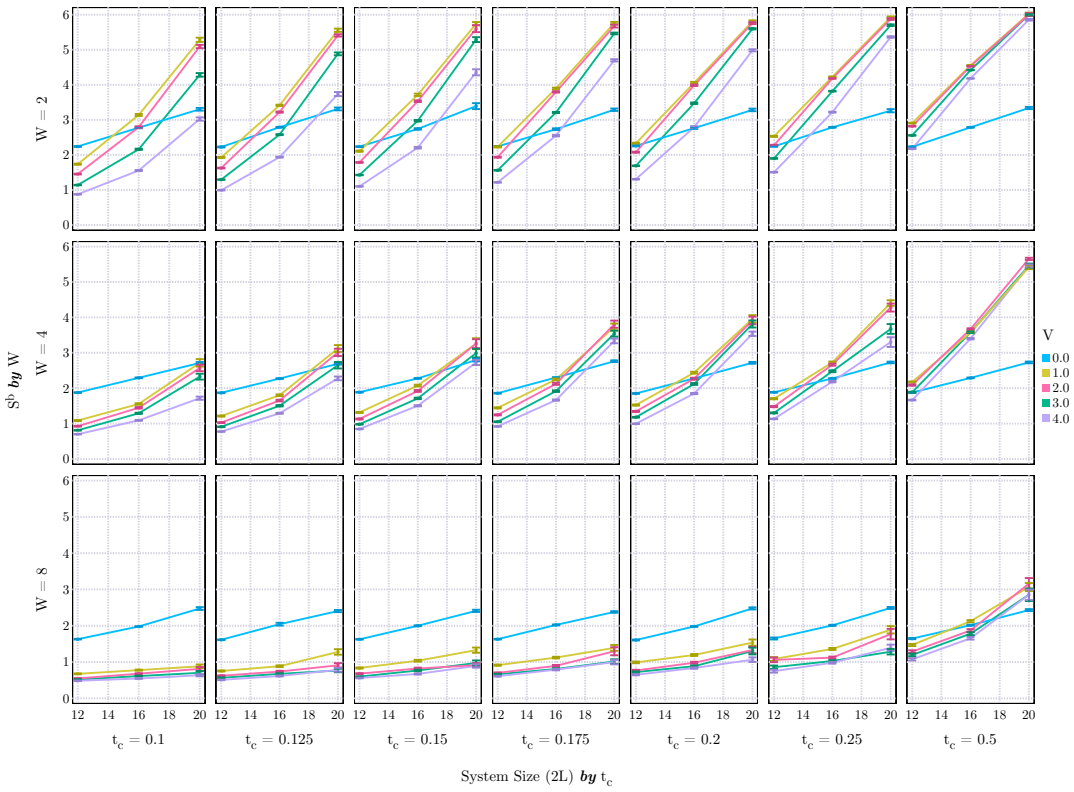

Figure 3.6: Maximum entropy S^{b} for various L and interlayer couplings V, allowing the hopping strength to vary. For very large interlayer coupling, the system appears to localize at small hopping in the clean chain.

the system because its bandwidth is small compared to the energy mismatch of nearby fermion states in the disordered system, which is of order W; however, higher-order resonances may invalidate this simple picture.

Our numerical results are summarized in Figs. 3.5 and 3.6. In Fig. 3.5, we show the entropy at the center of the system as a function of interaction strength V for three different strength of the disorder and several values of the hopping in the clean chain t_c, while keeping $t_d = 1$. For slightly reduced values of t_c, such as $t_c = 0.5$, we find behavior that is very similar to the case $t_c = t_d = 1$. However, for strongly reduced hopping of $t_c = 0.1$ and sufficiently strong disorder, the entropy does not increase rapidly – as was seen in the left panel of Fig. 3.4 – but rather remains constant, or even decreases in the case of strong disorder $W = 8$. This implies that as interactions are turned on, the system tends towards localization rather than delocalization.

To explore whether this is a robust effect that persists to the thermodynamic limit, we examine how this behavior depends on the system size over the limited range available to our exact numerics. In Fig. 3.6, we show the entropy at the center of the system versus system sizes, for an array of hopping strengths $t_c \in [0.1, 0.5]$ (keeping $t_d = 1$) and disorder strengths $W = 2, 4, 8$. For weak disorder ($W = 2$, top row), we observe that interactions suppress the entropy for small systems and $t_c \leq 0.25$, but for sufficiently large systems the behavior changes and the entropy of the interacting system exceeds that of the decoupled chains and the coefficient of the volume becomes comparable to that in the case $t_c = t_d$. The scale at which this crossover takes place depends on the

choice of W and t_c, and appears to shift to larger and larger systems as W is increased and t_c reduced. For example, for $W = 4$ and $t_c = 0.1$ (leftmost panel of the middle row) the crossover scale appears to be slightly larger than the system sizes available to us. We note that such an upturn of the entropy seems at odds with the results put forward in Ref. [69], which argued that $\partial^2 S(\ell)/\partial \ell^2 \leq 0$, where $S(\ell)$ is the entropy of a contiguous block of ℓ sites in a system of total size L. However, this result only holds for $\ell \ll L$, whereas here we have the case $\ell = L/2$ and therefore no clear separation between the two scales ℓ and L.

Finally, to examine the case of strong disorder ($W = 8$), small bath bandwidth ($t_c < 0.2$) and strong interactions further, we have performed simulations for up to $L = 12$ (i.e. 24 sites); our results are shown in Fig. 3.7. Although the entropy increases slightly with system size, it remains strongly suppressed over the entire range of system sizes available to our simulations. Nevertheless, given the finite-size crossover behavior observed away from this limit, we cannot rule out delocalization of the system on a very long length scale.

3.4.3 Time evolution

To obtain further insights into the putative localized regime at strong disorder and weak bath hopping and to connect our results to those of Ref. [229], we repeat some of the numerical experiments performed there in the presence of weak disorder. To this end, we prepare the system in a randomly chosen product state, evolve under the Hamil-

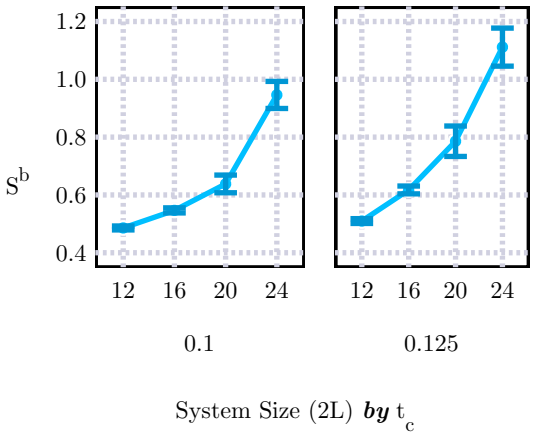

Figure 3.7: Maximum entropy S^b for system sizes up to $L = 24$. Here, $V = 4$ and $W = 8$. Note the drastically different scale on the vertical axis compared to Fig. 3.6.

tonian (3.1) (where, following [229], we from here forward impose periodic boundary conditions), and compute the entropy S^{b} at the center of the system as a function of time T. We average the results over different initial states, and in the case of $W > 0$ also over 10 different disorder realizations. For each case, we smooth the data by taking the maximum over 6 adjacent time samples. We note that these results are obtained for much stronger interaction V and much smaller t_c than the results reported in the previous sections.

Our results are shown in Fig. 3.8. Here, the parameters for the upper panel match those of Ref. [229], in particular $t_c = 0.001$, $t_d = 1$, and the disorder-free case $W = 0$ exactly matches the data presented there. Upon adding even a very weak disorder potential, the evolution of the entropy for large time scales – beyond the equilibration of local degrees of freedom on a scale $1/t_d$ – changes drastically: the slow divergence of the entropy at very large times that is observed in the quasi-MBL phase, and associated

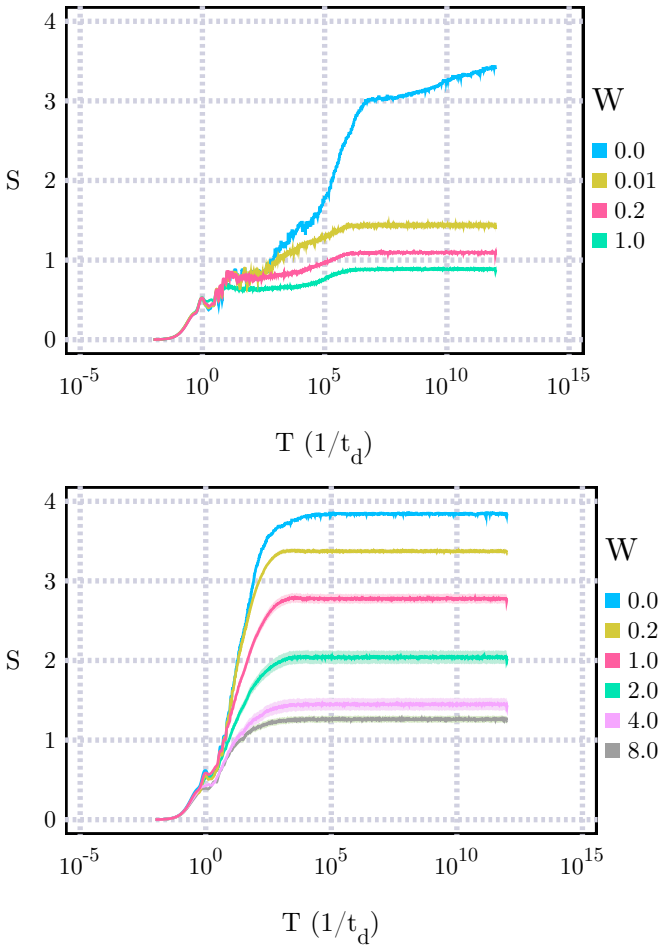

Figure 3.8: Time evolution of the entanglement entropy $S^{\mathrm{b}}(L/2)$ for $V = 10$ and $2L = 16$ total sites. The top panel shows data for $t_c = 0.001$, corresponding to Fig. 2 of Ref. [229], while the bottom panel shows $t_c = 0.1$ for comparison to Fig. 3.6.

with a slow relaxation of the system at all length scales, appears completely suppressed in the case of a weakly disordered system. Furthermore, the entropy saturates to a far sub-thermal value for both $L = 4$ (not shown) and $L = 8$ even for the weakest disorder potential $W = 0.01$. These results are consistent with the observation of a many-body localized regime in this limit in the entanglement entropy of highly excited eigenstates, and is also consistent with the observation of a divergent susceptibility to spin glass ordering in Ref. [229].

Increasing the hopping in the clean chain to $t_c = 0.1$ (bottom panel of Fig. 3.8), we find that a weak disorder potential suppresses the saturation entropy only slightly, while a sufficiently strong potential in the disordered chain is still able to suppress the entropy for both chains. While a finite critical disorder strength necessary to drive the system into the MBL phase appears at odds with a quasi-MBL regime in the clean limit, our numerical observation may also be due to a large localization length compared to the available system sizes. In either interpretation, these results are consistent with the observation of a possible MBL phase in a similar parameter regime in the entropy of eigenstates, see Fig. 3.6.

3.5 Conclusion

We have proposed a system of spinless fermions on a ladder, where one chain of the ladder is translationally invariant while the other experiences a disorder potential. This system can serve as a prototypical example to study many-body localization effects in

a system where in the limit of vanishing interactions, localized and delocalized degrees of freedom coexist. Equivalently, the system allows us to study the effect of coupling a small bath to a many-body localized system. Exploiting the large degree of tunability of the model, we have found that while in most of the phase diagram the system tends towards delocalization, a many-body localized regime – and thus localization of the bath through induced disorder from the MBL system – may appear in a regime where the bandwidth of the bath is small compared to the disorder strength.

In the entanglement of eigenstates, this localization of the entire system is heralded by a decreasing entanglement entropy as a function of the interaction strength. Attempting to extrapolate to larger systems, we find a broad regime of parameters where the trend of suppression of the entropy by interactions reverses for larger system sizes, and the system tends towards delocalization as the system size is increased. By taking the hopping in the clean chain very small and the disorder very strong, we obtain a regime where the entropy remains small for all system sizes accessible to our numerics; however, we cannot answer in the affirmative whether we obtain a genuine many-body localized phase of both chains, or rather a regime where the crossover to delocalization takes place at an extraordinarily large system scale. Turning to the time evolution of the entropy starting from random initial product states, a strong suppression of the saturation entropy is observed in a similar parameter regime, providing further support for a many-body localized phase.

Finally, we comment on the intermediate non-ergodic yet delocalized phase observed in Ref. [123] in a window of many-body energy densities between a localized regime at

low energies, and a fully ergodic delocalized regime at high energies. Since the crossover regime in the problem considered here is parametrically very large, reliably observing such a regime appears very challenging and has not been attempted systematically. However, we point out that tuning into such a regime as a function of energy is less natural in the model considered here, since in the single-particle limit localized and delocalized states coexist at all energies, whereas in the model of Ref. [123] the energy density can be understood as tuning the relative number of localized and delocalized orbitals in the non-interacting limit. A more natural parameter to replicate the phase diagram in our model would thus be the relative filling of the clean and disordered chains. However, given the small range of system sizes available to us, changing the average inter-particle distance is likely to incur larger finite-size corrections.

3.6 Acknowledgements

We thank Chris Laumann, Sankar Das Sarma, Sarang Gopalakrishnan and Sid Parameswaran for insightful discussions. This research was supported in part by the National Science Foundation, under Grant No. DMR-14-04230 (James R. Garrison), and by the Caltech Institute of Quantum Information and Matter, an NSF Physics Frontiers Center with support of the Gordon and Betty Moore Foundation (James R. Garrison).

This material is based upon work supported by the National Science Foundation Graduate Research Fellowship under Grant No. DGE 1144085. Any opinion, findings, and conclusions or recommendations expressed in this material are those of the authors(s)

and do not necessarily reflect the views of the National Science Foundation.

We acknowledge support from the Center for Scientific Computing at the CNSI and MRL: an NSF MRSEC (DMR-1121053) and NSF CNS-0960316. Andrew C. Potter was supported by the Gordon and Betty Moore Foundation's EPiQS Initiative through Grant GBMF4307.

Chapter 4

Extracting entanglement geometry from quantum states

4.1 Introduction

Tensor networks have proven to be a powerful and universal tool to describe quantum states. Originating as variational ansatz states for low-dimensional quantum systems, they have become a common language between condensed matter and quantum information theory. More recently, the realization that some key properties of holographic dualities [200, 197, 129, 223, 3] are reproduced in certain classes of tensor network states (TNS) [198, 56] has led to new connections to quantum gravity. In particular, many questions about holographic dualities appear more tractable in TN models [164, 21, 141, 155, 15, 137, 45, 77, 228, 102, 163]. The study of the geometry of

TN states underlies these developments. Here, the physical legs of the network represent the boundary of some emergent "holographic" space that is occupied by the TN. While in networks such as matrix-product states (MPS) [57, 221, 151] and projected entangled-pair states (PEPS) [65, 148, 210] this space just reflects the physical geometry, other networks – such as the multi-scale entanglement renormalization ansatz (MERA) [213, 214] – can have non-trivial geometry in this space [56]. We will refer to this geometry as "entanglement geometry".

In this chapter, we investigate whether this entanglement geometry can be extracted from a given quantum state without pre-imposing a particular structure on the TN [33]. We first describe a greedy, iterative algorithm that, given a quantum state, finds a 2-local unitary circuit that transforms this state into an unentangled (product) state (see Fig. 4.1). Such circuits, composed from unitary operators acting on two sites (which are not necessarily spatially close to each other), can be viewed as a particular class of TNS where the tensors are the unitary operators that form the circuit.

We then develop a framework for analyzing the geometry of these circuits. First, we introduce a locally computable notion of distance between two points in the circuit, thus inducing a geometry in the bulk. We then focus on a particular property of this geometry, the length of geodesics (shortest paths through the circuit) between physical (boundary) sites. A similar quantity has been previously discussed as a diagnostic of geometry in tensor networks [56], and reveals similar information as the minimal spanning surface in the celebrated Ryu-Takayanagi (RT) formula for the entanglement entropy in

AdS/CFT [171, 170]. Crucially, our definition takes into account the strength of each local tensor, and thus allows us to numerically compute an appropriate length without imposing additional restrictions on the tensors [155] or *a priori* knowledge of the emergent geometry.

Applying these techniques to many-particle quantum states, we observe three regimes: (i) a flat (zero curvature) two-dimensional geometry, (ii) a hyperbolic two-dimensional geometry, and (iii) a geometry where the geodesic distance between all points is equal, which corresponds to zero (fractal) dimension. We first observe these in eigenstates of non-interacting fermions in a disorder potential. For low-energy eigenstates with weak disorder, we find a hyperbolic geometry and thus recover key aspects of the AdS/CFT duality [200, 197, 129, 223, 3]. Going beyond eigenstates, we study a quench from the localized to the delocalized regime, i.e. the evolution of a localized initial state under a Hamiltonian with vanishing disorder potential. In this case, the geodesics reveal detailed information about the deformation of the emergent geometry, which progresses from flat geometry (i) to zero-dimensional (iii). This process reproduces certain aspects of previous holographic analyses of quantum quenches [87, 1, 190].

In a complementary approach 4.6, we also examine the nature of emergent light cones in the unitary network. In the case of critical systems, these are found to exhibit features of scale invariance. In the cases of localized and thermal states, the light cones reveal that the entanglement is fully encoded in local and global operators, respectively.

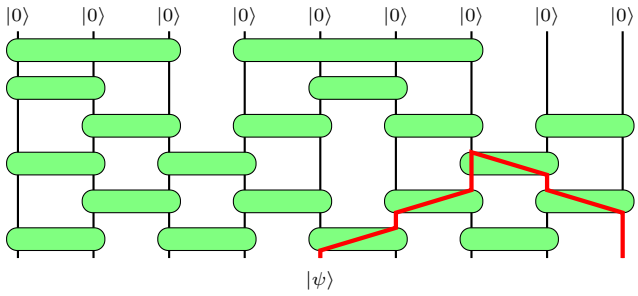

Figure 4.1: Example of a two-local unitary circuit, where each unitary acts only on the two qubits that are at its ends. The thick red line indicates a geodesic between the 5th and 9th qubit (from the left), following a path through the circuit as given by Fig. 4.2.

4.2 Disentangling algorithm

Our algorithm for finding a unitary disentangling circuit is in many ways inspired by the strong-disorder renormalization group [128, 61]. However, there are two crucial differences. First, instead of acting on the Hamiltonian, the algorithm acts on a particular state. Second, rather than on the energetically strongest bond, at each step the algorithm works on the most strongly entangled pair of sites. The algorithm has two desirable properties. First, it works for a broad class of input states, including states that have area law and volume law entanglement. This comes at the cost of generating circuits that cannot in general be contracted in polynomial time. Second, each iteration of the iterative algorithm is completely determined by the output of the previous iteration; we thus avoid solving the challenging non-linear optimization problems that are usually encountered when optimizing a tensor network. Similar algorithms have been put forward in Refs. [38, 102].

We take as input a quantum state $|\psi\rangle$ on a lattice $\mathcal{L}$. We denote as ρ_{ij} the reduced

density matrix on sites $i, j \in \mathcal{L}$, $\rho_{ij} = \mathrm{Tr}_{\mathcal{L}\setminus\{i,j\}} |\psi\rangle\langle\psi|$, and as ρ_i the reduced density matrix on site i, $\rho_i = \mathrm{Tr}_{\mathcal{L}\setminus\{i\}} |\psi\rangle\langle\psi|$, and $S(\rho) = -\operatorname{Tr} \rho \log \rho$. The algorithm proceeds as follows:

(i) Calculate the mutual information between all pairs of sites, $I(i:j) = I(\rho_{ij}) \equiv S(\rho_i) + S(\rho_j) - S(\rho_{ij})$, and find the pair (i, j) with the largest mutual information. If all $I(i:j)$ are below some predefined threshold ϵ, terminate. (ii) Find the unitary matrix $\hat{U}_{ij}$ that acts only on sites i and j and maximally reduces the amount of mutual information between these sites, i.e. solve $\min_{\hat{U}_{ij}} I(\hat{U}_{ij}\rho_{ij}\hat{U}_{ij}^\dagger)$. (iii) Set $|\psi\rangle \leftarrow \hat{U}_{ij}|\psi\rangle$, and return to step 1.

Details of the algorithm, in particular step (ii), can be found in Section 4.7. For an exact representation of a many-body state in a Hilbert space of dimension $\dim \mathcal{H}$, one iteration of the above algorithm can be carried out with computational cost $\mathcal{O}(L \dim \mathcal{H})$ [1]. For a system of non-interacting fermions, however, the algorithm can be completely expressed in terms of the correlation matrix $C_{ij} = \langle \hat{c}_i^\dagger \hat{c}_j \rangle$ [215, 156, 157]. Given the initial correlation matrix, the algorithm can be performed in $\mathcal{O}(L)$ operations per iteration, where L is the number of fermionic modes. In all cases, a single iteration of the algorithm can be performed as fast or faster than finding the eigenstates. The number of iterations required to converge to an unentangled state depends heavily on the input state: for weakly entangled states, convergence is fast, while for states with large entanglement, such as completely random quantum states, convergence can be very slow. Furthermore, the algorithm is not straightforwardly applicable to certain specific classes of states (see, e.g., the perfect tensors of Ref. [155]). We numerically explore convergence for some

[1] Note that while the first iteration is carried out in $\mathcal{O}(L^2 \dim \mathcal{H})$ time, all subsequent iterations can be carried out in $\mathcal{O}(L \dim \mathcal{H})$ time, as only quantities involving the transformed sites i and j must be recalculated.

relevant cases in Section 4.7.4.

The algorithm ultimately constructs a unitary circuit $\hat{U} = \hat{U}^{(\tau)}_{i_\tau j_\tau} \dots \hat{U}^{(2)}_{i_2 j_2} \hat{U}^{(1)}_{i_1 j_1}$ acting on the initial state $|\Psi\rangle$, where $\hat{U}^{(\tau)}_{i_\tau j_\tau}$ is the unitary obtained in the τ'th step. The number of execution steps corresponds to the number of unitaries comprising the circuit. The circuit is 2-local in the sense that each unitary acts on two sites, but it is *not* local in the lattice geometry because the two sites i and j may be arbitrarily far apart. Furthermore, this circuit is not unique: an ambiguity arises since the unitary can always be followed by a swap of the two sites or a single-site unitary while keeping the mutual information the same 4.7.

4.3 Emergent geometry of unitary circuits

A powerful way to probe the geometry of the unitary network is to measure the length of "geodesics", i.e. the shortest paths connecting two physical sites on the boundary of the circuit through the bulk of the circuit (see Fig. 4.1). The crucial ingredient for a numerical analysis of the unitary circuits is an appropriate notion of length for a path in the circuit which incorporates the strength of each unitary operator. It is obvious that a careful definition of this quantity is necessary: If, for example, one were simply to count the number of unitaries traversed in connecting two sites, one would – for a sufficiently deep circuit – always find a length of 1, since eventually all pairs of sites will be directly connected by a unitary. However, deep in the circuit the unitaries are very close to the identity, and therefore do not mediate correlations between the two sites. It

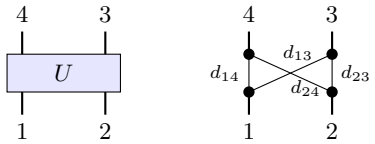

Figure 4.2: *Left panel:* Labeling of the input and output indices on a unitary operator. *Right panel:* Local graph corresponding to the unitary operator, with weights labeled on the internal edges.

is also desirable for the definition of length to be invariant under trivial deformations of the circuit, such as introducing additional swap, identity, or single-qubit gates. Finally, the distance measure should be computable locally and not rely on any global features of the graph.

Our definition of length builds on a local connection between geodesic length and correlations [164]. We construct a weighted, undirected graph as illustrated in Fig. 4.2: The vertices of the graph are the indices of the unitary operators. Edges connecting different operators have weight 0, while the internal edges connecting different indices of the unitary have lengths d_{ab} as labeled in the right-hand side of Fig. 4.2. To define d_{ab}, we interpret the unitary as a wavefunction on four qubits and set $d_{ab} = -\log[I(a : b)/(2\log 2)]$, where $I(a : b)$ is the mutual information between qubits a and b of the normalized wavefunction. Unitarity dictates $d_{12} = d_{34} = \infty$: these two lengths are not included in the graph. Entanglement monogamy [43, 203] implies that if $d_{24} = 0$ ($d_{14} = 0$), d_{13} (d_{23}) must also vanish and d_{14} (d_{24}) must be infinite. Given this weighted, undirected graph, the minimal distance between two vertices is computable using standard graph algorithms.

To develop some intuition for this quantity, consider the length of a path in well-

known TNS such as MPS/PEPS and MERA [56]. Assuming that each tensor in such a network has roughly equal strength, we can for now simply take the length to be the number of tensors that a path between two points traverses. For an MPS or PEPS, the length of the geodesic is then simply the physical distance between the sites, indicative of a flat entanglement geometry. In contrast, the length of a geodesic in a MERA scales only logarithmically with the physical distance, since the path is shorter when moving through the bulk of the TN [56]; this is a signature of a hyperbolic entanglement geometry.

It is important to contrast the geodesics considered here with the minimal surfaces in the RT formula for the holographic entanglement entropy. In the standard translation to TNS, such a minimal surface is given by the minimal number of bonds that need to be cut in order to completely separate two regions of physical sites. A minimal surface in this sense can be defined for any TN, and always yields an upper bound to the entanglement entropy between the two regions [2]. While in some cases these minimal surfaces also take the form of geodesics [155], they are distinct from the geodesics as defined in this manuscript, which *connect* pairs of sites rather than *separate* regions of sites. The difference is most easily seen in a MPS: while our geodesics are *linear* in the physical distance, the minimal separating surface is *constant*, since at most two bonds need to be cut to separate the TN. While our definition is more natural in the context of unitary circuits, they are complementary to each other, and both reveal similar information when appropriately interpreted.

It is important to recognize that while our distance measure locally is connected to

[2]This well-known fact is discussed explicitly e.g. in Refs. [211, 56, 44].

correlations, there is no simple one-to-one correspondence between the behavior of our geodesics and the behavior of two-point correlation functions. As outlined in Ref. [56], an intuitive relation is for correlations to decay exponentially with the geodesic length. This relation is precise for MPS, and also suggests the possibility of power-law decay of correlations in MERA (although for certain MERA the correlations may decay faster). However, the connection breaks down in the case of a PEPS: while the length of a geodesic is always at least the physical (Manhattan) distance, it is possible to find PEPS whose correlations decay as a power law [211]. Finally, the intricate behavior in a quantum quench discussed below is largely invisible to two-point correlations.

4.4 Models

We first study the properties of the disentangling circuits in a model of non-interacting spinless fermions in one dimension moving in a disorder potential. We discuss further examples in Section 4.6. The random-potential model is given by

$$\hat{H} = -t \sum_i \left(\hat{c}_i^\dagger \hat{c}_{i+1} + \hat{c}_{i+1}^\dagger \hat{c}_i \right) + \sum_i w_i \hat{c}_i^\dagger \hat{c}_i, \tag{4.1}$$

where $\hat{c}_i^\dagger$ creates a spinless fermion on the i'th site of a chain of length L. Throughout this chapter, we work with periodic boundary conditions, set $t = 1$ as an overall energy scale, and focus on Slater determinants at half filling. The random on-site potential is chosen from a uniform distribution of width W, $w_i \in [-W/2, W/2]$. For vanishing disorder $W \to 0$, this system is critical and the long-wavelength limit of the ground state is described by a free-boson conformal field theory with central charge $c = 1$. For any

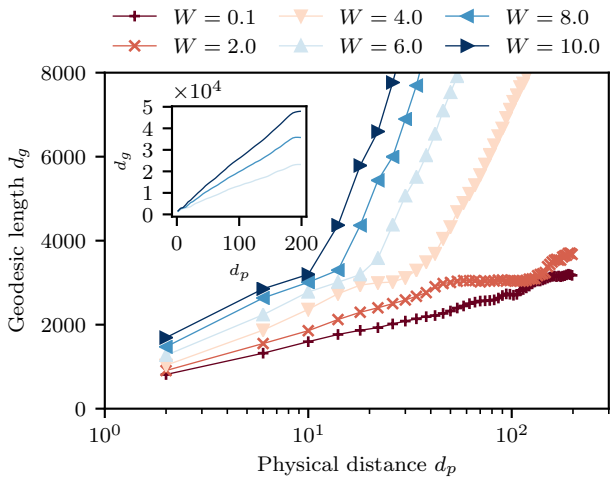

Figure 4.3: Geodesic length of the $L = 500$ Anderson disorder model for different values of the disorder strength W, with 200 realizations each. While the physical distance is given in lattice spacings, the geodesic length is in arbitrary units. The inset shows the same data for $W = 6.0, 8.0, 10.0$ on a linear scale to highlight the linear dependence $d_g \sim d_p$.

finite strength of the disorder potential, the fermions localize [10]. However, for very small $W \ll 1$, the localization length ξ_{loc} is large compared to the system sizes we study, allowing us to break translational invariance without significantly affecting physically observable properties.

4.5 Numerical Results

Our numerical findings for the scaling with the physical distance of geodesics in ground states of (4.1) are shown in Fig. 4.3 for different disorder strengths. Consider first the case of very large disorder strength, and thus short localization length. The geodesic length initially grows as $d_g \sim \log d_p$ with the physical distance d_p (see in particular the inset of Fig. 4.3), and then crosses over to a linear dependence $d_g \sim d_p$, indicated by

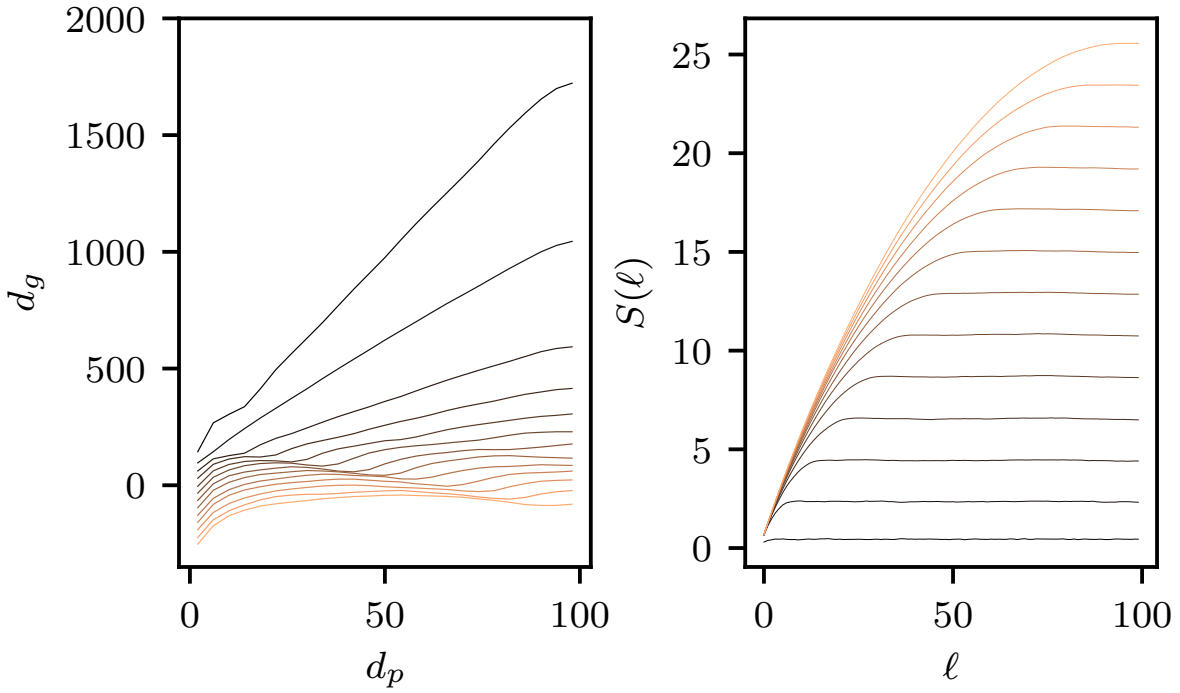

Figure 4.4: Quench from the ground state of the Anderson disorder model with with $L = 200$ sites and $W = 8$ to the clean case $W = 0$. *Left panel:* Geodesic length d_g as a function of physical distance d_p. *Right panel:* entanglement entropy of a contiguous region of ℓ sites. Individual lines represent snapshots of the system at times equally spaced between $T = 0$ to $T = 25.25$ averaged over 200 disorder realizations. The curves in the left panel have been offset by $-15 \cdot T$. Increasing copper/decreasing blackness indicates times further in the quench.

the sharp kink in Fig. 4.3. This behavior at large physical distance is characteristic of the flat entanglement geometry expected in a localized state. As the disorder strength decreases, the crossover shifts to larger and larger distances, indicating that the crossover length corresponds to the localization length. For very weak disorder potential (such as $W = 0.1$, where the localization length exceeds the system size), the region of logarithmic dependence spans the entire system. This is the hallmark feature of hyperbolic entanglement geometry and establishes a connection to other holographic mappings, such as the AdS/CFT correspondence.

Going beyond eigenstates, we now consider a quench where the system is initialized in the ground state of (4.1) with finite disorder ($W = 8$ in the examples chosen here), and is subsequently evolved under the translationally-invariant Hamiltonian ($W = 0$). This is similar to quenching the mass gap from a finite value to zero. We evolve up to time $T = 100$, performing the disentangling algorithm to obtain $d_g(d_p)$ at various times during the quench. Our results are shown in the left panel of Fig. 4.4, while the right panel shows the growth of bipartite entropy of a block of ℓ sites, and thus the crossover from area-law to volume-law entanglement entropy scaling. Note that here, in contrast to Fig. 4.3, the horizontal axis scales linearly.

Initially, the system exhibits the expected $d_g \sim d_p$ scaling of a localized system. The dominant effect at early times is a fast reduction in the scaling coefficient. However, careful examination at early times already reveals a drastic change in the scaling behavior at short distances, where d_g, instead of growing linearly with d_p, becomes nearly constant (or even decreases slightly). There is a sharp kink associated with the crossover from this to the linear behavior, which moves out to larger and larger distances with time, and finally reaches the maximal distance $d_p = L/2$. Comparison with the right panel of Fig. 4.4 shows that the location of the kink corresponds to the crossover from area-law to volume-law scaling of the bipartite entanglement entropy. Once the system has reached a long-time state with volume-law entanglement entropy, d_g shows some d_p-dependence only for short distances, and is flat otherwise.

In terms of the emergent entanglement geometry, the interpretation of these findings is

as follows: the global quench excites a homogeneous and finite density of local excitations, which ballistically spread and entangle with each other. Both the kink and the area- to volume-law crossover follow the spread of this wavefront. For distances beyond this (time-dependent) scale, the circuit is not *qualitatively* affected; however, a *quantitative* change in the coefficient d_g/d_p occurs. Similar to the coefficient of an area law, this quantity is easily changed by a local finite-depth unitary. Within the characteristic length scale, on the other hand, the nature of the circuit is qualitatively changed from a short-ranged circuit encoding an area law state to a very long-ranged circuit, with unitaries connecting the current location of an excitation to its origin, and thus encoding volume-law entanglement. In the final state, this long-ranged circuit dominates the geodesic, with only the short-distance behavior which originates from the boundary of the circuit exhibiting some locality. This bears resemblance to the final state in other holographic theories of quantum quenches [87, 1], with the non-local part of the circuit playing the role of a black hole. The relation of our results for intermediate times to the model put forward in these references is an open question left for future work. We also note that some details of the emergent geometry, including in particular oscillations observed at times longer than the initial spreading of entanglement shown in Fig. 4.4, may be due to integrability of the model.

4.6 Light Cone Growth

In a complementary analysis to the geodesics discussed in Section 4.5, we can also characterize the emergent geometry of unitary networks through the growth of light cones. To define the light cone, we interpret the unitary circuit as creating the physical state from an initial product state (i.e., the reverse direction of how it is obtained in the algorithm) and track the effect of changing one of the unitary operators. For an illustration of the light cone in a unitary circuit representing a MERA state, see Fig. 4.5. It is important to note that a notion of causality is crucial for the definition of a light cone. In the disentangling circuits, this is ensured through the unitarity of each operator. This is a crucial difference to distance discussed in Section 4.3, which could in principle be generalized to non-unitary networks.

We define the width of the light cone emanating from a particular unitary operator as the number of physical sites whose state is affected by changing this unitary operator. Quantifying the depth of the light cone, however, is more subtle. In many ansatz states, such as a scale-invariant MERA, each layer is the same and one can thus simply count the number of layers. However, the operators in the disentangling circuits are all different, and furthermore become closer to the identity as the disentangling procedure progresses and the state approaches a product state. To measure the depth in the circuit, we employ the entangling power $P(\hat{U})$; recall (from the main text) that $P(\hat{U})$ is a measure related to the amount of bipartite entanglement a unitary can create in a multipartite state. We

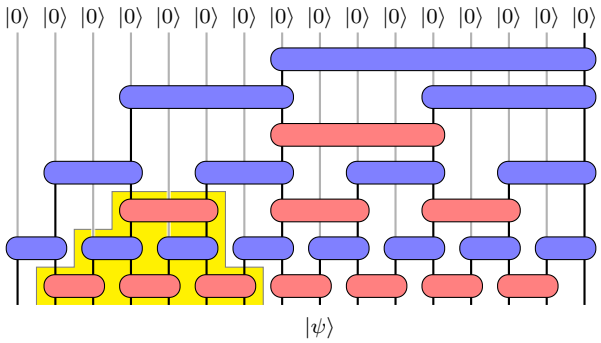

Figure 4.5: Two-local unitary network with the structure of a MERA state [213], illustrating the light cone of a bulk operator. To make the structure of the light cone more transparent, the network is interpreted as acting on a product state $|0\rangle^{\otimes L}$ (at the upper end), which is evolved into the physical state $|\psi\rangle$. Each tensor acts only on its ends (thicker lines). The red tensors correspond to disentanglers with two input and two output qubits, while the blue tensors are isometries that take a qubit of an entangled state (thick line) and a previously unentangled qubit (thin line) and entangles them. The circuit's structure defines a light cone emanating from each unitary in the circuit. Modification of the unitary at the top of the yellow-shaded region will only affect the circuit evolution and physical sites in the region; thus, the yellow region represents a light cone.

here use the accumulated entangling power of the steps τ up to some step t,

$$\mathcal{P}(t) = \sum_{\tau<t} P(\hat{U}(\tau)), \tag{4.2}$$

where $P(\hat{U}(\tau))$ is the entangling power of the unitary obtained in the τ'th iteration of the algorithm, to measure the depth into the circuit. We have also explored other measures for the depth, such as the total correlations [140, 139] (see definition below), the average bipartite entropy, and the average mutual information between pairs of sites. For all these quantities, qualitatively similar results are obtained. We restrict our discussion to $\mathcal{P}$ since it has an interpretation purely in terms of the circuit without having to refer to the initial state that the disentangling circuit is applied to.

In a MERA, the width of the light cone grows as $w \sim b^n$, where b is the number of

incoming legs on an isometry of the MERA, and n is the number of layers (see Fig. 4.5). Since the unitaries of a scale-invariant MERA are the same in each layer, the accumulated entangling power is $\mathcal{P} \sim n$, and thus $\log(w) \sim \mathcal{P}$. This reflects the fact that the entanglement of a critical system can be understood as a sum of equal contributions from each length scale [213]. Indeed, since the light cone in a MERA grows as b^n, and the entropy of a region of size l in a critical state follows $\frac{c}{3}\log l$ [192, 32, 83, 215], we have that the entropy of a reduced density matrix in a MERA after n layers is $S\left(\hat{\rho}(n)\right) \sim \frac{c}{3}\log(b^n) = \frac{nc}{3}\log(b)$ and thus $S\left(\hat{\rho}(n+1)\right) - S\left(\hat{\rho}(n)\right) = \frac{c}{3}\log(b)$. Each layer of the MERA captures the amount of entanglement encoded at a length scale b^n and makes a constant contribution proportional to the central charge of the system.

Below, we present numerical results for light cone growth as each step of a disentangling unitary circuit is applied. In addition to the Anderson model, we also analyze two further examples: an analogue of a random singlet phase in a chain of free fermions, as well as the André-Aubry model of electrons in a quasi-disordered potential, which exhibits a delocalized phase even when translational symmetry is broken.

4.6.1 Anderson Model

Our numerical results for light cone growth in the Anderson model (4.1) are summarized in Fig. 4.6. In the top panel, we show results for different strengths of the disorder potential. For $W = 0.1$, the localization length exceeds the system size and the expected scaling behavior for a critical system is observed: after an initial regime where the light

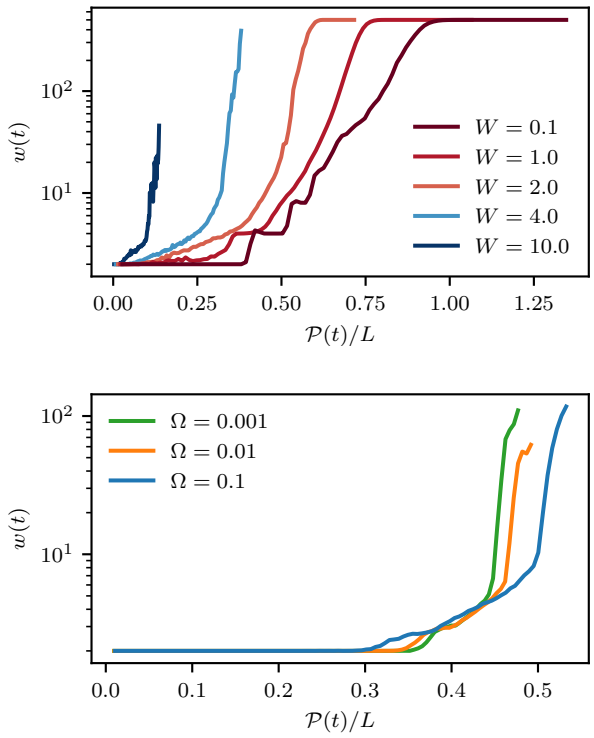

Figure 4.6: Width of the light cone $w(t)$. Here, t represents the number of steps into the disentangling circuit. *Top panel:* Ground states of the Anderson model for $L = 500$, for 200 disorder realizations. *Bottom panel:* Ground states in the random-singlet phase for $L = 700$, for 250 disorder realization.

cone width remains at $w = 2$, which can be attributed to short-range non-universal physics that is encoded in local correlations, there is a broad regime with the expected scaling of $\log(w) \sim \mathcal{P}$. This regime continues until w saturates to its maximum value. As the disorder strength in the Anderson model is increased and the localization length becomes comparable to the system size, we find that the initial plateau becomes much shorter and the width of the light cone increases very rapidly. This is consistent with the state having a limited amount of short-range entanglement and almost no long-range entanglement. For very strong disorder, the final steps of the circuit exhibit a very rapid growth of $w(t)$ with $\mathcal{P}(t)$. This is due to the fact that while almost all correlations are very local in these states, there is a very small amount of long-range correlations which is addressed by the last iterations of the algorithm and leads to large $w(t)$; however, since these correlations are very weak, the unitary operators that remove them are very close to the identity and thus contribute only very little to $\mathcal{P}(t)$. Therefore, the growth of $w(t)$ appears very steep in the final steps of the disentangling algorithm.

4.6.2 Random Singlet Phase

The Hamiltonian for the "random singlet phase" is given by

$$\hat{H} = -\sum_i J_i \left(\hat{c}_i^\dagger \hat{c}_{i+1} + \hat{c}_{i+1}^\dagger \hat{c}_i \right), \tag{4.3}$$

which we study at half filling. For $J_i = J = 1$, this model coincides with (4.1) for $W = 0$. However, upon introducing disorder by choosing the J_i randomly and identically distributed, the system flows to a strongly disordered fixed point known as the random

singlet phase [61]. At the random-singlet fixed point, the low-energy states take the form of a product of maximally entangled pairs, i.e. for every i there exists another site j such that $I(i:j) = 2\log 2$ is maximal, while $I(i:k) = 0$ for all $k \neq j$. Despite being very different from the ground states in the clean chain, the entanglement scaling is similar to critical systems with an effective central charge $\tilde{c} = \log 2$ [165].

To obtain the universal behavior of this fixed point in small systems, it is convenient to choose the couplings J_i from the fixed-point distribution,

$$P(J,\Omega) = \frac{\alpha}{\Omega}\left(\frac{\Omega}{J}\right)^{1-\alpha}\Theta(\Omega - J) \tag{4.4}$$

where $\alpha = -1/\log\Omega$. The exponent of the distribution is controlled by Ω: for $\Omega = e^{-1} \approx 0.368$, the exponent is 0 and the distribution is a box distribution of width Ω; for $\Omega \to 0$, the exponent becomes larger and larger. The random-singlet behavior is more pronounced at short scales (high energies) for smaller Ω.

The drastic difference between the structure of the random-singlet states in the lower panel of Fig. 4.6 and the eigenstates of the Anderson model with small W in the upper panel of Fig. 4.6 is very apparent in the growth of the light cones. The width of the light cone remains at $w = 2$ for most of the circuit, since most of the entanglement is encoded in two-local (long-ranged) operators. The deviations from this – that is, the point where the light cone grows to $w > 2$ – occur at later times as Ω is reduced, i.e. the system is brought closer to the ideal random-singlet fixed point. As shown in Sec. 4.7.4, the disentangling algorithm also converges drastically faster in the random-singlet phase. Similar to the Anderson model for strong disorder, the growth of $w(t)$ is very rapid in

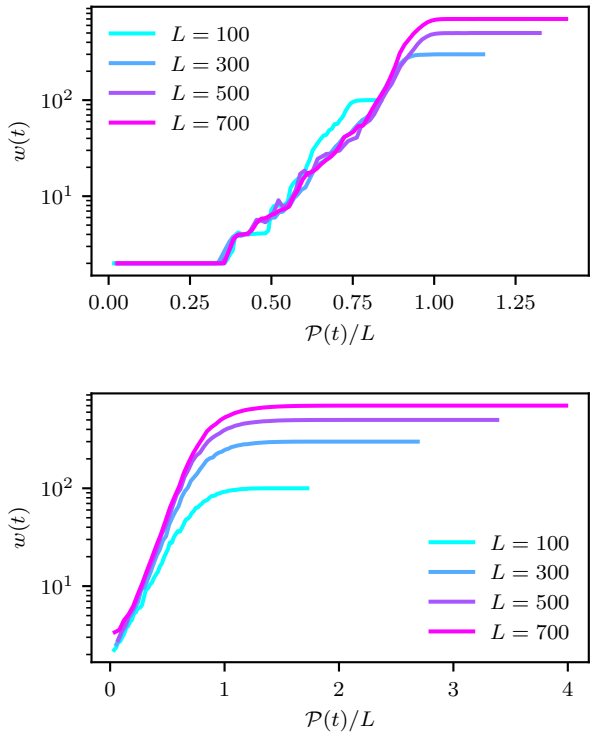

Figure 4.7: Light cone growth for the André-Aubry model at $\lambda = 0.1$. *Top panel:* Ground states. *Bottom panel:* Excited states. Note the different scales for the axes in the two plots.

the final stages of the algorithm.

4.6.3 André-Aubry model

As a final example, we consider the André-Aubry model [12] given by

$$\begin{aligned} \hat{H}_{\mathrm{AA}} = &- \sum_i \left(\hat{c}_i^\dagger \hat{c}_{i+1} + \hat{c}_{i+1}^\dagger c_i \right) \\ &+ \sum_i \lambda \cos(2\pi q i + \phi) \hat{n}_i, \end{aligned} \tag{4.5}$$

where $\hat{c}_i^\dagger$ creates a spinless fermion on the i'th site of a 1d lattice, $\hat{n}_i = \hat{c}_i^\dagger \hat{c}_i$, and we choose $q = (\sqrt{5}+1)/2$. The model is in a delocalized regime characterized by extended wavefunctions for $\lambda < 2$, while at $\lambda = 2$, the entire spectrum undergoes a localization transition into an Anderson insulator for $\lambda > 2$. Upon adding interactions, the system is known to undergo a many-body localization transition [92]. The fact that extended single-particle wavefunctions can persist even when translational invariance is locally broken by the external potential allows us to at the same time study large systems and obtain smooth results by averaging over different choices of ϕ.

In Fig. 4.7, we show the growth of light cones in these two cases for a system at half filling. In the case of ground states for small λ, the system exhibits the expected critical scaling $w(t) \sim \exp(\mathcal{P}(t))$ over almost three order of magnitudes in the largest system. In the case of excited states, on the other hand, the width of the light cones diverges very rapidly and saturates to the system size. This indicates that the entanglement is mostly encoded globally in the state.

4.7 Details of the disentangling algorithm

4.7.1 Ambiguity of local unitaries

As discussed in the main manuscript, an ambiguity arises since the unitary can always be followed by a swap of the two sites or a single-site unitary while keeping the mutual information the same. In order to partially lift this ambiguity, we choose the unitary to

minimize the entangling power $P(\hat{U})$. To define the entangling power of a two-site unitary $\hat{U}_{ij}$, consider its decomposition $\hat{U}_{ij} = \sum_\alpha \sqrt{\lambda_\alpha} \hat{X}_i^\alpha \otimes \hat{Y}_j^\alpha$, where $\hat{X}_i^\alpha$ and $\hat{Y}_i^\alpha$ are unitary operators acting on sites i and j, respectively, and $\mathrm{Tr}\left(\hat{X}_i^\alpha \hat{X}_i^\beta\right) = \mathrm{Tr}\left(\hat{Y}_j^\alpha \hat{Y}_j^\beta\right) = \delta_{\alpha\beta}$. We then define $P(\hat{U}) = -\sum_\alpha \lambda_\alpha \log(\lambda_\alpha)$. This quantity is closely related to the amount of entanglement the unitary can create between two systems, given additional ancilla systems (assisted entangling power, see e.g. Refs. [233, 219]).

4.7.2 Optimization of the two-site disentangling unitary

We now describe our strategy for quickly finding a two-site unitary U that maximally reduces the mutual information between two qubits i and j, $I(i:j) = S_i + S_j - S_{ij}$. Since the overall contribution S_{ij} must remain unchanged under unitary transformations, we only need to minimize $S_i + S_j$.

We can write a general unitary rotation on the two-qubit reduced density matrix in the form

$$\hat{U} = |00\rangle\langle 0| + |01\rangle\langle 1| + |10\rangle\langle 2| + |11\rangle\langle 3|, \tag{4.6}$$

where $|a\rangle = \{|0\rangle, \ldots, |3\rangle\}$ is an orthonormal basis for $\mathbb{C}^4$, $\langle a|b\rangle = \delta_{ab}$. Since we can apply a unitary to each qubit without affecting the entanglement properties, we can assume w.l.o.g. that U is chosen such that the reduced density matrices for the two qubits are diagonal,

$$\rho_i = \mathrm{Tr}_j\left(\hat{U}\rho\hat{U}^\dagger\right) = \begin{pmatrix} p_i & 0 \\ 0 & 1-p_i \end{pmatrix} \tag{4.7}$$

$$\rho_j = \mathrm{Tr}_i\left(\hat{U}\rho\hat{U}^\dagger\right) = \begin{pmatrix} p_j & 0 \\ 0 & 1-p_j \end{pmatrix}, \tag{4.8}$$

where

$$p_i = \mathrm{Tr}\left[\rho(|0\rangle\langle 0| + |1\rangle\langle 1|)\right] \tag{4.9}$$

$$p_j = \mathrm{Tr}\left[\rho(|0\rangle\langle 0| + |2\rangle\langle 2|)\right]. \tag{4.10}$$

The quantity we want to minimize is then

$$S_a + S_b = H_b(p_i) + H_b(p_j), \tag{4.11}$$

where $H_b(p) = -p\log p - (1-p)\log(1-p)$ is the binary entropy.

The strategy we pursue is to choose $|a\rangle$ to be the eigenvectors of ρ, in order of descending eigenvalue. If the eigenvalues of ρ are λ_α, $\lambda_\alpha \geq \lambda_{\alpha+1}$, then $p_i = \lambda_0 + \lambda_1$, and $p_j = \lambda_0 + \lambda_2$. This clearly minimizes S_i, as well as minimizing S_j under the constraint of keeping S_i minimal. While we do not provide a proof that this is the global optimum, further analytical calculation can show that this is a local minimum, and numerical tests have always shown this to be a global minimum.

4.7.3 Disentangling algorithm for free fermions

In the case of non-interacting fermions, the entanglement properties of the system are encoded entirely in the correlation matrix (equal-time Green's function)

$$C_{kl} = \langle \hat{c}_k^\dagger \hat{c}_l \rangle, \tag{4.12}$$

where $\hat{c}_k^\dagger$ creates a fermion on the k'th site of the lattice. Given a free-fermion Hamiltonian

$$\hat{H} = \sum_{k,l} h_{kl} \hat{c}_k^\dagger \hat{c}_l = \sum_\alpha \epsilon_\alpha \hat{d}_\alpha^\dagger \hat{d}_\alpha, \tag{4.13}$$

where ϵ_α are the single-particle energies and $\hat{d}_\alpha^\dagger = \sum_i w_{\alpha i} \hat{c}_i^\dagger$ creates a fermion in the α'th eigenstate,

$$C_{kl} = \sum_{\alpha \in F} w_{\alpha k} w_{\alpha l}^*, \tag{4.14}$$

where F is the set of filled orbitals.

The entanglement of a group of sites A is obtained by restricting C_{kl} to the sites in A, $C_{kl}^A = C_{kl}$ for $k, l \in A$, computing the eigenvalues λ_α of C^A, and then computing $S_A = \sum_\alpha H_b(\lambda_\alpha)$ [215, 156, 157], where H_b is again the binary entropy. In particular, for a single site the entropy is simply $S_i = H_b(C_{ii})$.

The mutual information between two sites $I(i:j)$ in a free-fermion state is therefore completely encoded in the 2×2 submatrix of the correlation matrix $C^{\{ij\}}$. Furthermore, if $C^{\{ij\}}$ is diagonal, the mutual information vanishes. To maximally reduce the mutual information, we therefore find the orthogonal rotation $R(\theta)$ of the fermion operators that diagonalizes $C^{\{ij\}}$.

On the many-body operators, this transformation acts according to

$$\hat{c}_i^\dagger \mapsto R(\theta)_{11} \hat{c}_i^\dagger + R(\theta)_{21} \hat{c}_j^\dagger \tag{4.15}$$

$$\hat{c}_j^\dagger \mapsto R(\theta)_{12} \hat{c}_i^\dagger + R(\theta)_{22} \hat{c}_j^\dagger \tag{4.16}$$

$$\hat{c}_i^\dagger \hat{c}_j^\dagger \mapsto \det\left(R(\theta)\right) \hat{c}_i^\dagger \hat{c}_j^\dagger. \tag{4.17}$$

This can be succinctly summarized in the block-diagonal matrix

$$U = \left(\begin{array}{c|cc|c} 1 & 0 & 0 & 0 \\ \hline 0 & & & 0 \\ 0 & & R(\theta) & 0 \\ \hline 0 & 0 & 0 & \det\left(R(\theta)\right) \end{array}\right), \tag{4.18}$$

where care must be taken to correctly implement fermionic anti-commutation rules when applying the off-diagonal elements.

It is interesting to note that for free fermions, the mutual information between two sites can *always* be reduced to zero. While many other entanglement properties of the free-fermion chain are similar to those of weakly interacting fermions in the same phase (for example, the CFT description and thus the universal terms in the entanglement entropy are the same), this is a strong indication of the simpler entanglement structure in non-interacting systems.

4.7.4 Convergence

To characterize the convergence of the unitary circuit towards a product state, we measure the distance from a product state [209]. For an easily computable measure of this distance, we rely on the "total correlation" [140, 139], which for a state $\hat{\rho}$ is given by

$$T(\hat{\rho}) = \sum_i S(\hat{\rho}_i) - S(\hat{\rho}), \tag{4.19}$$

where $\hat{\rho}_i$ are the reduced density matrices for sites i, and $S(\hat{\rho}) = -\operatorname{Tr}\hat{\rho}\log\hat{\rho}$. The total correlations have the property that $T(\hat{\rho}) = \min_{\hat{\pi}} S(\hat{\rho}||\hat{\pi})$, where $S(\hat{\rho}||\hat{\sigma}) = -\operatorname{Tr}(\hat{\rho}\log\hat{\sigma}) - S(\hat{\rho})$ is the relative entropy, which obeys $S(\hat{\rho}||\hat{\sigma}) \geq |\hat{\sigma} - \hat{\rho}|_1^2/2$, where $|\cdot|_1$ is the trace norm, and $\hat{\pi} = \hat{\pi}_1 \otimes \hat{\pi}_2 \otimes \ldots \otimes \hat{\pi}_L$ is the closest product state (in relative entropy) to

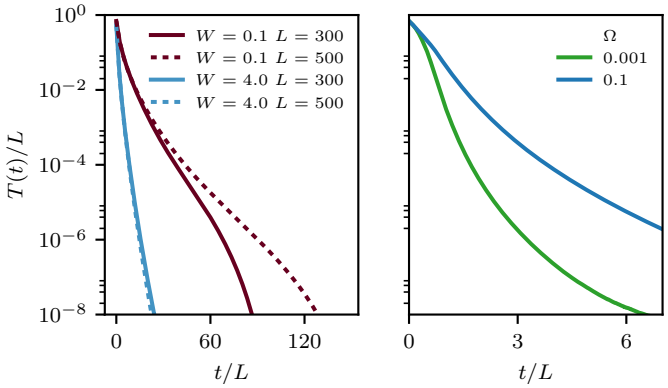

Figure 4.8: Convergence of the disentangling algorithm. Here, T denotes the total correlation as given in (4.19), and t represents the number of steps into the disentangling circuit. *Left panel:* Ground states of the Anderson model (4.1). For $W = 0.1$, the localization length exceeds the system size and the system is effectively critical on the length scales considered here, while for $W = 4$ the localization length is smaller than the system size and the effects of localization can be observed. Averaging has been performed over 100 disorder realizations. *Right panel:* Ground states in the random-singlet phase for $L = 700$, averaged over 250 realizations.

$\hat{\rho}$. Since we are working over pure states, $S(\hat{\rho}) = 0$ and $T(\hat{\rho})$ is easily computed, since we need to compute the $S(\hat{\rho}_i)$ in the course of the disentangling algorithm. It is worth noting that for pure states $\hat{\rho}$ and $\hat{\sigma}$, $|\hat{\rho} - \hat{\sigma}|_1 = \sqrt{1 - |\langle\hat{\rho}|\hat{\sigma}\rangle|^2}$.

In Fig. 4.8, we show the convergence of $T(t)/L$ (where $T(t)$ denotes the total correlation of the state after t iterations of the disentangling algorithm) for ground states of the Anderson model as well as the random-singlet model. We consider two disorder strengths for the Anderson model: one which leads to a localization length ξ_{loc} that exceeds the system size, while the other leads to a localization length ξ_{loc} short enough that localization can be observed for accessible system sizes (L up to 500 sites). In the strongly localized regime, we find very fast convergence that is almost independent of system size. This is expected since localized states obey an area law and are known to be generated

by finite-depth local unitaries [19]. In the weakly localized regime, convergence is slower and depends much more on the system size. This is expected since these states violate the area law with a logarithmic correction up to the relevant length scales.

For the random-singlet phase (not shown), we find very rapid convergence to a product state, even though the bipartite entanglement of the initial state is comparable to that of a critical system. This can be explained by the very simple structure of these quantum states, whose entanglement is almost all contained in simple two-site correlations. Convergence is faster for smaller Ω, where the finite-size states are closer to the random-singlet fixed point.

4.8 Outlook

While we have so far applied our methods to systems where a holographic description is already known, the fact that we did not make use of any *a priori* knowledge of these systems makes our methods ideally suited to systems with no known holographic description. Most prominently, this includes the many-body localization transition [18, 149, 152, 16, 19, 127], which is known to be characterized through entanglement properties [19] while the details of the transition remain controversial [69, 103, 231].

4.9 Acknowledgments

We thank M. P. A. Fisher, G. Refael and J. Sonner for insightful discussions, and A. Antipov and S. Fischetti for comments on earlier drafts of this manuscript. James R. Garrison was supported by the NIST NRC Research Postdoctoral Associateship Award, by the National Science Foundation under Grant No. DMR-14-04230, and by the Caltech Institute of Quantum Information and Matter, an NSF Physics Frontiers Center with support of the Gordon and Betty Moore Foundation. This material is based upon work supported by the National Science Foundation Graduate Research Fellowship under Grant No. DGE 1144085. Any opinion, findings, and conclusions or recommendations expressed in this material are those of the authors(s) and do not necessarily reflect the views of the National Science Foundation. We acknowledge support from the Center for Scientific Computing at the CNSI and MRL: an NSF MRSEC (DMR-1121053) and NSF CNS-0960316. This work was in part performed at the Aspen Center for Physics, which is supported by National Science Foundation grant PHY-1066293.

Chapter 5

Quantum Quenches and Entanglement Geometry

5.1 Introduction

In Chapter 4 we developed an algorithm to disentangle generic quantum wavefunctions to product states, generating a tensor network description of the wavefunction which can be analyzed to determine its entanglement structure and which can reproduce aspects of the AdS/CFT holographic duality.

A rich body of literature exists related to using AdS/CFT to predict how quantum quenches applied to the CFT side are expressed on the AdS bulk dual [87, 1, 190] through the mapping dictionary and, conversely, how perturbations in the gravity theory can be observed in the surface properties [23, 189, 143, 5] of the CFT. Inspired by this line of

inquiry, we wish to extend the established results of the previous Chapter to develop better understanding of the interplay of quenching and disorder. In previous work, we focused on the Anderson model (reproduced below) at one disorder strength, $W = 8$, at a single system size:

$$\hat{H} = -t \sum_i \left(\hat{c}_i^\dagger \hat{c}_{i+1} + \hat{c}_{i+1}^\dagger \hat{c}_i \right) + \sum_i w_i \hat{c}_i^\dagger \hat{c}_i, \tag{5.1}$$

where $\hat{c}_i^\dagger$ creates a spinless fermion on the i'th site of a chain of length L. w_i is drawn from a uniform distribution between $[-W/2, W/2]$. Throughout this Chapter, we work with periodic boundary conditions, set $t = 1$ as an overall energy scale, and focus on Slater determinants at half filling.

We perform the same instantaneous quenching procedure as in Chapter 4:

1. Prepare the system in the groundstate of the disordered Anderson model (5.1).

2. Time evolve the system from $t = 0 \to t = t_f$ using the $W = 0$ Anderson Hamiltonian.

Because the model we consider is non-interacting, we are again able to exploit the fact that the algorithm can be used on the matrix of two-point correlation functions (see Sec. 4.2). This allows us to calculate the equal time Green's functions at various distances and times throughout the quench easily and to relatively quickly find disentangling circuits for all the disorder strengths and system sizes we consider.

We find that the disorder strength sets an effective energy density, reflected throughout the quench. When the quench occurs and the disorder vanishes, excitations are free to move through the system and the number of these excitations increases with the

pre-quench disorder strength. This leads to interesting behavior which reveals itself in a variety of observables. First, in Sec. 5.2 we examine the behavior of the equal time Green's function. We find that for a localized initial state it increases monotonically outward as the wavefront of excitations spreads, finally reaching a "flat" steady-state late in the quench. The geodesics and entanglement entropy, discussed in more detail in Sec. 5.3, display two regimes: an initial rapid change – increasing to a volume law for the entanglement entropy, decreasing geodesic length – which stabilizes into a long-time regime of slowly decaying oscillations. The oscillation amplitude is set by this effective energy density from the disorder strength. The oscillation period is controlled by system size L.

5.2 Equal Time Green's Functions

The real space equal time Green's function at time t is given by:

$$\mathcal{G}(r,t) = \sum_{i=1}^{L} \left\langle \hat{c}_i^\dagger(t)\hat{c}_{i+r}(t) \right\rangle \tag{5.2}$$

In Fig 5.1 we examine the behavior of $\mathcal{G}$ over all pairs of sites separated by distance r, up to distance $L/2$ (since we use periodic boundary conditions) for a variety of quench times. The $W = 2$ plots begin in the regime of the Anderson model where the localization length ξ_{loc} is longer than the system size L, which explains the higher correlations at longer distances early in the quench (darker). Initially, as expected, the equal time

Green's function decays exponentially with distance, capturing the exponential decay of correlations in the regime where $\xi_{\text{loc}} > L$. During the quench (as the line coloring lightens) the system crosses over to a volume law, and as this occurs sites further and further apart become more and more correlated, until the late-time behavior where the equal time Green's function is saturated and flat for almost all site separation distances and does not oscillate. This is in contrast to the entanglement entropy $S(L/2, t)$, which does oscillate even at late times in the quench.

5.3 Geodesic Rescaling

As the quench proceeds we observe two distinct regimes for the geodesic distance $d_g(d_p, t)$:

- Very fast initial drop of geodesic distance early in the quench
- Very slowly decaying oscillatory behavior

Fig. 5.3 shows the length of the longest geodesic (averaged over all pairs of sites distance $L/2$ apart) as a function of quench time t for various disorder strengths W at fixed $L = 250$ and Fig. 5.2 similarly for system sizes L for fixed disorder strength $W = 7.0$. Note that the time has been rescaled by system size L in Fig. 5.2, showing that the periodicity in region (2) is controlled by the system size.

In Fig. 5.3 and Fig. 5.2, the geodesic for the longest accessible physical site separation distance d_p ($L/2$ due to periodic boundary conditions) is shown, along with the maximum entangling power $P(\tau)$ (see Eq. (4.2)) reached by the longest geodesic at that quench time,

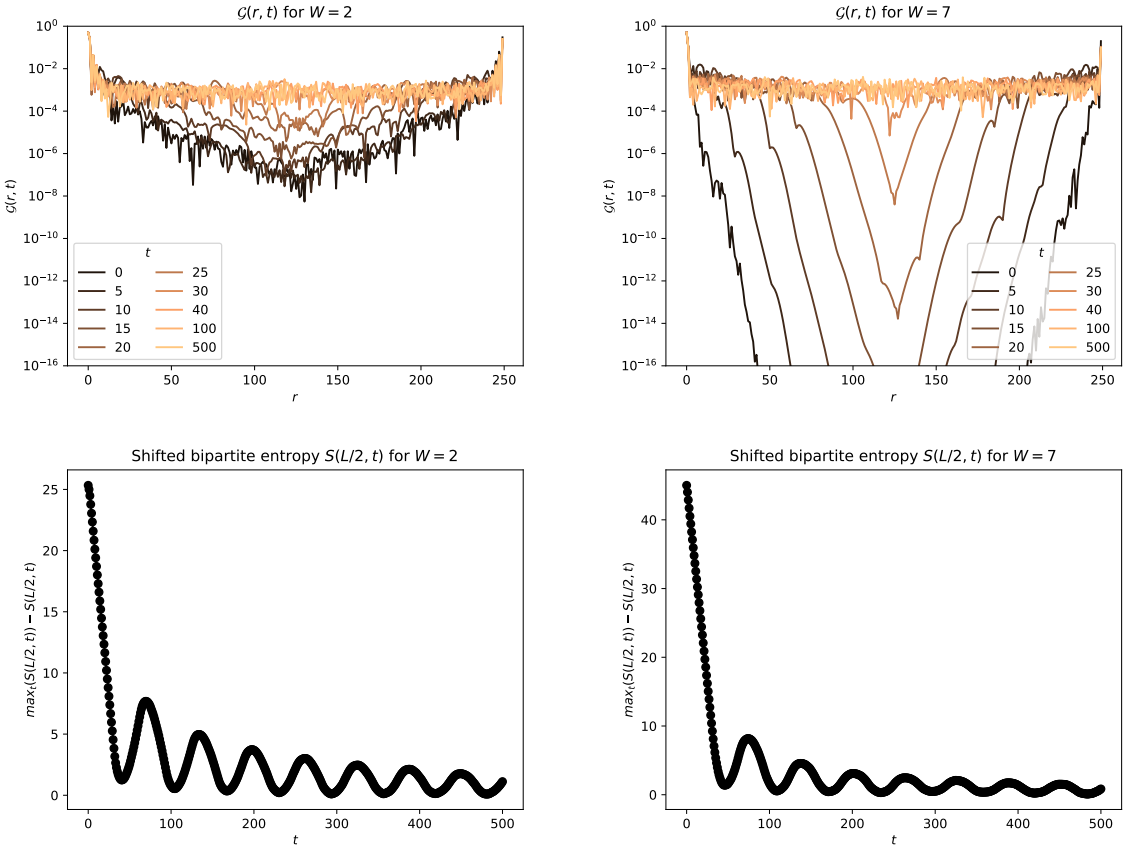

Figure 5.1: Equal time Green's function (top) in Eq. (5.2) and shifted bipartite entanglement entropy $\max_t\left(S(L/2,t)\right) - S(L/2,t)$ (bottom) for $L = 250$, $W = 2$ (left) and $W = 7$ (right). At early times in the quench (darker) the exponential decay of correlations is seen, while later (lighter) in the volume law state the Green's function is essentially flat at medium-to-long distances.

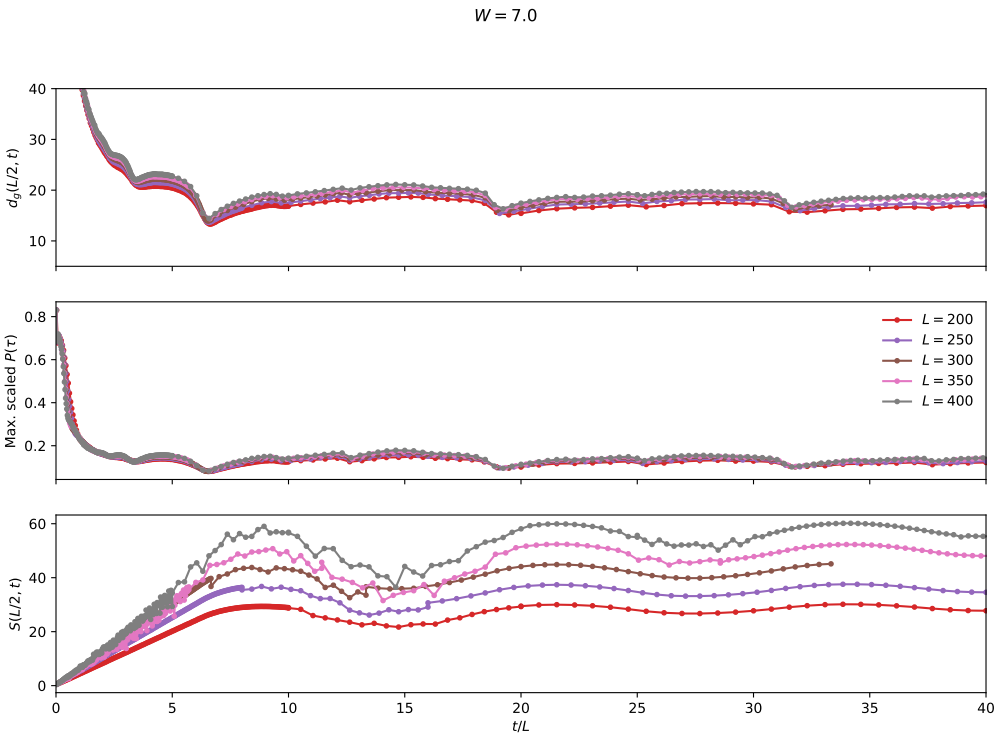

Figure 5.2: Geodesic distance $d_g(L/2, t)$ corresponding to physical distance $L/2$ (top), maximum scaled entangling power reached along that geodesic (middle), and bipartite entanglement entropy $S(L/2, t)$ (bottom) throughout the quench. Note that quench time has been rescaled by system size L to emphasize that the periodic behavior depends on L. These data are for a single disorder strength $W = 7$.

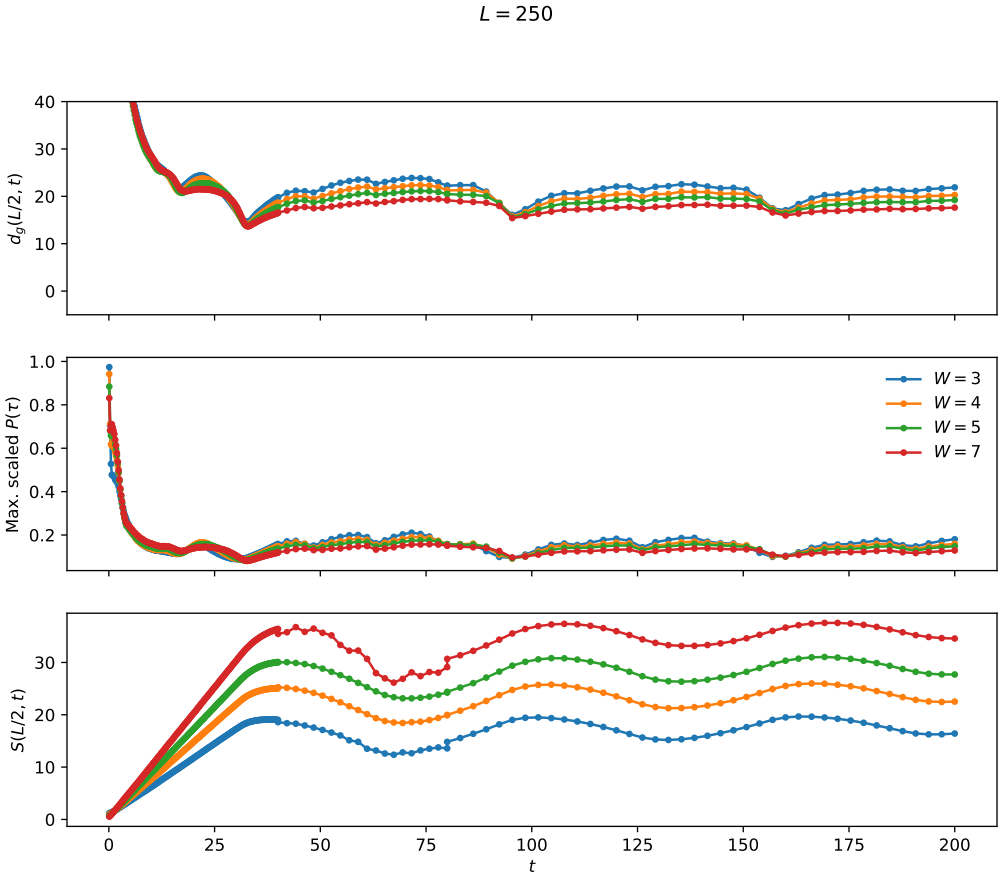

Figure 5.3: Geodesic distance $d_g(L/2, t)$ corresponding to physical distance $L/2$ (top), maximum scaled entangling power reached along that geodesic (middle), and bipartite entanglement entropy $S(L/2, t)$ (bottom) throughout the quench. In contrast to Fig. 5.2, here all data are for $L = 250$, and different disorder strengths W are compared, two of which ($W = 5, W = 7$) are in the $L > \xi_{\text{loc}}$ regime and two of which ($W = 3, W = 4$) are in the $L < \xi_{\text{loc}}$ regime.

and the bipartite entanglement entropy $S(L/2,t)$ at the beginning of the disentangling procedure. From these data it is clear that the periodicity of the entanglement entropy and the corresponding geodesics are linked, and that both reach their "long time" (region (2)) behavior together as the system arrives at volume law entanglement scaling.

Once the geodesics have stabilized into region (2) they have an interesting oscillatory pattern which has slowly decaying amplitude. This oscillatory behavior is also present in the bipartite entanglement entropy $S(L/2,t)$, but interestingly does *not* seem to be present in the equal time Green's function shown in Fig. 5.1. One might be concerned that this is an artifact of the choice to examine these long-range separation distances for d_g and large cuts for S. Fig. 5.4 shows that the relationship persists for a much smaller $d_p = L/10$.

The system achieves the volume law bipartite entanglement entropy at the same quench time as the geodesics reach the region of very slowly decaying oscillations, and the minima in geodesic length correspond to maxima in bipartite entanglement entropy through time - the two have the same period. This period is independent of disorder strength W and is controlled entirely by the system size L, as can be seen in Fig. 5.2. The disorder strength W does control the amplitude of the oscillation, as seen in Fig. 5.3 and Fig. 5.4, with stronger disorder leading to larger amplitudes. This is as expected in our interpretation of larger disorder strength as creating more excitations which are then able to move through the system (leading to higher entropy) after the quench occurs.

Later in the quench the peaks of both geodesic length (for fixed d_p) and $S(d_p,t)$

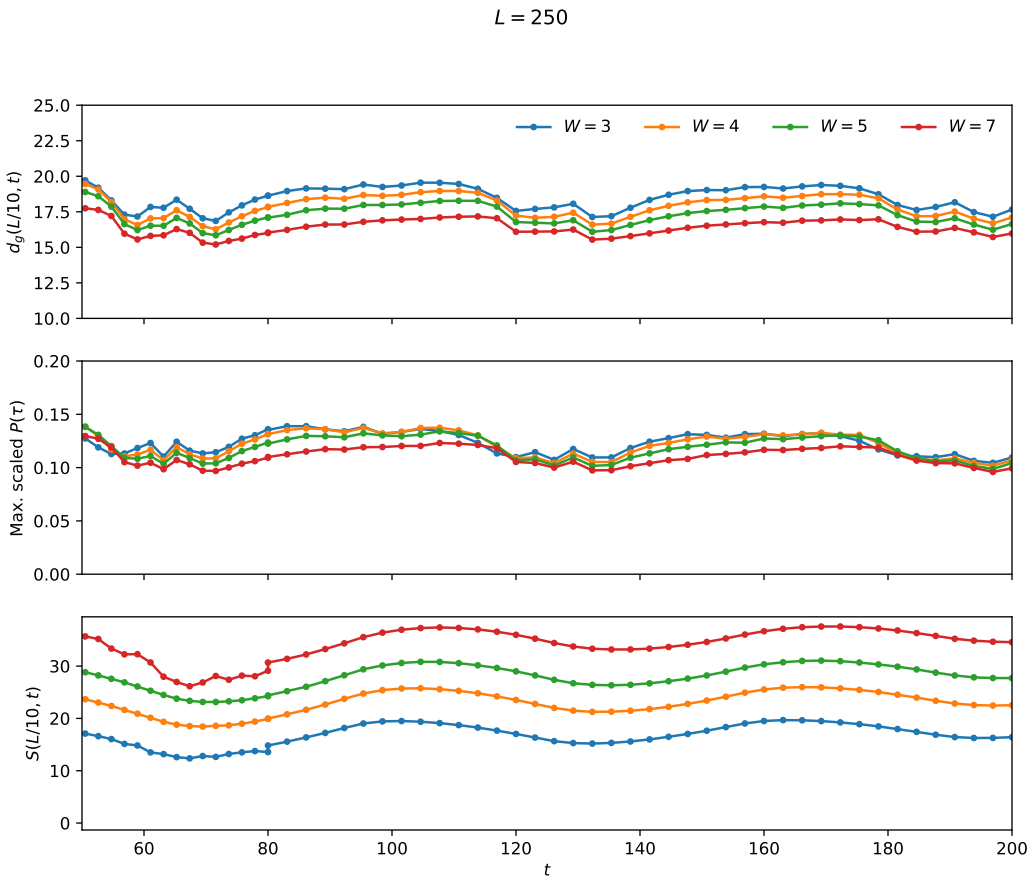

Figure 5.4: Geodesic lengths $d_g(L/10, t)$ (top), fraction of circuit entangling power reached along those geodesics (middle), and entanglement entropy $S(L/10, t)$ (bottom) corresponding to physical distance $d_p = L/10$ for $L = 250$ and various disorder strengths W.

Scaling	$W = 3$	$W = 4$	$W = 5$	$W = 7$
Exponential	1.057×10^{-6}	9.623×10^{-5}	3.418×10^{-5}	1.453×10^{-4}
Polynomial	6.122×10^{-5}	1.055×10^{-8}	1.324×10^{-5}	1.250×10^{-5}

Table 5.1: Residuals of the linear regression for $L = 250$ half-system geodesics.

Scaling	$W = 2$	$W = 7$
Exponential	0.36814	0.477891
Polynomial	0.0894624	0.0790413

Table 5.2: Residuals of the linear regression for $L = 50$ half-system entanglement entropy.

slowly decay in amplitude. To understand how this occurs in Fig. 5.5 we show a series of semi-log and log-log plots of the half-system separation distance $d_p = L/2$ geodesic lengths $d_g(d_p = L/2, t)$ for fixed L and various disorder strengths W on either side of the crossover between the system size L being smaller than localization length ξ_{loc} and L being the larger of the two at $W \approx 4$. We compute a linear regression of peak maxima against quench time in both cases, computing residual errors to determine which fit best represents the peak decay. The residuals are presented in Table 5.1.

Since determining the entanglement entropy is much less computationally intensive than both quenching and subsequently generating disentagling circuits from which to extract geodesic information and the two measures track each other, we also perform a long time quench and infer the behavior of the geodesics from the entanglement entropy. In Fig. 5.6 a similar analysis to the one in Fig. 5.5 is performed, and with more input to the regression the polynomial fit matches best. The residuals in these fits are presented in Table 5.2.

The slope of the line in this log-log fit is approximately -1, indicating that the peaks

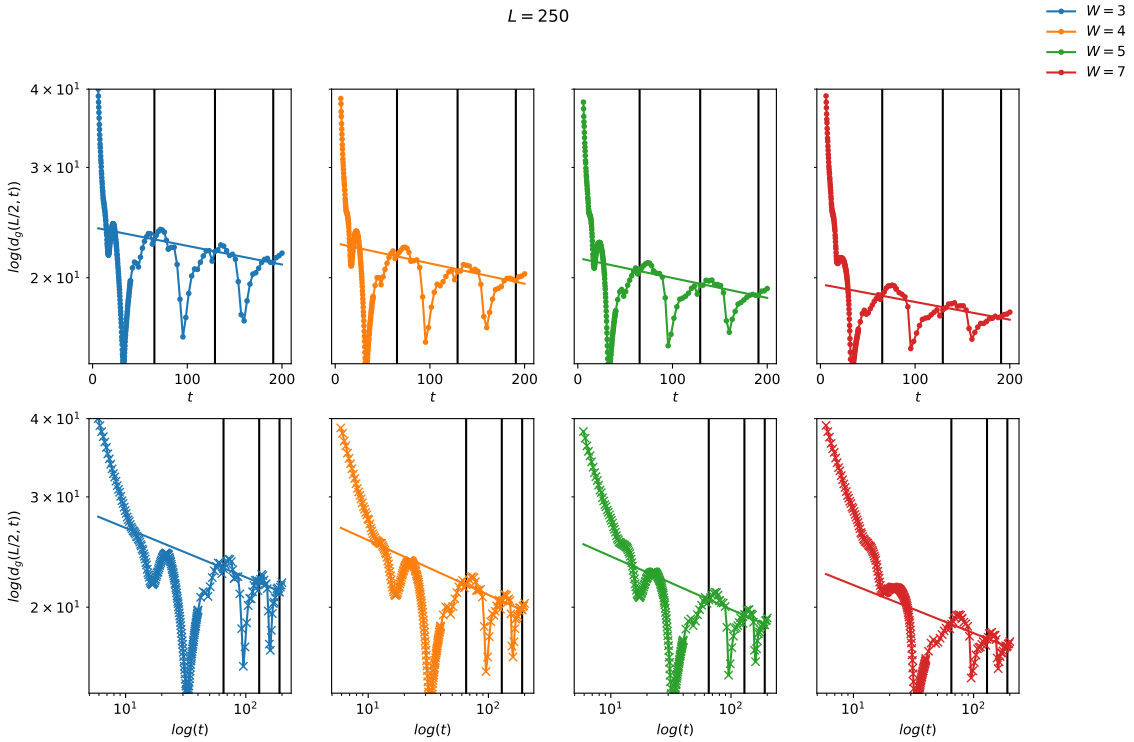

Figure 5.5: Fits of $\log(d_g)$ against t (top) and $\log(t)$ (bottom). The black lines represent the points used to compute the fit. The line drawn represents the result of the linear regression. All data are for $L = 250$.

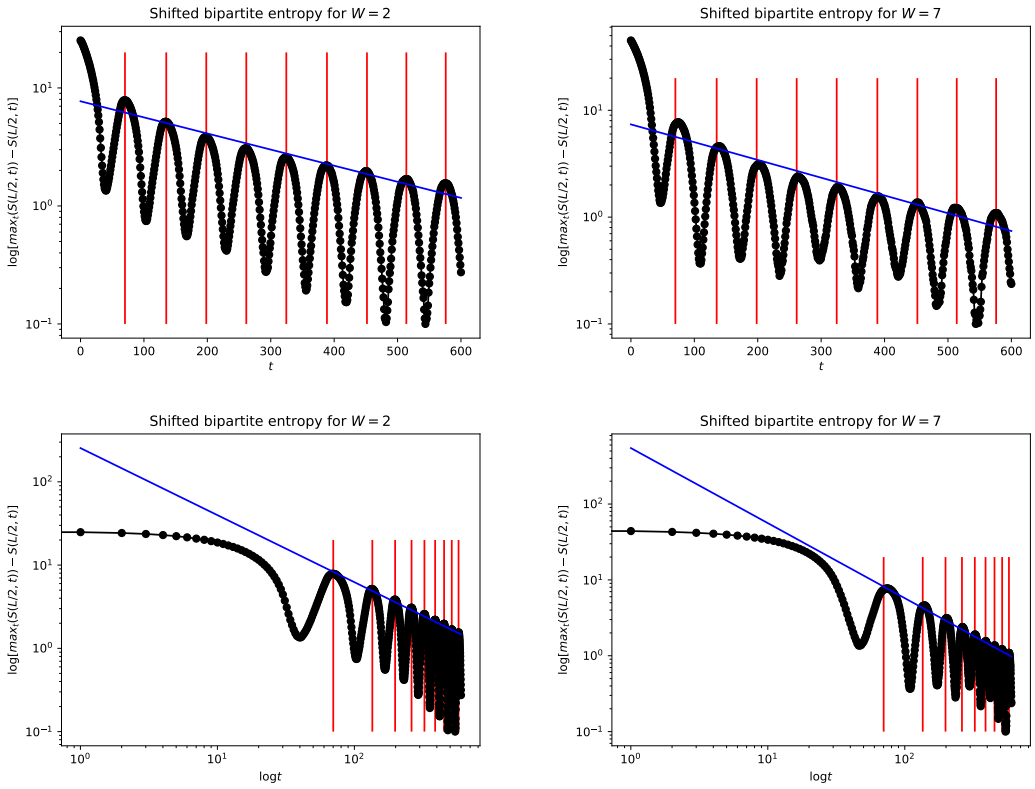

Figure 5.6: Fits of shifted bipartite entanglement entropy $\max_t(S(L/2,t)) - S(L/2,t)$ against t (top) and $\log(t)$ (bottom) for disorder strengths $W = 2$ (left, initially $L < \xi_{\text{loc}}$) and $W = 7$ (right, initially $L > \xi_{\text{loc}}$). The red lines represent the points used to compute the fit. The blue line drawn represents the result of the linear regression. All data are for $L = 250$.

seem to decay linearly in quench time. In this plot we subtract the entropy at each quench time (*not* disentangling time τ) from the maximum entanglement entropy for that physical distance ($d_p = L/2$) over *all* quench times. This accounts for the effective energy density difference introduced by different disorder strengths.

As in Fig. 5.4 it is interesting to see how the geodesics oscillate in time over the range of possible physical distances. In Fig. 5.7, the geodesic distances $d_g(d_p, t)$ are shown for all physical separation distances $d_p > 10$ (shorter distances have very small geodesic

lengths) after the oscillatory behavior has begun, $t >\sim 23$ for $L = 250$. For times before this, the system is still in regime (1), working towards the volume law, and the geodesics in this regime are much longer, washing out interesting features in regime (2). From this we can observe that the feature of geodesic maximization/minimization oscillates across the system through time.

5.4 Correlation Reconstruction

Another question of interest is how much information, especially local information, portions of the disentangling circuit are able to capture and represent? The total circuit must be able to represent all the information in the original physical state, since it can be run in reverse to regenerate that state from the totally disentangled product state. This circuit may be extremely long, especially for highly-entangled states such as volume law states. If it is possible to truncate the circuit and still retain an accurate recipe (in the form of the shorter circuit) for generating a state with good overlap with the original, this would be valuable from a state preparation perspective. A shorter circuit which retains essential information about the state is also more computationally tractable on a classical computer. It is also interesting to determine whether local correlations are removed first or whether correlators at all distances are reproduced equivalently quickly in disentangling time.

We examine reconstructions of the previously discussed quenched wavefunctions. Again, since these are all free fermion models, we are able to represent the wavefunction

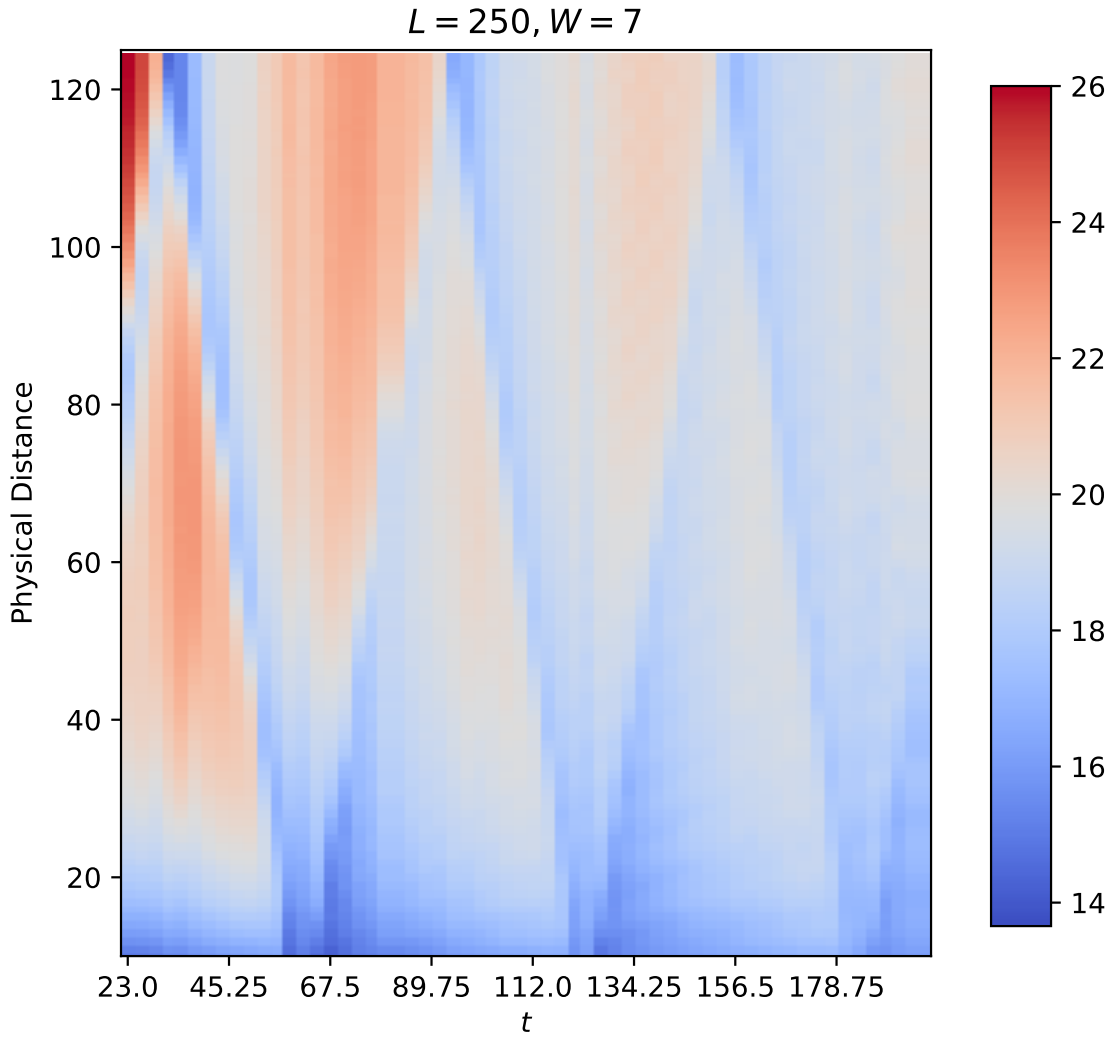

Figure 5.7: Heatmap of the geodesic lengths $d_g(d_p, t)$ (color) as a function of physical distance d_p (y axis) and quench time t (x axis).

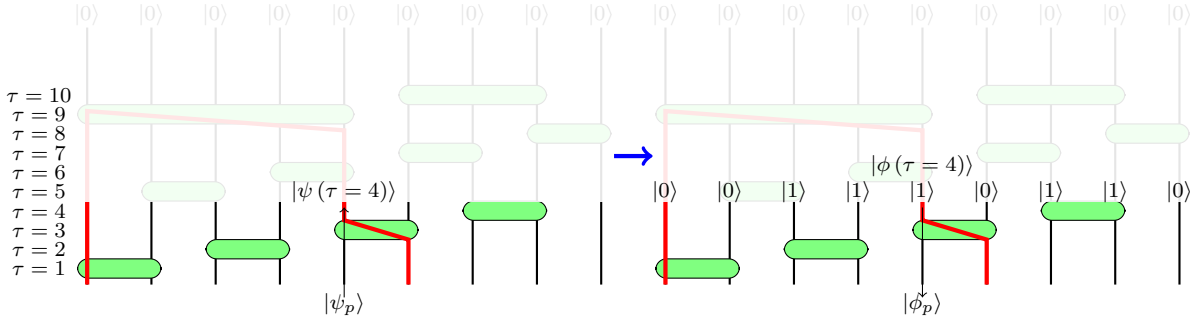

Figure 5.8: The process of rebuilding the wavefunction for step $\tau = 4$. The first 4 gates are applied to the starting wavefunction $|\psi\rangle$ (left), which is then clamped to a product state and run in reverse to generate $|\psi'\rangle$ (right). If the entire circuit were included, $|\psi'\rangle = |\psi\rangle$. If fewer gates are included, the difference between the correlations of $|\psi'\rangle$ and $|\psi\rangle$ can be compared using the previously defined measures Eq. (5.4) and Eq. (5.4).

as its two-point correlation matrix, which makes running the disentangling circuit in reverse feasible. Our procedure for reconstruction at a given disentangling step τ (τ-th gate in the circuit) is:

1. Apply the first τ gates to the beginning physical state $|\psi_p\rangle$, giving $|\psi(\tau)\rangle = \prod_{j=1}^{\tau} \hat{U}_j \, |\psi_p\rangle$, and partially disentangling $|\psi_p\rangle$.

2. Project $|\psi(\tau)\rangle$ (in the form of its correlation matrix) so that it forms a product state $|\phi(\tau)\rangle = \otimes_{i=1}^{L} |\chi_i\rangle$.

3. Run the first τ gates *in reverse*, re-entangling $|\phi(\tau)\rangle$ to $|\phi_p\rangle = \left[\prod_{j=1}^{\tau} \hat{U}_j\right] |\phi(\tau)\rangle = \hat{U}_1^\dagger \otimes \hat{U}_2^\dagger \otimes \ldots \otimes \hat{U}_{\tau-1}^\dagger \otimes \hat{U}_\tau^\dagger \, |\phi(\tau)\rangle$.

4. Measure the agreement in correlators between the original physical state $|\psi_p\rangle$ and the reconstructed state $|\phi_p\rangle$.

A schematic of this procedure is presented in Fig. 5.8.

There are many possible choices of "metric" of agreement or difference between the reconstructed state and the physical state. For a given distance, we choose to compute the root mean square (RMS) difference defined in Eq. (5.4):

$$A(r,t,\tau) = \left\langle C_{\psi(t)}(r) - C_{\phi(\tau)}(r) \right\rangle = \sqrt{\sum_{i=1}^{L} \left[\left(C_{\psi(t)}^{i,i+r} \right)^* - C_{\phi(\tau)}^{i,i+r} \right]^2} \tag{5.3}$$

We can view $A(r,t,\tau)$ as a measure of "absolute" difference. However, it does not take into account the fact that at large r, $C^{i,i+r}$ will be smaller than at small r. In fact, it may be exponentially smaller. This may mask disagreement in the reconstruction. Therefore we also consider a relative measure, dividing the difference by its value at the start of the circuit (since $|\phi(0)\rangle = |\psi\rangle$, because no gates have yet been applied) to give:

$$R(r,t,\tau) = \frac{1}{A(r,t,0)} \left\langle C_{\psi(t)}(r) - C_{\phi(\tau)}(r) \right\rangle \tag{5.4}$$

We apply the reconstruction procedure throughout the quench time t for disorder strengths $W = 2, 3, 7, 8$. Since performing reconstruction is extremely time-intensive we only do so for $L = 50$, $L = 100$, and $L = 150$. For larger τ (more of the circuit included), the difference should decrease towards 0 for the two metrics.

Since the number of gates varies between disorder realizations, we consider a binned average of scaled entangling power $\mathcal{P}_S$. The scaled entangling power at a gate is the accumulated entangling power up to that gate, working "inwards" from the physical state, divided by the total entangling power of the circuit. The total entangling power of the circuit is the same as the accumulated entangling power at the last gate before

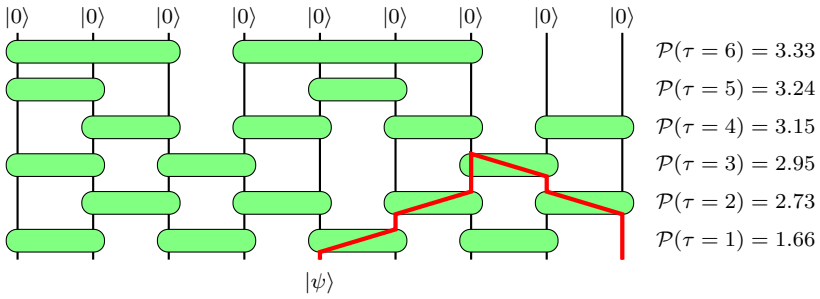

Figure 5.9: Example of a two-local disentangling unitary circuit. The thick red line indicates a geodesic between the 5th and 9th qubit (from the left). At each step, on the right we show the accumulated total entangling power. As in a real disentangling circuit, most of the correlations are removed early on.

the completely disentangled product state. We compute 20 bins between 0 and 1 for the entangling power, where the value corresponding to 1 occurs at the last (deepest) gate. This allows us to compare like-to-like in the difference metrics, since some circuits may have a long series of "ineffective" disentangling gates which each contribute little entangling power, and other circuits many have fewer gates but each of these has much stronger entangling power. To compute maximum scaled entangling power along a path through the circuit, we compute the total entangling power reached at each gate touched by the path and compute the maximum of these, then divide this value by the total entangling power of the entire circuit. As an example, consider Fig. 5.9. The maximum scaled entangling power of the geodesic shown there in red would be $2.95/3.33 = 0.8858$.

The relative difference data presented in Fig. 5.10 and Fig. 5.11 do not seem especially amenable to simple interpretation. We can confirm that this rescaling allows the difference at all length scales to be compared on the same footing. For the strong disorder case at short times in the quench, we see that the agreement is very bad for intermediate

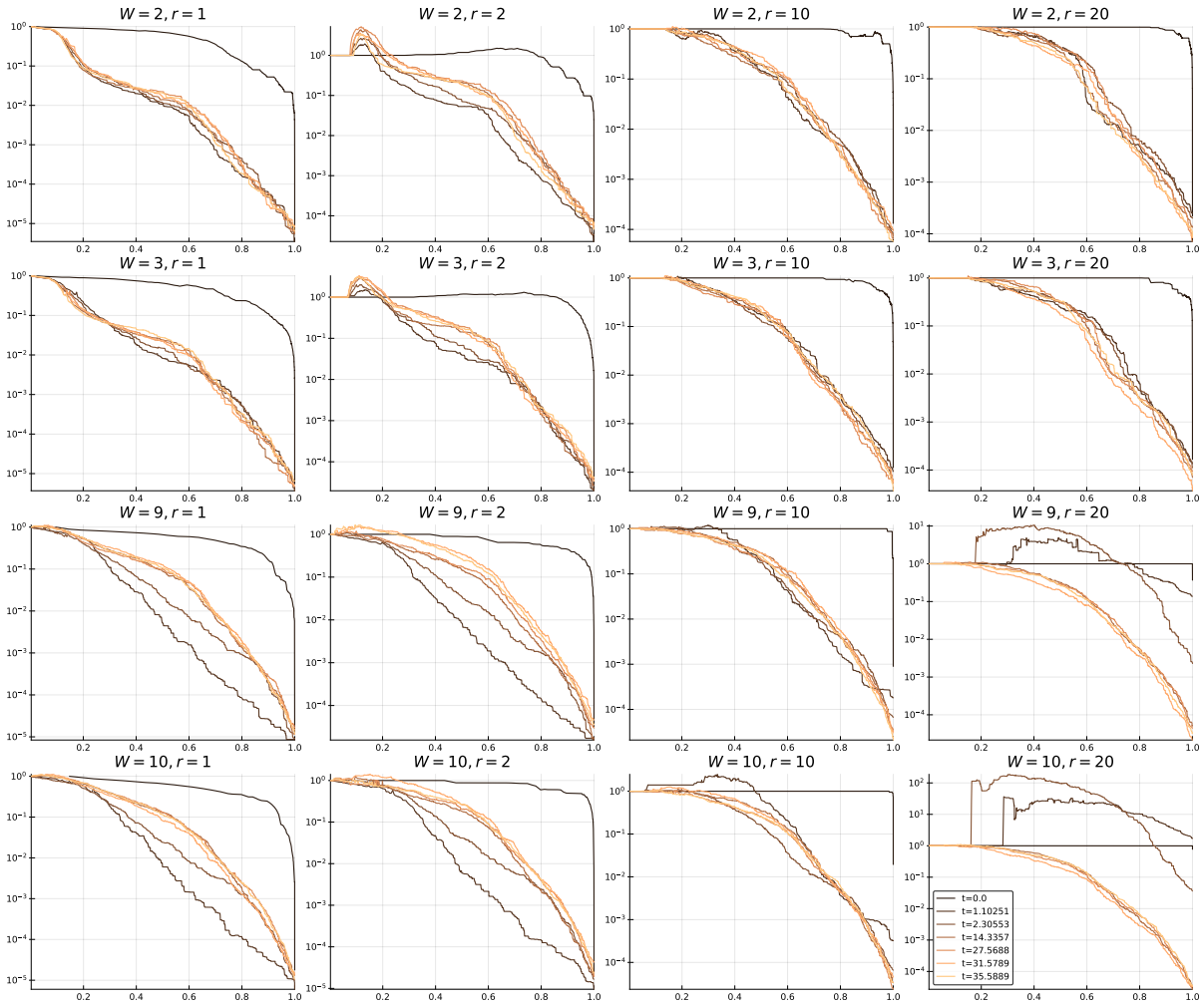

Figure 5.10: Relative difference $R(r, t, \mathcal{P}_S)$ for a variety of quench times t and physical site separation distances r. The color indicates the quench time – darker is earlier (with black indicating the initial state before the quench) and lighter and browner is later. Note that before the quench begins (darker), the entire circuit must be included. These data include reconstructions for all τ (and therefore $\mathcal{P}_S$), not only the gates before the maximum geodesic penetration. For this reason, eventually all physical separation distances agree at all quench times. For short distances (leftmost columns) at all disorder strengths W the reconstructions make progress monotonically. For longer distances (rightmost columns), especially at stronger disorder (lower panels), the relative difference *grows* initially in scaled entangling power. A possible interpretation is that the reconstruction is not effectively reproducing the small long-distance correlations of $|\psi_p\rangle$ – note that this effect vanishes for longer quench times when the system is in the volume law. All data are for $L = 50$.

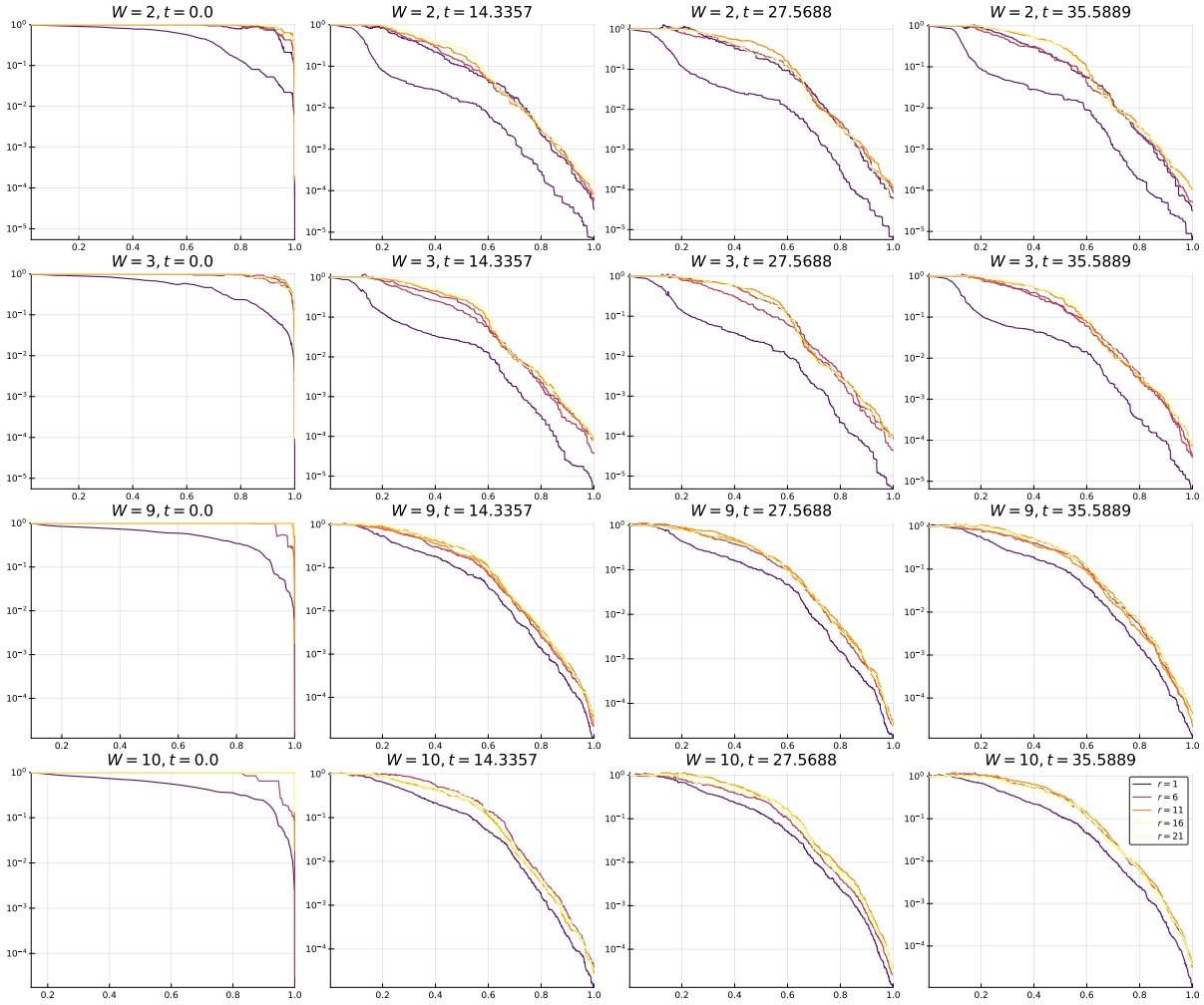

Figure 5.11: Relative difference $R(r, t, \mathcal{P}_S)$ for a variety of physical site separation distances r. The color indicates the physical separation distance - purpler is shorter, yellower is longer. The closest sites (purple) seem to achieve agreement earlier in the reconstruction than sites further away (yellower colors), and this is especially pronounced for weaker disorder (top two rows of panels, $W = 2$ and $W = 3$) All data are for $L = 50$.

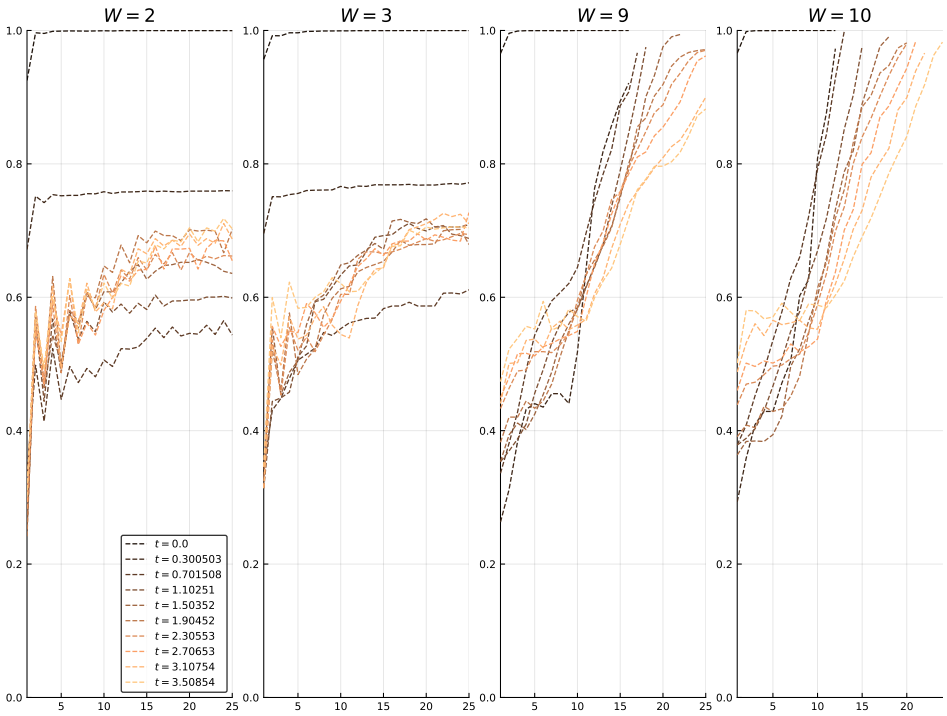

Figure 5.12: Scaled entangling power $\mathcal{P}_S$ (y axis, intuitively, the fraction of the circuit) needed to reach relative difference $R(d_p, t, \mathcal{P}_S)$ (Eq. (5.4)) < 0.05 for all physical separation distances d_p (x axis). Color indicates time in the quench, with darker indicating earlier and lighter later. All data are for $L = 50$.

τ because $A(r, t, \tau) \gg A(r, t, 0)$. Here, reconstructions over the entire circuit are performed, and so eventually the difference falls to zero as expected (since the entire circuit must reproduce $|\phi_p\rangle$).

Finally, we examine how far into the circuit we must reconstruct in order to reach certain threshold differences. These data are shown in Fig. 5.12. These plots show the minimum scaled entangling power required to capture correlations up to relative difference of 0.05, which indicates a very good reproduction of the correlations of the physical wavefunction $|\psi(t)\rangle$ at quench time t (and "disentangling time" $\tau = 0$). Again it is noticeable that the entire circuit must be included early in the quench (black) to

accurately reproduce correlations at any distance, while later, as the system achieves the volume law, much less is needed, especially at short separation distances. Note that for the weaker disorder (left columns), late in the quench the necessary scaled entangling power saturates, while for stronger disorder (right columns), it grows with r. This seems to provide some evidence for the supposition that the circuits reproduce local correlations earlier than longer distance correlations, especially in the states with longer initial localization length.

5.5 Conclusions

We examined the relationships between various metrics of quantum circuits generated by our previously developed disentangling algorithm. We focus on systems of free fermions as we instantaneously quench the initial disordered physical state with the non-disordered version of the Hamiltonian of which it is a groundstate. Examining how circuit properties change with properties of the physical state through the quench, we find an interesting relationship between the entanglement entropy and geodesic distances which is not present in the equal time Green's function.

It would be interesting to try to connect these relationships with those developed in the AdS/CFT framework. Since we work with lattice models, and most of the results in AdS/CFT were developed for the continuum, so making such connections would likely be nontrivial.

Bibliography

[1] Javier Abajo-Arrastia, João Aparício, and Esperanza López. Holographic evolution of entanglement entropy. *Journal of High Energy Physics*, 2010(11):149, 2010.

[2] Miguel Aguado and Guifre Vidal. Entanglement renormalization and topological order. *Physical review letters*, 100(7):070404, 2008.

[3] Ofer Aharony, Steven S. Gubser, Juan Maldacena, Hirosi Ooguri, and Yaron Oz. Large n field theories, string theory and gravity. *Physics Reports*, 323(3–4):183 – 386, 2000.

[4] Fabien Alet and Nicolas Laflorencie. Many-body localization: an introduction and selected topics. *arXiv preprint arXiv:1711.03145*, 2017.

[5] Irene Amado, Matthias Kaminski, and Karl Landsteiner. Hydrodynamics of holographic superconductors. *Journal of High Energy Physics*, 2009(05):021, 2009.

[6] P. R. Amestoy, I. S. Duff, J.-Y. L'Excellent, and J. Koster. A fully asynchronous multifrontal solver using distributed dynamic scheduling. *SIAM Journal on Matrix Analysis and Applications*, 23(1):15–41, 2001.

[7] P. R. Amestoy, A. Guermouche, J.-Y. L'Excellent, and S. Pralet. Hybrid scheduling for the parallel solution of linear systems. *Parallel Computing*, 32(2):136–156, 2006.

[8] Luigi Amico, Rosario Fazio, Andreas Osterloh, and Vlatko Vedral. Entanglement in many-body systems. *Reviews of Modern Physics*, 80(2):517, 2008.

[9] P. W. Anderson. Absence of diffusion in certain random lattices. *Phys. Rev.*, 109:1492, 1958.

[10] P. W. Anderson. Absence of diffusion in certain random lattices. *Phys. Rev.*, 109:1492–1505, 1958.

[11] Roland Assaraf, Michel Caffarel, and Anatole Khelif. Diffusion monte carlo methods with a fixed number of walkers. *Physical Review E*, 61(4):4566, 2000.

[12] Serge Aubry and Gilles André. Analyticity breaking and anderson localization in incommensurate lattices. *Ann. Israel Phys. Soc*, 3(133):18, 1980.

[13] Satish Balay et al. PETSc users manual. Technical Report ANL-95/11 - Revision 3.5, Argonne National Laboratory, 2014.

[14] Satish Balay, William D. Gropp, Lois Curfman McInnes, and Barry F. Smith. Efficient management of parallelism in object oriented numerical software libraries. In E. Arge, A. M. Bruaset, and H. P. Langtangen, editors, *Modern Software Tools in Scientific Computing*, pages 163–202. Birkhäuser Press, 1997.

[15] Ning Bao, ChunJun Cao, Sean M Carroll, Aidan Chatwin-Davies, Nicholas Hunter-Jones, Jason Pollack, and Grant N Remmen. Consistency conditions for an ads multiscale entanglement renormalization ansatz correspondence. *Physical Review D*, 91(12):125036, 2015.

[16] J. H. Bardarson, F. Pollmann, and J. E. Moore. Unbounded Growth of Entanglement in Models of Many-Body Localization. *Phys. Rev. Lett.*, 109:017202, 2012.

[17] D. M. Basko, I. L. Aleiner, and B. L. Altshuler. On the problem of many-body localization.

[18] D. M. Basko, I. L. Aleiner, and B. L. Altshuler. Metal insulator transition in a weakly interacting many-electron system with localized single-particle states. *Annals of Physics*, 321:1126–1205, May 2006.

[19] B. Bauer and C. Nayak. Area laws in a many-body localized state and its implications for topological order. *J. Stat. Mech: Theor. Exp.*, 9:09005, September 2013.

[20] John S. Bell. On the einstein-podolsky-rosen paradox. *Physics*, 1(3):195–200, 1964.

[21] Cédric Bény. Causal structure of the entanglement renormalization ansatz. *New Journal of Physics*, 15(2):023020, 2013.

[22] Michele Benzi. Preconditioning techniques for large linear systems: a survey. *Journal of Computational Physics*, 182(2):418–477, 2002.

[23] Danny Birmingham, Ivo Sachs, and Sergey N Solodukhin. Conformal field theory interpretation of black hole quasinormal modes. *Physical review letters*, 88(15):151301, 2002.

[24] Richard Blankenbecler, DJ Scalapino, and RL Sugar. Monte carlo calculations of coupled boson-fermion systems. i. *Physical Review D*, 24(8):2278, 1981.

[25] Richard Blankenbecler and RL Sugar. Projector monte carlo method. *Physical Review D*, 27(6):1304, 1983.

[26] P. Bordia, H. P. Lüschen, S. S. Hodgman, M. Schreiber, I. Bloch, and U. Schneider. Coupling Identical one-dimensional Many-Body Localized Systems. *Physical Review Letters*, 116(14):140401, April 2016.

[27] Pranjal Bordia, Henrik Lüschen, Ulrich Schneider, Michael Knap, and Immanuel Bloch. Periodically driving a many-body localized quantum system. *Nature Physics*, 13(5):460, 2017.

[28] Pranjal Bordia, Henrik P Lüschen, Sean S Hodgman, Michael Schreiber, Immanuel Bloch, and Ulrich Schneider. Coupling identical one-dimensional many-body localized systems. *Physical review letters*, 116(14):140401, 2016.

[29] Matteo Calandra Buonaura and Sandro Sorella. Numerical study of the two-dimensional heisenberg model using a green function monte carlo technique with a fixed number of walkers. *Physical Review B*, 57(18):11446, 1998.

[30] Pasquale Calabrese, Massimo Campostrini, Fabian Essler, and Bernard Nienhuis. Parity effects in the scaling of block entanglement in gapless spin chains. *Physical review letters*, 104(9):095701, 2010.

[31] Pasquale Calabrese and John Cardy. Entanglement entropy and quantum field theory. *Journal of Statistical Mechanics: Theory and Experiment*, 2004(06):P06002, 2004.

[32] Curtis Callan and Frank Wilczek. On geometric entropy. *Physics Letters B*, 333(1):55 – 61, 1994.

[33] C. Cao, S. M. Carroll, and S. Michalakis. Space from Hilbert space: Recovering geometry from bulk entanglement. *Phys. Rev. D*, 95(2):024031, January 2017.

[34] Sylvain Capponi and Andreas M Läuchli. Phase diagram of interacting spinless fermions on the honeycomb lattice: A comprehensive exact diagonalization study. *Physical Review B*, 92(8):085146, 2015.

[35] H Casini, CD Fosco, and M Huerta. Entanglement and alpha entropies for a massive dirac field in two dimensions. *Journal of Statistical Mechanics: Theory and Experiment*, 2005(07):P07007, 2005.

[36] J Casulleras and J Boronat. Unbiased estimators in quantum monte carlo methods: Application to liquid he 4. *Physical Review B*, 52(5):3654, 1995.

[37] DM Ceperley and B Bernu. The calculation of excited state properties with quantum monte carlo. *The Journal of chemical physics*, 89(10):6316–6328, 1988.

[38] Claudio Chamon, Alioscia Hamma, and Eduardo R Mucciolo. Emergent irreversibility and entanglement spectrum statistics. *Physical review letters*, 112(24):240501, 2014.

[39] Anushya Chandran, Isaac H Kim, Guifre Vidal, and Dmitry A Abanin. Constructing local integrals of motion in the many-body localized phase. *Physical Review B*, 91(8):085425, 2015.

[40] Shailesh Chandrasekharan. Fermion bag approach to lattice field theories. *Physical Review D*, 82(2):025007, 2010.

[41] Xie Chen, Zheng-Cheng Gu, and Xiao-Gang Wen. Local unitary transformation, long-range quantum entanglement, wave function renormalization, and topological order. *Physical review b*, 82(15):155138, 2010.

[42] Jae-yoon Choi, Sebastian Hild, Johannes Zeiher, Peter Schauß, Antonio Rubio-Abadal, Tarik Yefsah, Vedika Khemani, David A Huse, Immanuel Bloch, and Christian Gross. Exploring the many-body localization transition in two dimensions. *Science*, 352(6293):1547–1552, 2016.

[43] Valerie Coffman, Joydip Kundu, and William K. Wootters. Distributed entanglement. *Phys. Rev. A*, 61:052306, 2000.

[44] Shawn X Cui, Michael H Freedman, Or Sattath, Richard Stong, and Greg Minton. Quantum max-flow/min-cut. *Journal of Mathematical Physics*, 57(6):062206, 2016.

[45] Bartlomiej Czech, Lampros Lamprou, Samuel McCandlish, and James Sully. Tensor networks from kinematic space. *Journal of High Energy Physics*, 2016(7):100, 2016.

[46] W. De Roeck, F. Huveneers, M. Müller, and M. Schiulaz. Absence of many-body mobility edges. *Phys. Rev. B*, 93(1):014203, January 2016.

[47] Wojciech De Roeck and Francois Huveneers. Can translation invariant systems exhibit a many-body localized phase? *Preprint*, 2014.

[48] Wojciech De Roeck and François Huveneers. Stability and instability towards delocalization in many-body localization systems. *Physical Review B*, 95(15):155129, 2017.

[49] J. M. Deutsch. Quantum statistical mechanics in a closed system. *Phys. Rev. A*, 43:2046–2049, Feb 1991.

[50] Oscar JC Dias, Gary T Horowitz, and Jorge E Santos. Black holes with only one killing field. *Journal of High Energy Physics*, 2011(7):115, 2011.

[51] Jorge Dukelsky, Miguel A Martín-Delgado, Tomotoshi Nishino, and Germán Sierra. Equivalence of the variational matrix product method and the density matrix renormalization group applied to spin chains. *EPL (Europhysics Letters)*, 43(4):457, 1998.

[52] Philipp T Dumitrescu, Maksym Serbyn, Richard T Scalettar, and Ashvin Vishwanath. Superconductivity and nematic fluctuations in a model of doped fese monolayers: Determinant quantum monte carlo study. *Physical Review B*, 94(15):155127, 2016.

[53] J. Eisert, M. Cramer, and M. B. Plenio. *Colloquium* : Area laws for the entanglement entropy. *Rev. Mod. Phys.*, 82:277–306, 2010.

[54] G Evenbly, RNC Pfeifer, V Picó, S Iblisdir, L Tagliacozzo, IP McCulloch, and G Vidal. Boundary quantum critical phenomena with entanglement renormalization. *Physical Review B*, 82(16):161107, 2010.

[55] Glen Evenbly and Guifré Vidal. Algorithms for entanglement renormalization. *Physical Review B*, 79(14):144108, 2009.

[56] Glen Evenbly and Guifré Vidal. Tensor network states and geometry. *Journal of Statistical Physics*, 145(4):891–918, 2011.

[57] M. Fannes, B. Nachtergaele, and R. F. Werner. Finitely correlated states on quantum spin chains. *Communications in Mathematical Physics*, 144(3):443–490, 1992.

[58] Pau Figueras and Toby Wiseman. Stationary holographic plasma quenches and numerical methods for non-killing horizons. *Physical review letters*, 110(17):171602, 2013.

[59] M. H. Fischer, M. Maksymenko, and E. Altman. Dynamics of a Many-Body-Localized System Coupled to a Bath. *Physical Review Letters*, 116(16):160401, April 2016.

[60] Sebastian Fischetti, Donald Marolf, and Jorge E Santos. Ads flowing black funnels: Stationary ads black holes with non-killing horizons and heat transport in the dual cft. *Classical and Quantum Gravity*, 30(7):075001, 2013.

[61] Daniel S. Fisher. Random antiferromagnetic quantum spin chains. *Phys. Rev. B*, 50:3799–3821, Aug 1994.

[62] Barry Friedman. A density matrix renormalization group approach to interacting quantum systems on cayley trees. *Journal of Physics: Condensed Matter*, 9(42):9021, 1997.

[63] Max Führinger, Stephan Rachel, Ronny Thomale, Martin Greiter, and Peter Schmitteckert. Dmrg studies of critical su (n) spin chains. *Annalen der Physik*, 17(12):922–936, 2008.

[64] J. R. Garrison and T. Grover. Does a single eigenstate encode the full Hamiltonian? *Preprint*, 2015.

[65] A. Gendiar, N. Maeshima, and T. Nishino. Stable Optimization of a Tensor Product Variational State. *Progr. Theor. Phys.*, 110(4):691–699, 2003.

[66] Sarang Gopalakrishnan and Rahul Nandkishore. Mean-field theory of nearly many-body localized metals. *Phys. Rev. B*, 90:224203, Dec 2014.

[67] I. V. Gornyi, A. D. Mirlin, and D. G. Polyakov. Interacting electrons in disordered wires: Anderson localization and low-t transport. *Phys. Rev. Lett.*, 95:206603, Nov 2005.

[68] D Gross and J Eisert. Novel schemes for measurement-based quantum computation. *Physical review letters*, 98(22):220503, 2007.

[69] Tarun Grover. Certain general constraints on the many-body localization transition. *Preprint*, 2014.

[70] Tarun Grover and Matthew P A Fisher. Quantum disentangled liquids. *Journal of Statistical Mechanics: Theory and Experiment*, 2014(10):P10010, 2014.

[71] Emanuel Gull, Andrew J Millis, Alexander I Lichtenstein, Alexey N Rubtsov, Matthias Troyer, and Philipp Werner. Continuous-time monte carlo methods for quantum impurity models. *Reviews of Modern Physics*, 83(2):349, 2011.

[72] DC Handscomb. The monte carlo method in quantum statistical mechanics. In *Mathematical Proceedings of the Cambridge Philosophical Society*, volume 58, pages 594–598. Cambridge University Press, 1962.

[73] Sean A Hartnoll, Christopher P Herzog, and Gary T Horowitz. Building a holographic superconductor. *Physical Review Letters*, 101(3):031601, 2008.

[74] M B Hastings. An area law for one-dimensional quantum systems. *J. Stat. Mech.*, page P08024, 2007.

[75] Matthew B Hastings, Iván González, Ann B Kallin, and Roger G Melko. Measuring renyi entanglement entropy in quantum monte carlo simulations. *Physical review letters*, 104(15):157201, 2010.

[76] Stephen W Hawking. Gravitational radiation from colliding black holes. *Physical Review Letters*, 26(21):1344, 1971.

[77] Patrick Hayden, Sepehr Nezami, Xiao-liang Qi, Nathaniel Thomas, Michael Walter, and Zhao Yang. Holographic duality from random tensor networks. *Journal of High Energy Physics*, 2016(11):1, 2016.

[78] Vicente Hernandez, Jose E. Roman, and Vicente Vidal. SLEPc: A scalable and flexible toolkit for the solution of eigenvalue problems. *ACM Trans. Math. Software*, 31(3):351–362, 2005.

[79] James M Hickey, Sam Genway, and Juan P Garrahan. Signatures of many-body localisation in a system without disorder and the relation to a glass transition. *Journal of Statistical Mechanics: Theory and Experiment*, 2016(5):054047, 2016.

[80] Jorge E Hirsch, Robert L Sugar, Doug J Scalapino, and Richard Blankenbecler. Monte carlo simulations of one-dimensional fermion systems. *Physical Review B*, 26(9):5033, 1982.

[81] M Hohenadler, TC Lang, and FF Assaad. Correlation effects in quantum spin-hall insulators: A quantum monte carlo study. *Physical review letters*, 106(10):100403, 2011.

[82] M Hohenadler, ZY Meng, TC Lang, S Wessel, A Muramatsu, and FF Assaad. Quantum phase transitions in the kane-mele-hubbard model. *Physical Review B*, 85(11):115132, 2012.

[83] Christoph Holzhey, Finn Larsen, and Frank Wilczek. Geometric and renormalized entropy in conformal field theory. *Nuclear Physics B*, 424(3):443 – 467, 1994.

[84] Gary T Horowitz and Veronika E Hubeny. Quasinormal modes of ads black holes and the approach to thermal equilibrium. *Physical Review D*, 62(2):024027, 2000.

[85] Gary T Horowitz and Benson Way. Complete phase diagrams for a holographic superconductor/insulator system. *Journal of High Energy Physics*, 2010(11):11, 2010.

[86] Veronika E Hubeny. The ads/cft correspondence. *Classical and Quantum Gravity*, 32(12):124010, 2015.

[87] Veronika E. Hubeny, Mukund Rangamani, and Tadashi Takayanagi. A covariant holographic entanglement entropy proposal. *Journal of High Energy Physics*, 2007(07):062, 2007.

[88] David A Huse, Rahul Nandkishore, and Vadim Oganesyan. Phenomenology of fully many-body-localized systems. *Physical Review B*, 90(17):174202, 2014.

[89] David A. Huse and V. Oganesyan. A phenomenology of certain many-body-localized systems. *Phys. Rev. B*, 90:174202, 2014.

[90] John Z. Imbrie. On Many-Body Localization for Quantum Spin Chains. *Journal of Statistical Physics*, 163(5):998–1048, 2016.

[91] S. Iyer, V. Oganesyan, G. Refael, and D. A. Huse. Many-Body Localization in a Quasiperiodic System. *Phys. Rev. B*, 87:134202, 2013.

[92] Shankar Iyer, Vadim Oganesyan, Gil Refael, and David A. Huse. Many-body localization in a quasiperiodic system. *Phys. Rev. B*, 87:134202, 2013.

[93] Kristan Jensen. Chiral anomalies and ads/cmt in two dimensions. *Journal of High Energy Physics*, 2011(1):109, 2011.

[94] Hong-Chen Jiang, Matthew S Block, Ryan V Mishmash, James R Garrison, DN Sheng, Olexei I Motrunich, and Matthew PA Fisher. Non-fermi-liquid d-wave metal phase of strongly interacting electrons. *Nature*, 493(7430):39–44, 2013.

[95] B-Q Jin and Vladimir E Korepin. Quantum spin chain, toeplitz determinants and the fisher—hartwig conjecture. *Journal of statistical physics*, 116(1-4):79–95, 2004.

[96] Sonika Johri, Rahul Nandkishore, and R. N. Bhatt. Many-body localization in imperfectly isolated quantum systems. *Phys. Rev. Lett.*, 114:117401, Mar 2015.

[97] MH Kalos. Monte carlo calculations of the ground state of three-and four-body nuclei. *Physical Review*, 128(4):1791, 1962.

[98] MH Kalos. Stochastic wave function for atomic helium. *Journal of Computational Physics*, 1(2):257–276, 1966.

[99] MH Kalos, D Levesque, and L Verlet. Helium at zero temperature with hard-sphere and other forces. *Physical Review A*, 9(5):2178, 1974.

[100] MH Kalos and F Pederiva. Polarizability of the hydrogen molecule. *J. Chem. Phys.*, 46:1426, 1967.

[101] C Karrasch, JH Bardarson, and JE Moore. Reducing the numerical effort of finite-temperature density matrix renormalization group calculations. *New Journal of Physics*, 15(8):083031, 2013.

[102] S. Kehrein. Flow Equation Holography. *Preprint*, 2017.

[103] V. Khemani, S. P. Lim, D. N. Sheng, and D. A. Huse. Critical Properties of the Many-Body Localization Transition. *Preprint*, 2016.

[104] Vedika Khemani, Frank Pollmann, and SL Sondhi. Obtaining highly excited eigenstates of many-body localized hamiltonians by the density matrix renormalization group approach. *Physical review letters*, 116(24):247204, 2016.

[105] Vedika Khemani, DN Sheng, and David A Huse. Two universality classes for the many-body localization transition. *Physical review letters*, 119(7):075702, 2017.

[106] S Khlebnikov and M Kruczenski. Locality, entanglement, and thermalization of isolated quantum systems. *Physical Review E*, 90(5):050101, 2014.

[107] Jonas A. Kjäll, Jens H. Bardarson, and Frank Pollmann. Many-body localization in a disordered quantum ising chain. *Phys. Rev. Lett.*, 113:107204, Sep 2014.

[108] S. S. Kondov, W. R. McGehee, W. Xu, and B. DeMarco. Disorder-induced localization in a strongly correlated atomic hubbard gas. *Phys. Rev. Lett.*, 114:083002, Feb 2015.

[109] Robert König, Ben W Reichardt, and Guifré Vidal. Exact entanglement renormalization for string-net models. *Physical Review B*, 79(19):195123, 2009.

[110] Steven E Koonin, David J Dean, and Karlheinz Langanke. Shell model monte carlo methods. *Physics reports*, 278(1):1–77, 1997.

[111] PK Kovtun, Dan T Son, and Andrei O Starinets. Viscosity in strongly interacting quantum field theories from black hole physics. *Physical review letters*, 94(11):111601, 2005.

[112] Evgeny Kozik, Kris Van Houcke, Emanuel Gull, Lode Pollet, Nikolai Prokof'ev, Boris Svistunov, and Matthias Troyer. Diagrammatic monte carlo for correlated fermions. *EPL (Europhysics Letters)*, 90(1):10004, 2010.

[113] Jaron T Krogel and David M Ceperley. Population control bias with applications to parallel diffusion monte carlo. In *Advances in Quantum Monte Carlo*, pages 13–26. ACS Publications, 2012.

[114] AN Krylov. On the numerical solution of the equation by which in technical questions frequencies of small oscillations of material systems are determined. *Izvestija AN SSSR (News of Academy of Sciences of the USSR), Otdel. mat. i estest. nauk*, 7(4):491–539, 1931.

[115] Cornelius Lanczos. An iteration method for the solution of the eigenvalue problem of linear differential and integral operators. *J. Res. Natl. Bur. Std.*, 45:225, 1950.

[116] David P Landau and Kurt Binder. *A guide to Monte Carlo simulations in statistical physics*. Cambridge university press, 2014.

[117] Andreas M Läuchli. Numerical simulations of frustrated systems. In *Introduction to Frustrated Magnetism*, pages 481–511. Springer, 2011.

[118] JPF LeBlanc, Andrey E Antipov, Federico Becca, Ireneusz W Bulik, Garnet Kin-Lic Chan, Chia-Min Chung, Youjin Deng, Michel Ferrero, Thomas M Henderson, Carlos A Jiménez-Hoyos, et al. Solutions of the two-dimensional hubbard model: Benchmarks and results from a wide range of numerical algorithms. *Physical Review X*, 5(4):041041, 2015.

[119] Mac Lee, Thomas R Look, Say-Peng Lim, and DN Sheng. Many-body localization in spin chain systems with quasiperiodic fields. *Physical Review B*, 96(7):075146, 2017.

[120] Patrick A. Lee and T. V. Ramakrishnan. Disordered electronic systems. *Rev. Mod. Phys.*, 57:287–337, Apr 1985.

[121] Yevgeny Bar Lev, Guy Cohen, and David R Reichman. Absence of diffusion in an interacting system of spinless fermions on a one-dimensional disordered lattice. *Physical review letters*, 114(10):100601, 2015.

[122] E. Levi, M. Heyl, I. Lesanovsky, and J. P. Garrahan. Robustness of Many-Body Localization in the Presence of Dissipation. *Physical Review Letters*, 116(23):237203, June 2016.

[123] X. Li, S. Ganeshan, J. H. Pixley, and S. Das Sarma. Many body localization and quantum non-ergodicity in a model with a single-particle mobility edge. *Phys. Rev. Lett.*, 115:186601, 2015.

[124] Zi-Xiang Li, Yi-Fan Jiang, and Hong Yao. Solving the fermion sign problem in quantum monte carlo simulations by majorana representation. *Physical Review B*, 91(24):241117, 2015.

[125] EY Loh Jr, JE Gubernatis, RT Scalettar, SR White, DJ Scalapino, and RL Sugar. Sign problem in the numerical simulation of many-electron systems. *Physical Review B*, 41(13):9301, 1990.

[126] David J Luitz, François Huveneers, and Wojciech De Roeck. How a small quantum bath can thermalize long localized chains. *Physical review letters*, 119(15):150602, 2017.

[127] David J. Luitz, Nicolas Laflorencie, and Fabien Alet. Many-body localization edge in the random-field heisenberg chain. *Phys. Rev. B*, 91:081103, Feb 2015.

[128] Shang-Keng Ma, Chandan Dasgupta, and Chin-Kun Hu. Random antiferromagnetic chain. *Phys. Rev. Lett.*, 43:1434–1437, 1979.

[129] Juan Maldacena. The large-n limit of superconformal field theories and supergravity. *International Journal of Theoretical Physics*, 38(4):1113–1133, 1999.

[130] Igor L Markov and Yaoyun Shi. Simulating quantum computation by contracting tensor networks. *SIAM Journal on Computing*, 38(3):963–981, 2008.

[131] Miguel A Martin-Delgado and Germán Sierra. Analytic formulations of the density matrix renormalization group. *International Journal of Modern Physics A*, 11(17):3145–3174, 1996.

[132] Ian P McCulloch. From density-matrix renormalization group to matrix product states. *Journal of Statistical Mechanics: Theory and Experiment*, 2007(10):P10014, 2007.

[133] Roger G Melko. Stochastic series expansion quantum monte carlo. In *Strongly Correlated Systems*, pages 185–206. Springer, 2013.

[134] Roger G Melko and Anders W Sandvik. Stochastic series expansion algorithm for the s= 1/ 2 x y model with four-site ring exchange. *Physical Review E*, 72(2):026702, 2005.

[135] Sean P Meyn and Richard L Tweedie. *Markov chains and stochastic stability*. Springer Science & Business Media, 2012.

[136] Ryan V Mishmash, Matthew S Block, Ribhu K Kaul, DN Sheng, Olexei I Motrunich, and Matthew PA Fisher. Bose metals and insulators on multileg ladders with ring exchange. *Physical Review B*, 84(24):245127, 2011.

[137] M. Miyaji and T. Takayanagi. Surface/state correspondence as a generalized holography. *Progress of Theoretical and Experimental Physics*, 2015(7):073B03, July 2015.

[138] Ranjan Modak and Subroto Mukerjee. Many-body localization in the presence of a single-particle mobility edge. *Phys. Rev. Lett.*, 115:230401, Dec 2015.

[139] Kavan Modi, Aharon Brodutch, Hugo Cable, Tomasz Paterek, and Vlatko Vedral. The classical-quantum boundary for correlations: Discord and related measures. *Rev. Mod. Phys.*, 84:1655–1707, 2012.

[140] Kavan Modi, Tomasz Paterek, Wonmin Son, Vlatko Vedral, and Mark Williamson. Unified view of quantum and classical correlations. *Phys. Rev. Lett.*, 104:080501, Feb 2010.

[141] Ali Mollabashi, Masahiro Naozaki, Shinsei Ryu, and Tadashi Takayanagi. Holographic geometry of cmera for quantum quenches and finite temperature. *Journal of High Energy Physics*, 2014(3):98, 2014.

[142] Olexei I. Motrunich and Matthew P. A. Fisher. d-wave correlated critical bose liquids in two dimensions. *Physical Review B*, 75(23):235116, 2007.

[143] Robert C Myers, Andrei O Starinets, and Rowan M Thomson. Holographic spectral functions and diffusion constants for fundamental matter. *Journal of High Energy Physics*, 2007(11):091, 2007.

[144] R. Nandkishore. Many-body localization proximity effect. *Phys. Rev. B*, 92:245141, 2015.

[145] Rahul Nandkishore, Sarang Gopalakrishnan, and David A. Huse. Spectral features of a many-body-localized system weakly coupled to a bath. *Phys. Rev. B*, 90:064203, Aug 2014.

[146] Rahul Nandkishore and David A. Huse. Many-body localization and thermalization in quantum statistical mechanics. *Annual Review of Condensed Matter Physics*, 6(1):15–38, 2015.

[147] Michael A Nielsen and Isaac Chuang. *Quantum computation and quantum information*. AAPT, 2002.

[148] T. Nishino, Y. Hieida, K. Okunushi, N. Maeshima, Y. Akutsu, and A. Gendiar. Two-Dimensional Tensor Product Variational Formulation. *Progr. Theor. Phys.*, 105(3):409–417, 2001.

[149] V. Oganesyan and D. A. Huse. Localization of interacting fermions at high temperature. *Phys. Rev. B*, 75(15):155111, April 2007.

[150] Román Orús. A practical introduction to tensor networks: Matrix product states and projected entangled pair states. *Annals of Physics*, 349:117–158, 2014.

[151] Stellan Östlund and Stefan Rommer. Thermodynamic limit of density matrix renormalization. *Phys. Rev. Lett.*, 75:3537–3540, Nov 1995.

[152] Arijeet Pal and David A. Huse. Many-body localization phase transition. *Phys. Rev. B*, 82:174411, 2010.

[153] Shesansu Sekhar Pal. Model building in ads/cmt: Dc conductivity and hall angle. *Physical Review D*, 84(12):126009, 2011.

[154] Arun Paramekanti, Leon Balents, and Matthew P. A. Fisher. Ring exchange, the exciton bose liquid, and bosonization in two dimensions. *Physical Review B*, 66(5):054526, 2002.

[155] Fernando Pastawski, Beni Yoshida, Daniel Harlow, and John Preskill. Holographic quantum error-correcting codes: toy models for the bulk/boundary correspondence. *Journal of High Energy Physics*, 2015(6):1–55, 2015.

[156] Ingo Peschel. Calculation of reduced density matrices from correlation functions. *Journal of Physics A: Mathematical and General*, 36(14):L205, 2003.

[157] Ingo Peschel and Viktor Eisler. Reduced density matrices and entanglement entropy in free lattice models. *Journal of Physics A: Mathematical and Theoretical*, 42(50):504003, 2009.

[158] Robert NC Pfeifer, Glen Evenbly, and Guifré Vidal. Entanglement renormalization, scale invariance, and quantum criticality. *Physical Review A*, 79(4):040301, 2009.

[159] Ionut-Dragos Potirniche, Sumilan Banerjee, and Ehud Altman. On the stability of many-body localization in d ¿ 1. *Preprint*, 2018.

[160] William H Press. Long wave trains of gravitational waves from a vibrating black hole. *The Astrophysical Journal*, 170:L105, 1971.

[161] NV Prokof'ev, BV Svistunov, and IS Tupitsyn. "worm" algorithm in quantum monte carlo simulations. *Physics Letters A*, 238(4-5):253–257, 1998.

[162] Nikolai V Prokof'ev, Boris V Svistunov, and Igor S Tupitsyn. Exact quantum monte carlo process for the statistics of discrete systems. *Journal of Experimental and Theoretical Physics Letters*, 64(12):911–916, 1996.

[163] X.-L. Qi, Z. Yang, and Y.-Z. You. Holographic coherent states from random tensor networks. *Preprint*, 2017.

[164] Xiao-Liang Qi. Exact holographic mapping and emergent space-time geometry. *Preprint*, 2013.

[165] G. Refael and J. E. Moore. Entanglement entropy of random quantum critical points in one dimension. *Phys. Rev. Lett.*, 93:260602, Dec 2004.

[166] M. Rigol, V. Dunjko, and M. Olshanii. Thermalization and its mechanism for generic isolated quantum systems. *Nature*, 452:854–858, April 2008.

[167] Marcos Rigol and Lea F Santos. Quantum chaos and thermalization in gapped systems. *Physical Review A*, 82(1):011604, 2010.

[168] Stefan Rommer and Stellan Ostlund. A class of ansatz wave functions for 1d spin systems and their relation to dmrg. *Phys. Rev. B*, 55:2164, 1997.

[169] A. Rubio-Abadal, J.-y. Choi, J. Zeiher, S. Hollerith, J. Rui, I. Bloch, and C. Gross. Probing many-body localization in the presence of a quantum bath. *ArXiv e-prints*, April 2018.

[170] Shinsei Ryu and Tadashi Takayanagi. Aspects of holographic entanglement entropy. *Journal of High Energy Physics*, 2006(08):045, 2006.

[171] Shinsei Ryu and Tadashi Takayanagi. Holographic derivation of entanglement entropy from the anti˘de sitter space/conformal field theory correspondence. *Phys. Rev. Lett.*, 96:181602, 2006.

[172] Anders W Sandvik. Stochastic series expansion method with operator-loop update. *Physical Review B*, 59(22):R14157, 1999.

[173] Anders W Sandvik. Stochastic series expansion method for quantum ising models with arbitrary interactions. *Physical Review E*, 68(5):056701, 2003.

[174] Anders W Sandvik. Evidence for deconfined quantum criticality in a two-dimensional heisenberg model with four-spin interactions. *Physical review letters*, 98(22):227202, 2007.

[175] Anders W Sandvik and Hans Gerd Evertz. Loop updates for variational and projector quantum monte carlo simulations in the valence-bond basis. *Physical Review B*, 82(2):024407, 2010.

[176] Lea F Santos and Marcos Rigol. Localization and the effects of symmetries in the thermalization properties of one-dimensional quantum systems. *Physical Review E*, 82(3):031130, 2010.

[177] Lea F Santos and Marcos Rigol. Onset of quantum chaos in one-dimensional bosonic and fermionic systems and its relation to thermalization. *Physical Review E*, 81(3):036206, 2010.

[178] M. Schiulaz and M. Müller. Ideal quantum glass transitions: Many-body localization without quenched disorder. *AIP Conference Proceedings*, 1610(1):11–23, 2014.

[179] Ulrich Schollwöck. The density-matrix renormalization group. *Reviews of modern physics*, 77(1):259, 2005.

[180] Ulrich Schollwöck. The density-matrix renormalization group in the age of matrix product states. *Annals of Physics*, 326(1):96–192, 2011.

[181] M. Schreiber, S. S. Hodgman, P. Bordia, H. P. Lüschen, M. H. Fischer, R. Vosk, E. Altman, U. Schneider, and I. Bloch. Observation of many-body localization of interacting fermions in a quasirandom optical lattice. *Science*, 349:842–845, August 2015.

[182] Michael Schreiber, Sean S Hodgman, Pranjal Bordia, Henrik P Lüschen, Mark H Fischer, Ronen Vosk, Ehud Altman, Ulrich Schneider, and Immanuel Bloch. Observation of many-body localization of interacting fermions in a quasi-random optical lattice. *Science*, page aaa7432, 2015.

[183] M. Serbyn, Z. Papić, and D.A. Abanin. Local conservation laws and the structure of the many-body localized states. *Phys. Rev. Lett.*, 111:127201, 2013.

[184] M. Serbyn, Z. Papić, and D.A. Abanin. Universal slow growth of entanglement in interacting strongly disordered systems. *Phys. Rev. Lett.*, 110:260601, 2013.

[185] F Setiawan, Dong-Ling Deng, and JH Pixley. Transport properties across the many-body localization transition in quasiperiodic and random systems. *Physical Review B*, 96(10):104205, 2017.

[186] Y-Y Shi, L-M Duan, and Guifre Vidal. Classical simulation of quantum many-body systems with a tree tensor network. *Physical review a*, 74(2):022320, 2006.

[187] Gerard LG Sleijpen and Henk A Van der Vorst. A jacobi–davidson iteration method for linear eigenvalue problems. *SIAM review*, 42(2):267–293, 2000.

[188] J. Smith, A. Lee, P. Richerme, B. Neyenhuis, P. W. Hess, P. Hauke, M. Heyl, D. A. Huse, and C. Monroe. Many-body localization in a quantum simulator with programmable random disorder. *Nature Physics*, 12:907–911, October 2016.

[189] Dam T Son and Andrei O Starinets. Minkowski-space correlators in ads/cft correspondence: Recipe and applications. *Journal of High Energy Physics*, 2002(09):042, 2002.

[190] J. Sonner, A. Del Campo, and W. H. Zurek. Universal far-from-equilibrium dynamics of a holographic superconductor. *Nature Communications*, 6:7406, June 2015.

[191] M. Srednicki. Chaos and quantum thermalization. *Phys. Rev. E*, 50:888–901, August 1994.

[192] Mark Srednicki. Entropy and area. *Phys. Rev. Lett.*, 71:666–669, Aug 1993.

[193] Robin Steinigeweg, Jacek Herbrych, Frank Pollmann, and Wolfram Brenig. Typicality approach to the optical conductivity in thermal and many-body localized phases. *Physical Review B*, 94(18):180401, 2016.

[194] E Miles Stoudenmire. Learning relevant features of data with multi-scale tensor networks. *arXiv preprint arXiv:1801.00315*, 2017.

[195] E Miles Stoudenmire and Steven R White. Itensor-intelligent tensor library.

[196] G Sugiyama and SE Koonin. Auxiliary field monte-carlo for quantum many-body ground states. *Annals of Physics*, 168(1):1–26, 1986.

[197] Leonard Susskind. The world as a hologram. *Journal of Mathematical Physics*, 36(11):6377–6396, 1995.

[198] Brian Swingle. Entanglement renormalization and holography. *Phys. Rev. D*, 86:065007, 2012.

[199] Brian Swingle and John McGreevy. Renormalization group constructions of topological quantum liquids and beyond. *Physical Review B*, 93(4):045127, 2016.

[200] G. 't Hooft. Dimensional Reduction in Quantum Gravity, 1993.

[201] Luca Tagliacozzo and Guifre Vidal. Entanglement renormalization and gauge symmetry. *Physical Review B*, 83(11):115127, 2011.

[202] Tiamhock Tay and Olexei I. Motrunich. Possible realization of the exciton bose liquid phase in a hard-core boson model with ring-only exchange interactions. *Physical Review B*, 83(20):205107, 2011.

[203] Barbara M Terhal. Is entanglement monogamous? *IBM Journal of Research and Development*, 48(1):71–78, 2004.

[204] Luke Tierney. Markov chains for exploring posterior distributions. *the Annals of Statistics*, pages 1701–1728, 1994.

[205] Julien Toulouse, Roland Assaraf, and Cyrus J Umrigar. Introduction to the variational and diffusion monte carlo methods. In *Advances in Quantum Chemistry*, volume 73, pages 285–314. Elsevier, 2016.

[206] Nandini Trivedi and DM Ceperley. Green-function monte carlo study of quantum antiferromagnets. *Physical Review B*, 40(4):2737, 1989.

[207] Matthias Troyer and Uwe-Jens Wiese. Computational complexity and fundamental limitations to fermionic quantum monte carlo simulations. *Physical review letters*, 94(17):170201, 2005.

[208] Marko Žnidarič, Tomaž Prosen, and Peter Prelovšek. Many-body localization in the heisenberg xxz magnet in a random field. *Phys. Rev. B*, 77:064426, 2008.

[209] V. Vedral, M. B. Plenio, M. A. Rippin, and P. L. Knight. Quantifying entanglement. *Phys. Rev. Lett.*, 78:2275–2279, 1997.

[210] F. Verstraete and J. I. Cirac. Renormalization algorithms for Quantum-Many Body Systems in two and higher dimensions. *Preprint*, 2004.

[211] F. Verstraete, M. M. Wolf, D. Perez-Garcia, and J. I. Cirac. Criticality, the area law, and the computational power of projected entangled pair states. *Phys. Rev. Lett.*, 96:220601, Jun 2006.

[212] Frank Verstraete and J Ignacio Cirac. Matrix product states represent ground states faithfully. *Physical Review B*, 73(9):094423, 2006.

[213] G. Vidal. Entanglement renormalization. *Phys. Rev. Lett.*, 99:220405, 2007.

[214] G. Vidal. Class of quantum many-body states that can be efficiently simulated. *Phys. Rev. Lett.*, 101:110501, 2008.

[215] G. Vidal, J. I. Latorre, E. Rico, and A. Kitaev. Entanglement in quantum critical phenomena. *Phys. Rev. Lett.*, 90:227902, 2003.

[216] Guifre Vidal, José Ignacio Latorre, Enrique Rico, and Alexei Kitaev. Entanglement in quantum critical phenomena. *Physical review letters*, 90(22):227902, 2003.

[217] CV Vishveshwara. Stability of the schwarzschild metric. *Physical Review D*, 1(10):2870, 1970.

[218] Fugao Wang and DP Landau. Efficient, multiple-range random walk algorithm to calculate the density of states. *Physical review letters*, 86(10):2050, 2001.

[219] Xiaoguang Wang, Barry C. Sanders, and Dominic W. Berry. Entangling power and operator entanglement in qudit systems. *Phys. Rev. A*, 67:042323, 2003.

[220] Y. Wang, H. Hu, and S. Chen. Many-body ground state localization and coexistence of localized and extended states in an interacting quasiperiodic system. *European Physical Journal B*, 89:77, March 2016.

[221] Steven R. White. Density matrix formulation for quantum renormalization groups. *Phys. Rev. Lett.*, 69:2863–2866, Nov 1992.

[222] Alexander Wietek and Andreas M Läuchli. Sublattice coding algorithm and distributed memory parallelization for large-scale exact diagonalizations of quantum many-body systems. *Preprint*, 2018.

[223] Edward Witten. Anti De Sitter Space and Holography. *Adv. Theor. Math. Phys.*, 2:253–291, 1998.

[224] Michael M. Wolf. Violation of the entropic area law for fermions. *Phys. Rev. Lett.*, 96:010404, 2006.

[225] Michael M. Wolf, Frank Verstraete, Matthew B. Hastings, and J. Ignacio Cirac. Area laws in quantum systems: Mutual information and correlations. *Phys. Rev. Lett.*, 100:070502, Feb 2008.

[226] JC Xavier. Entanglement entropy, conformal invariance, and the critical behavior of the anisotropic spin-s heisenberg chains: Dmrg study. *Physical Review B*, 81(22):224404, 2010.

[227] Kai Xu, Jin-Jun Chen, Yu Zeng, Yu-Ran Zhang, Chao Song, Wuxin Liu, Qiujiang Guo, Pengfei Zhang, Da Xu, Hui Deng, et al. Emulating many-body localization with a superconducting quantum processor. *Physical review letters*, 120(5):050507, 2018.

[228] Zhao Yang, Patrick Hayden, and Xiao-Liang Qi. Bidirectional holographic codes and sub-ads locality. *Journal of High Energy Physics*, 2016(1):1–24, 2016.

[229] N. Y. Yao, C. R. Laumann, J. I. Cirac, M. D. Lukin, and J. E. Moore. Quasi-many-body localization in translation-invariant systems. *Phys. Rev. Lett.*, 117:240601, Dec 2016.

[230] Yi-Zhuang You, Zhao Yang, and Xiao-Liang Qi. Machine learning spatial geometry from entanglement features. *Physical Review B*, 97(4):045153, 2018.

[231] Xiongjie Yu, David J. Luitz, and Bryan K. Clark. Bimodal entanglement entropy distribution in the many-body localization transition. *Phys. Rev. B*, 94:184202, Nov 2016.

[232] Xiongjie Yu, David Pekker, and Bryan K Clark. Finding matrix product state representations of highly excited eigenstates of many-body localized hamiltonians. *Physical review letters*, 118(1):017201, 2017.

[233] Paolo Zanardi. Entanglement of quantum evolutions. *Phys. Rev. A*, 63:040304, 2001.